Effects of Fracture Geometry on Contaminant Transport

EFFECTS OF FRACTURE GEOMETRY ON CONTAMINANT TRANSPORT

BY

SEAN P. L. CIANFLONE,

B.Sc., (Mathematics and Statistics, McMaster University),

M.A.Sc.(Biomedical Engineering, McMaster University)

a thesis

Submitted to the Department of Civil Engineering

and the School of Graduate Studies

of McMaster University

in partial fulfilment of the requirements

for the degree of

Doctor of Philosophy

Doctor of Philosophy (2015)	McMaster University
Civil Engineering	Hamilton, Ontario, Canada

TITLE:	Effects of Fracture Geometry on Contaminant Transport
AUTHOR:	Sean P. L. Cianflone B.Sc., M.A.Sc.
SUPERVISOR:	Dr. Sarah E. Dickson
NUMBER OF PAGES:	xviii, 159

To Someone New

Abstract

Approximately one third of Canadians and Americans use groundwater as their source of drinking water. Porous media aquifers typically provide significant filtration of particulate contaminants (e.g., viruses, bacteria, protozoa) and solute contaminants. Fractured media, however, does not provide the same degree of filtration, and in fact often acts as a pathway for particulates to migrate, typically at much greater velocities than in porous media. This work studies the effects of the geometry of a fracture on the transport of two classes of contaminants: particles and dense non-aqueous phase liquids (DNAPLs).

An invasion percolation (IP) model simulates the invasion of one immiscible liquid by another. An IP model was used to illustrate the effects of gravity on DNAPL migration into a horizontal water saturated fracture. While gravity is typically neglected in the conventional approach, this work demonstrated that gravity should often be included when modelling DNAPL invasion in water saturated fractures and provides an equation estimating the difference in invasion pattern between simulations including or neglecting gravity as a criterion for discerning when gravity is important in this process. The IP model was further utilized to examine the invasion of DNAPL saturated fractures by water. These simulated experiments focus on cases where covariance (COV, the ratio of the mean of the aperture field to the standard deviation

of the aperture field) as well as when the fracture is oriented super-horizontally and sub-horizontally. Results show that when COV is greater than 0.1, then DNAPL will always remain in the fracture after waterflooding. Furthermore, fracture angles below -15° permit the complete removal of DNAPL, while fractures oriented at higher angles do not.

In order to study the transport of particles in water saturated fractures, physical experiments measuring the transport of 0.046 μm and 0.55 μm microspheres were undertaken on fractures where the geometry could be imported into a computer for comparative simulation analysis. Results demonstrated that during advection, particles generally travel at less than the velocity of the surrounding fluid. As well, hydrodynamic effects such as shear were shown to influence the effluent concentrations by increasing dispersion. Finally, the physical geometry of the fracture was shown to influence the particle pathway during transport and can limit the chances of particles adhering to a fracture wall, thus reducing dispersion and increasing peak concentration.

The combined results of these studies show that fracture geometry has a significant effect on the mechanisms of transport in saturated fractures. The geometry of a fracture can significantly change retention mechanisms for both DNAPLs and particles which would affect remediation strategies. In some cases, fracture statistics and contaminant properties alone are enough to make judgments regarding transport and retention (DNAPLs); however, this is not necessarily the case with particle transport where local geometric changes not accounted for in general fracture statistics can heavily affect transport and retention.

Acknowledgements

There are many people without whom I would not be where I am today. My advisor, Dr. Sarah Dickson, has provided support and invaluable advice during my research endeavours, as well, she has provided me invaluable tools I shall rely on in perpetuity. Sarah, I have learned so much from you! My committee members, Dr. Dieter Stolle and Dr. Paulin Coulibaly have provided valuable insight and suggestions throughout my time at McMaster University and I can't thank them enough for their support.

I have had many lab mates throughout the years and all of them have been supportive and helpful with advice on research, life or just a place to vent research related frustrations. In particular, Vick Lakhian, Ahmed Tawfic and Mohamed Mohamed - you gentlemen have made my grad work fun!! You gents aren't just my colleagues, but my friends.

My collaborators have been insightful and valuable in their own research efforts and this work would not be possible without them. In particular, Vick Lakhian, Jason Beattie and Dr. Kevin Mumford have provided their efforts in the constant challenge that is research, and have made this work all the better for it and me a better researcher.

I would also like to thank Mark Hahn who taught me so much about cluster computing. As well, I would like to thank Dr. C.Y. Ching and Dr. H. Mazhar for their help in producing digital versions of my experimental fractures.

I would also like to mention Frank Hayes, who never let me lose sight of the research (or hockey) goals. Our frequent lunch meetings served to keep me grounded! Go Habs Go!

I must also acknowledge the contributions of many hundreds of musical artists, without whom my late nights programming would have surely ended in computer parts being strewn about. In particular, to Mr. Gilmour, I'll keep rattling that lock!

Finally, my wife, Sarah Allison, has shown me nothing but love and support throughout my studies. She is the best thing that happened to me in grad school (there it is, in print, Love). My dogs, Finnigan and Gibson always provided a smile for me during any frustrating time and never let me stay up late working alone! You're my buds.

Notation and abbreviations

ADE Advection-Dispersion Equation
NAPL Non-aqueous phase liquid
DNAPL Dense non-aqueous phase liquid
IP Invasion percolation
BTC Breakthrough curve (contamination concentration in effluent)
RWPT Random Walk Particle Tracking
FEA Finite Element Analysis
PCE tetrachloroethylene
α used as a constant
β used as a constant
γ used as a constant
ε used as a constant
σ interfacial tension
θ wetting angle
φ macroscopic fracture angle
b fracture aperture
μ_b mean of the aperture field
μ_z mean of the mid-point aperture field
SD standard deviation
SD_b standard deviation of the aperture field
SD_z standard deviation of the mid-point aperture field
λ correlation
λ_b correlation of the aperture field
λ_z correlation of the mid-point aperture field
P_c capillary pressure

P_g pressure due to gravity

P_I invasion pressure

ρ density

g gravitational constant

N number of invasion elements (in IP model)

z elevation

R projection of DNAPL and fracture characteristics into 1 variable (as a ratio)

k_B Boltzmann constant

V velocity of the flow field

d_p particle diameter

T temperature

Re Reynold's number

$\mathbf{X_t}$ particle position at time t

D Stokes-Einstein diffusion constant

$\zeta\,(0,1)$ Gaussian distribution with mean of 0, standard deviation of 1

$\mathbf{U}_g$ velocity component of particle movement due to gravity

$\mathbf{S}\,(\mathbf{X_t})$ velocity component of particle movement due to shear

Preface

This thesis has been prepared according to the McMaster University regulations for theses consisting of previously published/prepared material. Chapters 2,3 and 4 consist of material prepared for publication as academic journal articles, and thus the material was co-authored by multiple authors. The contributions of each author to the chapters of this thesis are given below:

Chapter 2

Article Title:	On the Importance of Gravity in DNAPL Invasion of Saturated Horizontal Fractures
Authors:	Sean P. L. Cianflone, Sarah E. Dickson, Kevin G. Mumford

The DNAPL invasion experiment was performed by S. E. Dickson. The IP model was developed and programmed by S. P. L. Cianflone. The genetic algorithm optimization was performed by S. P. L. Cianflone. Simulations comparing gravity included and neglected scenarios were conducted by S. P. L. Cianflone. Analysis and interpretation of results was conducted by S. P. L. Cianflone in consultation with S. E. Dickson and K. G. Mumford. The manuscript was written by S. P. L. Cianflone and edited by S. E. Dickson and K. G. Mumford.

Chapter 3

Article Title:	Effects of gravity and aperture and midpoint aperture field statistics on DNAPL entrapment in fractures
Authors:	Sean P. L. Cianflone, Jason A. Beattie, Sarah E. Dickson

The IP model was developed and programmed by S. P. L. Cianflone. Overarching experimental (based on simulations) concepts were developed by S. P. L. Cianflone in consultation with J. A. Beattie and S. E. Dickson. All cluster computing code and simulations were developed and performed by S. P. L. Cianflone. Genetic algorithm optimization was performed by S. P. L. Cianflone. Statistical code was developed by S. P. L. Cianflone. Analysis and interpretation of results was conducted by S. P. L. Cianflone and J. A. Beattie in consultation with S. E. Dickson. The manuscript was written by S. P. L. Cianflone with minor contributions from J. A. Beattie and edited by S. E. Dickson.

Chapter 4

Article Title:	Effect of Hydrodynamics and Geometry on Particle Transport in Saturated Fractures: Experimental and Simulation Results
Authors:	Sean P. L. Cianflone, Vickram Lakhian, Sarah E. Dickson
Prepared for:	*Water Resources Research*

Overarching experimental methods and simulation direction was developed by S. P. L. Cianflone in consultation with V. Lakhian and S. E. Dickson. Experimental apparatus was developed by S. P. L. Cianflone and V. Lakhian. Experiments were performed by S. P. L. Cianflone. All simulations were coded and developed by S. P. L. Cianflone including all cluster computing efforts. Analysis and interpretation of results was conducted by S. P. L. Cianflone in consultation with S. E. Dickson and

V. Lakhian. The manuscript was written by S. P. L. Cianflone and edited by S. E. Dickson.

Contents

List of Figures

List of Tables

Chapter 1

Introduction

1.1 Background

At least 25% of Canadians utilized groundwater for drinking water in 2010 (Dewar and Soulard, 2010). In the United States, approximately 37% of the public water supply was sourced from groundwater in 2010 (Maupin *et al.*, 2010). Furthermore, 14% of Americans utilized self-supplied domestic water sourced from groundwater (Maupin *et al.*, 2010). In terms of geographic distribution, the percentage of people reliant on groundwater as a potable water source increases in more rural areas; for example, in Northern Ontario and Northern Manitoba, 50-75% of the population is dependent on groundwater and in Northern Quebec, more than 75% of the population utilizes groundwater as a primary drinking water source (Dewar and Soulard, 2010). Given the usage of ground water, it is essential to understand the mechanisms which may jeopardize this resource.

The studies undertaken in this thesis have focused on two different types of possible contaminants of groundwater: Dense Non-aqueous Phase Liquids (DNAPLs) and colloids. DNAPLs are generally immiscible fluids that are denser than water. The immiscibility of DNAPLs leads to two-phase flow physics when analyzing transport mechanisms (Glass and Nicholl, 1996). Colloids are particles that measure approximately 1 nm to 1 μm in size which are suspended in groundwater; however, these are not strict limitations (Gregory, 2006). The physical nature of colloid transport and, more generally, particle transport, is rooted in hydrodynamic forces on the particles themselves as well as attachment or detachment from the media in which the transport is occurring (Gregory, 2006).

Contamination of the subsurface by DNAPLs generally occurs as a result of chemical spills from an industrial setting. Typical DNAPLs found in the subsurface include tetrachloroethylene (PCE), the associated degradation product trichloroethylene (TCE) and petroleum products (e.g. creosote). TCE and PCE are commonly used in dry cleaning facilities and in manufacturing (Parker *et al.*, 2003). As DNAPLs are denser than water they tend to migrate downward in the subsurface and the general immiscibility of this class of chemicals can lead to pools forming in porous and fractured media. These pools can invade fractures and the surrounding porous media and rock matrix displacing the local groundwater. The immiscibility of DNAPLs allows flowing groundwater to move DNAPL in the subsurface and form plumes of contamination (Parker *et al.*, 2003). While DNAPLs are considered immiscible in water, small concentrations do dissolve in groundwater and may be transported at contamination levels above safe drinking water limits, thus the plume results in a persistent source of contamination. As of 1994, the estimated number of sites in the USA suspected of containing petroleum hydrocarbons was from 30 000 to 50 000, excluding leaking storage tanks (Kavanaugh and Rao, 2003). Estimates suggest that

27 000 of 36 000 dry cleaners in the USA have experienced some level of dry cleaning solvent or PCE release (Kavanaugh and Rao, 2003). Kavanaugh and Rao (2003) estimate that there are 15 000 to 25 000 sites in the USA currently impacted by DNAPL. These numbers show the ubiquitous nature of DNAPL contamination and suggest the need to understand the processes at work during the release and remediation of DNAPL contaminated sites. Remediation of DNAPL sites may be performed using pump-and-treat methods which are quite costly. Annual costs for operation of pump-and-treat technologies at a DNAPL contaminated site ranges from $30 000 to $4 000 000, with the median cost of approximately $180 000 in 1998 (Kavanaugh and Rao, 2003). The overall cost of pump-and-treat for the 15 000 to 25 000 sites is between $2.7 billion and $4.2 billion per annum (Kavanaugh and Rao, 2003). This technique must continue for 30-50 years as flushing does not mobilize a large amount of DNAPL (Darwish *et al.*, 2003; Mackay and Cherry, 1989; Alexandra *et al.*, 2012), leading to a long-term and very expensive issue. Another related method of remediation includes the addition of oxidizers such as permanganate or peroxide which breaks down the DNAPL in place (*in situ* chemical oxidation) (Kueper *et al.*, 2014). Similarly, the introduction of reductive species to the contaminated subsurface may also be used (*in situ* chemical reduction) (Kueper *et al.*, 2014). Even stimulating the growth of naturally occurring microorganisms is a possibility for DNAPL remediation (bioremediation)(Kueper *et al.*, 2014). Naturally, the use and cost of a given remediation strategy depends on the contaminant, geology and physical nature of the site. The associated costs of remediation efforts tends to be lowest with bioremediation at about half of the cost associated with pump-and-treat methods, but other remediation strategies tend towards a cost basis similar to that of pump-and-treat options

(Kueper *et al.*, 2014). Ultimately, understanding the mechanisms involved in DNAPL contamination in the subsurface as well as the mechanisms involved in remediation strategies is essential to the long-term management of groundwater supplies.

The events surrounding the bacterial contamination of drinking water in Walkerton, Ontario leading to more than 2300 cases of illness (some with long term health consequences) and 7 deaths gave rise to an inquiry and subsequent report detailing concerns over drinking water (O'Connor, 2002a). Most notably, the report proclaimed that people should feel safe drinking tap water and that source water requires protection and regular testing in order to maintain it safely (O'Connor, 2002b). Although awareness has increased surrounding the health and safety of our drinking water supply, the protection of source water from bacterial and other forms of contamination still remains a very real concern in Canada (O'Connor, 2002b). The primary source of the contamination was runoff from a farm which had spread manure containing *E. coli O157:H7* and *Campylobacter* strains. The runoff from the farm impacted the local groundwater used as a source of municipal drinking water (O'Connor, 2002a). While the contamination and resulting infection of the residents of Walkerton was rooted in several levels of mishandling and mismanagement at the treatment level (Schuster *et al.*, 2005), the studies contained in this thesis focus on protection and management of the groundwater sources.

The bacterial contamination that occurred in 2000 in Walkerton, Ontario is one of the more commonly cited examples of waterborne illness in Canada, but from 1974 to 2001 there were 288 cases of waterborne outbreaks in Canada alone (Schuster *et al.*, 2005). The causes of waterborne illness include viruses (e.g. norovirus, hepatitis A), bacteria (e.g. *E. coli*, *Salmonella*, *Campylobacter*), and protozoa (e.g. *Giardia*, *Cryptosporidium*) (Schuster *et al.*, 2005). Viruses are of the smallest of these contaminants at around a few nanometers in size; bacteria are typically around a micron in size, while protozoa are around 10 microns in size, although these measurements are by no means limiting. Viruses and bacteria are considered colloids for the purposes of this work. In porous media aquifers typically provide significant removal of particulate contaminants (eg. viruses, bacteria); however, in fractured rock aquifers and aquitards, fractures often provide pathways for particles to move in greater numbers and speed than in porous media (Shapiro and Bedrikovetsky, 2010; Vesper *et al.*, 2003). Thus, understanding flow and transport in fractures is important for the preservation and use of groundwater sources.

1.2 Transport of DNAPLs in the Subsurface

The transport of the contaminants studied in this thesis differs depending on the type of contaminant. DNAPLs are frequently found in industrially contaminated sites throughout the world and pose a challenge for remediation efforts. The invasion, migration, and transport of DNAPL in the subsurface is based on the physics of two-phase flow. As DNAPLs are generally immiscible in water, the invasion of DNAPL into porous media or fractures requires the displacement of water. Furthermore, during hydraulic displacement type remediation methods, water (sometimes with co-solvents or surfactants to aid in liberating the DNAPL pool) also causes the displacement of DNAPL (Kavanaugh and Rao, 2003; Kueper and McWhorter, 1991; Mackay and Cherry, 1989). The forces at work in DNAPL migration in the subsurface are rooted in capillary action, surface tension, viscosity and gravity effects. As the density of DNAPLs is greater than that of water, DNAPLs are under gravitational influence drawing the contaminant deeper below the subsurface.

Assuming there is no mass transfer between phases, the medium is not deformable and the fluids are incompressible, the mass balance equations governing the two-phase flow problem of DNAPL and groundwater in the subsurface are (Bear, 1972; Gerhard *et al.*, 1998):

$$-\frac{\partial}{\partial x_i}\left(\rho_W q_{W,i}\right) + Q_W = \frac{\partial}{\partial t}\left(\phi \rho_W S_W\right) \tag{1.1}$$

$$-\frac{\partial}{\partial x_i}\left(\rho_N q_{N,i}\right) + Q_N = \frac{\partial}{\partial t}\left(\phi \rho_N S_N\right) \tag{1.2}$$

where N and W represent the non-wetting and wetting phases respectively, ρ represents density, q is phase flux, Q is the sink/source term, ϕ is porosity of the medium, and S is saturation fraction. These equations must be coupled with flow equations in order to garner a solution for which Darcys law is typically used (Bear, 1972; Gerhard *et al.*, 1998; Kueper and Frind, 1988). Furthermore, $S_N + S_W = 1$ as the two fluids saturate the entire medium. The substitution of Darcys law requires the computation of the phase pressures, P_N and P_W and as such the capillary pressure relation $P_C = P_N - P_W$ must be satisfied (Bear, 1972; Gerhard *et al.*, 1998; Kueper and Frind, 1988). Numerically solving these equations is computationally heavy, although Gerhard *et al.* (1998) developed solutions using a finite difference scheme. Similarly, Esposito and Thomson (1999) solved this system utilizing a finite volume method. The great computational expense in solving these equations numerically does not lend this system to optimization with respect to an experiment.

A computationally lighter simulation was developed by Broadbent and Hammersley (1957), namely the concept of invasion-percolation (IP). The premise of IP is rooted in the path of least resistance. For example, assume a non-wetting fluid (DNAPL) is invading a saturated wetting fluid (water) system (either porous media or a fracture). The initial step of the algorithm is the discretization of the domain into elements. Along the invading fluid front, the local capillary pressures opposing invasion are computed. The non-wetting fluid will then proceed to displace the wetting fluid in the least resistant element. A new front will be formed based on the new geometry of the two phases, and the method is repeated. This technique has been used for modelling the invasion of DNAPL in porous media (Ewing and Gupta, 1993; Glass and Nicholl, 1996; Meakin *et al.*, 2000; Mumford *et al.*, 2010; Wagner *et al.*, 1997; Wilkinson and Willemsen, 1983). The IP algorithm was modified for fractures by accounting for the local aperture field and the capillary pressures associated with a parallel plate fracture in that local domain (Glass *et al.*, 2004; Petchsingto and Karpyn, 2010; Weerakone *et al.*, 2012; Yang *et al.*, 2012b). In general, this technique assumes that capillary forces dominate the invasion process while neglecting viscous forces, the stabilizing effect of surface tension, and gravitational effects (Kueper and Frind, 1988). Several additions have been made to the IP algorithm in an attempt to account for more forces. While capillary pressure is often computed based on the local aperture field of the fracture being considered a parallel plate, a method of computing capillary pressure utilizing the local in-plane curvature of the invading fluid was incorporated into IP models (Glass *et al.*, 1998; Yang *et al.*, 2012b). Glass and Yarrington (2003) and Meakin *et al.* (2000) both included gravity in porous media models; however, the gravity component was applied as a constant throughout the media. Gravity has also been incorporated into IP models regarding fractures; however, only in the vertical case where the computation only requires a constant gravitational effect while ignoring the local undulating nature of the fracture geometry (Yang *et al.*, 2013a). Furthermore, methods for including viscous forces have been included in IP models (Xu *et al.*, 1998; Glass *et al.*, 2001; Ewing and Berkowitz, 1998). For example, Ewing and Berkowitz (1998) included a random component in selecting the invasion elements for step to account for viscous effects. Glass and Yarrington (2003) utilized an invasion and re-invasion approach which allowed invasion to occur, then allowed the defending fluid to re-invade an element occupied by the invader, but only if a predetermined threshold was reached. The invasion and re-invasion method allowed for effects such as pulsation and pinching off to occur (Glass and Yarrington, 2003).

1.3 Transport of Particles in the Subsurface

The transport of particles in groundwater (or the subset of particles known as colloids) hinges on several physical effects: advection, dispersion, diffusion, straining, matrix flow, and attachment and detachment of particles to media. The main focus of this thesis is to understand particulate transport in saturated rock fractures since ground characteristics of the aquifer and the surrounding region can threaten source water quality. In fact, flow rates in fractures can be orders of magnitude greater than the surrounding media which can contaminate sources far more quickly than would normally be predicted in porous media (Berkowitz, 2002). Understanding flow and transport in fractures is therefore important for the preservation, use and potential remediation of contaminated sources (Berkowitz and Scher, 1997). The Navier-Stokes equations define the flow regime in a fracture and the solution is quite dependent on the geometry of the fracture (Brush and Thomson, 2003; Cardenas *et al.*, 2007; Koyama *et al.*, 2008b,a). While assumptions can be made that simplify the Navier-Stokes equations for ease of numerical solution, the resultant velocity flow field is based on the head difference across a varying geometrical system defining the fracture walls (Brush and Thomson, 2003; Koyama *et al.*, 2008b,a). An important measure of the turbulence in a flow field is the Reynolds Number, Re, which is the ratio of inertial over viscous forces in the flow field. When viscous forces dominate (e.g. $Re < 1$), then flow is generally laminar. Dominant inertial forces ($Re > 1$) tend to impose greater turbulence in the field. For fractures, a laminar flow field is generally assumed as the flow is slow enough for viscous forces to dominate; however, turbulence including eddies have been shown at groundwater velocities typically associated with laminar flow in fractures (Cardenas *et al.*, 2007). Once a fluid flow field is determined (typically numerically), the field may be coupled with transport equations in order to simulate the transport of solutes or particulate matter (e.g. viruses, bacteria and protozoa) in the fracture (Berkowitz, 2002; Zheng *et al.*, 2009b). Theory surrounding the movement as well as the adhesion to or detachment of microorganisms from media is based on treating the microorganism as a charged sphere. Both experimental results and simulations have shown that there are inconsistencies in current theory (Bayoudh *et al.*, 2009; Torkzaban *et al.*, 2007), particularly when particle size is varied (Zheng *et al.*, 2009b).

Transport of particles is of great interest because contaminants may compromise the water supply and this contamination of the water supply can happen far more quickly in fractures than in typical porous media (Berkowitz, 2002; Song and Elimelech, 1993, 1994). Furthermore, the notion of deposition of contaminants is very important as hazardous microbes, for example, may proliferate or require greater time to exit the fracture if deposition (and perhaps subsequent release from the wall) occurs (Kretzschmar *et al.*, 1997). Thus, a model of particulate transport and deposition is very important towards understanding how particulate contaminants migrate through a fractured aquifer.

The Advection-Dispersion Model

Diffusion is the process by which ionic and molecular species dissolved in water move through a fluid from high potentials to low potentials (Fetter, 2001). Advection is the process by which solutes or particles are carried with the fluid. Dispersion is the process by which particles or solutes are spread due to velocity variations within the fluid and different path lengths (Fetter, 2001). There are three main mechanisms of dispersion in porous media:

1. When pore size is locally smaller, the water slows versus when pore size is larger, the water moves more quickly thus spreading out the contaminant due to varying velocities (Figure 1.1 Pore Size) (Fetter, 2001).

2. As water moves in porous media, various paths may be taken and longer paths will generally take longer to navigate whereas shorter paths will require less transport time, again spreading out the contaminant and diluting it (Figure 1.1 - Path Length) (Fetter, 2001).

3. Finally, boundaries of media have a no-slip boundary condition meaning that

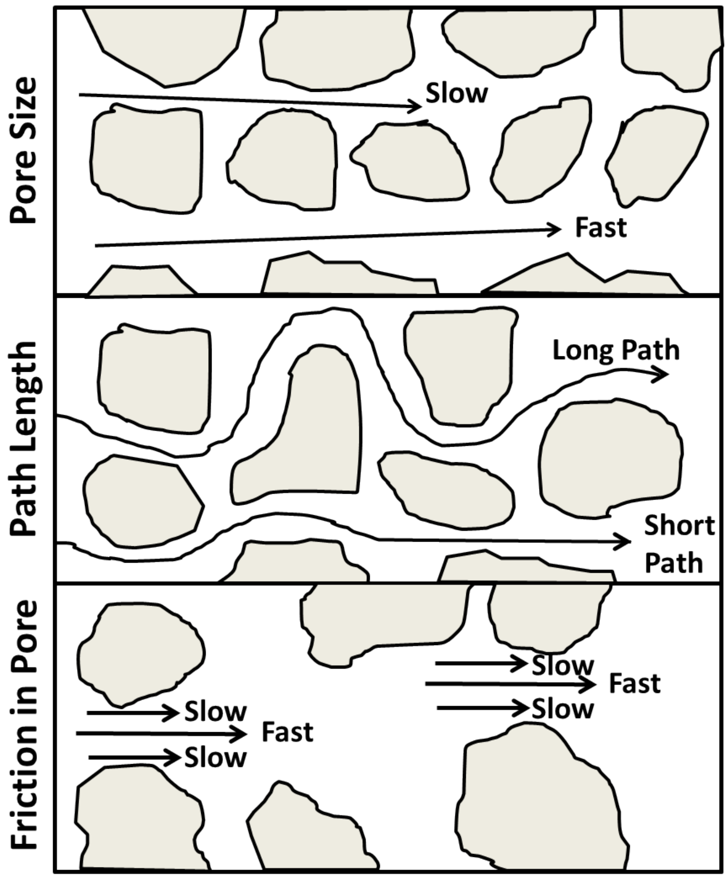

Figure 1.1: A diagram depicting the three mechanisms by which dispersion occurs in porous media. Figure modified from Fetter (2001).

near these boundaries water flows more slowly essentially due to friction against the boundary. Thus, contaminants near the boundaries will encounter slower speeds than speeds found midway between two boundaries. Thus, dilution of the contaminant occurs due to varying velocities (Figure 1.1 - Friction in Pore) (Fetter, 2001).

These three mechanisms occur in rock fractures, but the velocity variations and path lengths are a product of the 3D geometry found in the fracture. In particular, the majority of the contaminant mass will follow certain preferential paths where the aperture is larger and water is flowing more quickly. Due to the various paths that water may take in a fracture, the length of path will also cause dispersion. Finally, perhaps the most obvious analogue in the fracture setting is that of friction with the boundary of the fracture. In this case, the contaminant will flow more quickly in the midline of the fracture than near the boundary. The region near the fracture boundary where flow is slower is known as the boundary layer (Qian *et al.*, 2011a,b).

The Advection-Dispersion Equation (ADE) was developed to combine the effects of advection and dispersion to describe contaminant transport (Bear, 1972; Fetter, 2001; Qian *et al.*, 2011a,b). The ADE in one dimension for porous media is given as follows:

$$\frac{\partial C}{\partial t} = D_L \frac{\partial^2 C}{\partial x^2} - v \frac{\partial C}{\partial x} \tag{1.3}$$

where $C = C(x;t)$ is the concentration of a solute and the solution to the differential equation, D_L is the coefficient of longitudinal hydrodynamic dispersion, v is the average fluid velocity in the single direction (x in this case), and t is time (Bear, 1972; Fetter, 2001). It is valuable to note that the dispersion coefficient is an *effective* dispersion coefficient accounting for mechanical dispersion as well as diffusion. The ADE equates the change in concentration over time (Equation 1.3 - left side) to the rate of dispersion

$$D_L \frac{\partial^2 C}{\partial x^2} \tag{1.4}$$

minus the effects of advection

$$v \frac{\partial C}{\partial x} \tag{1.5}$$

A modification to the ADE is the addition of a retardation term, R. This retardation term is a constant that accounts for any straining, adhesion or detachment of the solute or particles being modelled. The application of R is as follows:

$$R\frac{\partial C}{\partial t} = D_L\frac{\partial^2 C}{\partial x^2} - v\frac{\partial C}{\partial x} \tag{1.6}$$

ADE and ADE-R have been used to model solute transport in fractured rock on several occasions where they were coupled with Darcys equation of flow (Qian *et al.*, 2011a,b). When comparing ADE to data collected from experiments in fractured rock using Darcys law to model flow, ADE-R outperformed ADE due to the use of R as a fitting parameter (Qian *et al.*, 2011a,b). Unfortunately, in these cases, bulk flow laws were used to compute flow under conditions where the flow was not laminar (Re was reportedly between 10 and 90) (Qian *et al.*, 2011a,b). Due to the use of flow models that fail to account for turbulence encountered in fractures with large Re (Brush and Thomson, 2003), the results may only suggest that the use of a fitting parameter in the differential equation allows for good fitting of results. The method used could be improved if turbulence is accounted for, as eddies are a way in which particles may be retarded (Cardenas *et al.*, 2007). Koyama *et al.* (2008b) compared models coupling ADE with NS versus ADE coupled with a flow field generated using a simplification of the Navier-Stokes equations (the local cubic law) in fractured media. The Reynolds numbers ranged from 50-70 (Koyama *et al.*, 2008b) which suggests that the local cubic law does not provide a reasonable approximation of the flow field (Brush and Thomson, 2003). As well, dispersion is neglected in this model (Koyama *et al.*, 2008b). Transport was reasonably modelled; however, because dispersion is ignored, jumping between stream lines of particles was not possible resulting in trapping that was permanent, which is not an accurate physical representation of the system (Koyama *et al.*, 2008b,a). In Koyamas work, the NS model outperformed the local cubic law model showing a significant impact on particulate transport (Koyama *et al.*, 2008b).

Random Walk Particle Tracking

An alternative to the ADE type methods is the Random Walk Particle Tracking method (RWPT). RWPT is not as computationally expensive as numerically solving the ADE (which also requires numerically solving for a fluid flow field) (Berkowitz, 2002). In short, the amount of computation time is increased so a method of describing the movement of particles more simply was developed (Salamon *et al.*, 2006b,a). Furthermore, it may be shown that the RWPT method mathematically resolves to the ADE (Equation 1.3) (Salamon *et al.*, 2006b,a).

The premise behind RWPT is to model the particulate mass with a large population of representative particles affected by the flow in the fracture. As time progresses, the particle is driven by a drift term representing the advective properties of the flow field. Diffusion/dispersion is considered using Brownian motion in a combined random term. The mathematical formulation is as follows:

$$X_{t+1} = X_t + \mathbf{A}\left(X_t\right)\Delta t + \mathbf{B}\left(X_t\right)\xi\left(0,1\right)\sqrt{\Delta t} \tag{1.7}$$

where X_t is the position of the particle at time, t, $\mathbf{A}$ is the drift vector created by interpreting the flow field at the position of the particle (advection term), and $\mathbf{B}$ is the displacement matrix defining the dispersion effects. In order to introduce random motion into the dispersion/diffusion, $\mathbf{B}$, is multiplied by $\xi\left(0,1\right)$, a vector of independent and normally distributed random numbers with mean of zero and unit variance (Salamon *et al.*, 2006b). The diffusion values given in **B** may be computed using a Brownian motion constant defined by the Stokes-Einstein equation (pure diffusion) (James and Chrysikopoulos, 2000; Zheng *et al.*, 2009b,a) or by adding an effective dispersion values (typically greater than the Stokes-Einstein diffusion values) to the diffusion values (James and Chrysikopoulos, 2003; Zheng *et al.*, 2009a).

This formulation allows for quick computation of particle motion and the tracking allows for the computation of local concentrations of particles (Berkowitz, 2002; James and Chrysikopoulos, 2000, 2011; James *et al.*, 2005; Salamon *et al.*, 2006b). James and Chrysikopoulos (2011) considered an RWPT based algorithm with polydisperse particles (particles of different sizes) and gravity in a vertically oriented parallel plate (ie. fixed aperture) fracture. James and Chrysikopoulos (2011) showed that gravitational effects are, in general, not negligible and they become more pronounced as particle size increases. RWPT methods have provided reasonably accurate models of transport and plume movement for transport in fractures (James and Chrysikopoulos, 2000, 2011). Zheng *et al.* (2009b) found that by modelling fracture flow using the local cubic law (with $Re < 1$) particles did not obey the general theory that smaller particles travelling through a fracture should move more slowly than larger ones. The underlying reason for this theory is that smaller particles can sample the slower velocities found near the boundary layer whereas larger ones can only sample the faster velocities in the midpoint of the fracture (Zheng *et al.*, 2009b). Zheng *et al.* (2009b), the RWPT method was used to show that the velocities of particles decrease with size, but only to a point and then begin to increase again because the effects of dispersion are overestimated by standard theory. This effective dispersion value is an averaged value based on integrating over a parallel plate fracture and as well, the implementation of the coefficient eliminates any directional component associated with dispersion caused by hydrodynamics in the local flow field.

Recently, several studies have been performed in microchannels elucidating upon the effect of fluid shear on particles. It has been shown that particles migrate away from the center of a channel thus increasing dispersion by lengthening the time taken for all particles to exit a channel (or fracture) (Di Carlo *et al.*, 2007, 2009; Masaeli *et al.*, 2012; Rusconi *et al.*, 2014). These studies elaborate on the physics of the dispersive effects of transport given a local flow field. In particular, Taylor (1953) and Aris (1956) initially reported that particles migrate away from the center of a channel and away from a wall as well. Taylor and Aris attempted to quantify this effect utilizing an averaged effective dispersion coefficient; however, the most current studies show how to compute the directionality of particles moving away from the center line, namely with the negative of the spatial derivative of the flow field (Rusconi *et al.*, 2014). Furthermore, Di Carlo *et al.* (2009) effectively computed the wall effect based on pressure effects forming between the wall and particle suggesting that this effect is related to scale as well, and thus more noticeable in a tiny microchannel.

The main advantage of RWPT type methods is the low computation time required for generating particle motion (Berkowitz, 2002; Salamon *et al.*, 2006b). Furthermore, due to the particle tracking method, individual particles may be monitored under various conditions such as whether or not walls are being struck or if straining occurs (Berkowitz and Scher, 1997). Furthermore, particle tracking methods allow for modification of modelling approaches involving local characteristics such as local hydrodynamic effects (ie. shear or dispersion) as well as allowing for ease of optimization of parameters related to the transport mechanisms. The monitoring of particles is not directly possible using ADE-based methods and therefore will not account for mechanical straining or wall collisions resulting in adhesion to the fracture wall.

1.4 Motivation for Contamination Transport Research

While the effects of gravity are known to be involved in DNAPL invasion in the subsurface, this effect is neglected in all models of two-phase flow in saturated horizontal fractures with the argument that capillary forces heavily dominate any gravitational effects (Petchsingto and Karpyn, 2010; Weerakone *et al.*, 2012; Yang *et al.*, 2012b). Thus, in this thesis, efforts to compute the effects of gravity based on the local geometry of the undulating field of a horizontal fracture were taken in order to understand how gravity affects the invasion of DNAPL into water saturated horizontal fractures. The results of the gravity study (Chapter 2) showed that while capillary forces may be up to two orders of magnitude greater than those caused by gravity, they are nevertheless important in the overall pattern of DNAPL invasion observed. This observation was based on optimizing an IP model with experimental results that included a local gravity computation accounting for the local undulating nature of the fracture geometry. Further to this point, as gravity was shown to be important in horizontal fractures, it is reasonable to assume that the effect of gravity may be further amplified in angled fractures. To date, no study regarding the effects of two-phase flow on macroscopically angled fractures has been undertaken (only horizontal and vertical fracture orientations), despite the expectation that fractures in the environment may be at any angle. Several remediation methods include some level of flushing the subsurface with water (sometimes with the inclusion of co-solvents or oxidizers). Thus, a study to examine the effects of flushing fractures containing DNAPL was undertaken focusing on retained DNAPL while varying fracture angles (Chapter 3). This model included gravitational effects based not only on the local geometry of the fracture, but the macroscopic angle of the fracture as well. This study ultimately led to the observation that complete removal of DNAPL is permitted in fractures aided by gravity at an angle of approximately $-10\,^{\circ}$ to $-15\,^{\circ}$; however, at higher angles complete removal is forbidden during the flushing process. Furthermore, it was possible to develop estimates of entrapped DNAPL depending on the angle of the fracture as well as the statistical (geometrical) characteristics of the fracture and the characteristics of the DNAPL.

Several studies model particle transport in fractures (e.g. James and Chrysikopoulos, 2003, 2011; James *et al.*, 2005; Koyama *et al.*, 2008b,a; Zheng *et al.*, 2009b,a), they do not compare the results with experimental results. Furthermore, previous studies have modelled particle transport in fractures utilizing an averaged *effective* dispersion coefficient, but do not account for the directionality or true physical nature of these effects (James and Chrysikopoulos, 2011; Zheng *et al.*, 2009b). Thus, a method of investigating the dispersive effects caused by fluid shear was devised whereby experiment and model may be compared (Chapter 4). The experiment minimized attachment and release of particles to the fracture wall by adding a small amount of Triton X100 to the fluid while the model neglected these effects. The local flow field is clearly defined by the geometry of the boundary (the fracture geometry) and thus, the model used in this thesis was used to investigate how the geometry of the fracture not only affected the local shear values, but also the overall path that particles travel through the fracture. The resulting simulations showed that narrowing of the fracture geometry directly affects the path particles travel through the fracture, and that these effects are difficult to describe with fracture statistics alone.

1.5 Objectives of this Thesis

The main objectives of this thesis are rooted deeply in the interplay of the geometry of the fracture on the movement of fluids and transport of two types of contaminants. Fracture geometry influences the dynamics of transport in fractures insofar as the geometry directly affects capillary pressure via apertures, local changes in elevation cause gravitational effects in two-phase flow based on fracture undulations, and the overall macroscopic angle of the fracture influencing geometric forces. In terms of a fluid flow field, the narrowing of a fracture will invariably increase the fluid velocity in order to maintain mass flow; however, the boundary condition will remain at zero velocity thus increasing shear effects and generating a rather high maximum velocity in the center of the fracture. Furthermore, eddies have been shown to form even at slow groundwater velocities ($\sim$1 m/day) which could trap contaminants. The specific objectives of this thesis are as follows:

1. The first objective of this thesis is to improve the understanding of the mechanistic effects of gravity on the invasion of DNAPL into a saturated horizontal fracture. In order to accomplish this objective, a modelling approach will be coupled with experimental results where the model will be calibrated to the experiment both with and without gravity. Then, utilizing data generated through running the calibrated simulations on hundreds of simulated fractures,

estimates of the differences between gravity included and gravity neglected simulations are collected and analyzed. Equations based on fracture statistics are empirically determined estimating the differences between simulations including and neglecting gravity (Chapter 2).

2. The second objective is to examine the effects of macroscopic fracture angle as well as geometric characteristics on flushing a fracture with water after DNAPL has invaded it. A two-phase flow model is utilized to simulate the flushing and resulting imbibition of DNAPL in hundreds of simulated fractures at varying angles. A statistical representation of the DNAPL and fracture characteristics can be used to quantify what characteristics allow for complete imbibition to occur. In particular, the goal is to understand the effects of this remediation technology on specific fracture characteristics in order to better understand the potential risks and downstream threats in fractured aquifers (Chapter 3).

3. The third objective is to further understand the effects of fracture geometry on the transport of particles with a particular focus on shear, hydrodynamic dispersion, advection and how fracture geometry may directly influence the advection process. The importance of calibrating a model to experiment is apparent as the fully calibrated model allows for a greater understanding of the effects of the physical aspects of transporting particles in fractures via analysis of the calibrated parameters. Understanding how geometry effects peak concentration and the dispersion of the contaminant in the effluent, as well as how it affects the likelihood of particle attachment to a fracture wall is valuable in assessing potential risks and appropriately managing groundwater under threat from particulate contamination (Chapter 4).

Chapter 2

On the Importance of Gravity in DNAPL Invasion of Saturated Horizontal Fractures

Abstract

Invasion percolation (IP) models of dense non-aqueous phase liquid (DNAPL) invasion into saturated horizontal fractures typically neglect viscous and gravity forces, as it is assumed capillarity dominates in many situations. An IP model simulating DNAPL invasion into saturated horizontal fractures was modified to include gravity as a local effect. The model was optimized using a genetic algorithm, and demonstrated that the inclusion of gravity is vital to achieving accurate simulations. Optimized simulations considering gravity were 80% accurate with respect to a laboratory experiment, compared to only 70% accurate without gravity. Additional simulations of

DNAPL invasion in 360 randomly generated fractures were compared with and without gravity forces. These simulations showed that with increasing fracture roughness, the minimum difference between simulations with and without gravity increases to 35% for a standard deviation of the mid-aperture field (SD_z) of 10 mm. Even for low roughness ($SD_z = 0.1$ mm), the difference was as high as 30%. Furthermore, a fracture composite ratio is defined which includes data regarding DNAPL type, media type and statistical characteristics of the fracture. The value of this composite ratio can be used to determine the conditions under which gravity should be considered when simulating DNAPL invasion in a macroscopically horizontal fracture. Finally, a set of equations defining the minimum and maximum absolute percentage difference between gravity-included and gravity-neglected simulations is presented based on the fracture and DNAPL characteristics.

2.1 Introduction

An understanding of two-phase flow in fractures is becoming increasingly important. Fractures present in geologic media provide pathways for the rapid migration of contaminants, including non-aqueous phase liquids (NAPLs), to reach groundwater. Entrapped dense non-aqueous phase liquids (DNAPLs) can become persistent sources of contamination in groundwater. Effective source zone characterization, management, and remedial strategies require an understanding of NAPL transport mechanisms in fractures. Two-phase flow in fractures is also important in oil and gas recovery, including growing interest in shale gas development and geological CO_2 storage, which require an understanding of two-phase ow in fractures to better understand extraction, injection, and potential leakage mechanisms.

Although NAPLs have been intensively studied in unconsolidated porous media, there have been comparatively few studies conducted in fractured environments. Capillary pressure, viscosity and gravitational forces govern the invasion of NAPLs in rough-walled, saturated, variable-aperture fractures. Both local and global (continuum-scale) mechanistic approaches have been employed to model NAPL invasion in saturated fractures. Reynolds and Kueper (2002) employed a global approach to model the invasion of trichloroethene (TCE) in a saturated fractured clay network by numerically solving the equations governing multiphase ow and multicomponent transport. While this global approach is advantageous over the local approach as it is able to incorporate the temporal component, it is computationally intensive and thus does not lend itself to the process of optimization (Ewing and Berkowitz, 1998). Invasion percolation (IP) is a local, more computationally efficient model that accounts for the physics of the invasion using a simple growth algorithm, thereby eliminating the need to solve systems of several equations (Ewing and Berkowitz, 1998).

The migration and entrapment of DNAPL in fractures dictates the morphology of the entrapped DNAPL, which governs the dissolution process, and ultimately controls the long-term persistence of the contaminant (Detwiler *et al.*, 2001; Yang *et al.*, 2012a). Accordingly, it is vital that the structure and morphology of DNAPL invasion is modelled accurately. IP has been used to model various physical growth processes such as capillary fingering (Wilkinson and Willemsen, 1983), gravity fingering (Glass and Yarrington, 1996; Glass and Nicholl, 1996; Glass and Yarrington, 2003), and fragmentation (Glass and Yarrington, 2003) during the invasion of one fluid by another immiscible fluid. Modifications to the IP algorithm include utilizing the local in-plane curvature and local fracture-wall topography to improve the calculation of capillary pressure by including local variations in fracture geometry (Glass and Yarrington, 1996; Glass *et al.*, 1998; Petchsingto and Karpyn, 2010). Other modifications to the IP model include simultaneously allowing both the invader to move into defender space and vice versa to account for fragmentation (reinvasion) of the non-wetting phase during the invasion process (e.g. Wagner *et al.*, 1997; Tsimpanogiannis and Yortsos, 2004; Mumford *et al.*, 2010), and the inclusion of trapping of one immiscible fluid by another (e.g. Wilkinson and Willemsen, 1983; Ioannidis *et al.*, 1996; Meakin *et al.*, 2000).

Capillary pressure is generally considered dominant in DNAPL invasion, though some IP models designed for porous media include the effects of gravity (Ewing and Berkowitz, 1998; Glass *et al.*, 1998; Meakin *et al.*, 2000; Glass and Yarrington, 2003; Mumford *et al.*, 2010) and viscous forces (Ewing and Berkowitz, 1998; Tsimpanogiannis and Yortsos, 2004). Studies in vertical fractures have also considered gravity (e.g. Glass and Yarrington, 2003; Yang *et al.*, 2013a). In these studies, the aperture midpoints are assumed to lie on a plane, the overall orientation of which is used to calculate the gravity force. Deviations of the aperture midpoints from this plane are not considered as they do not contribute significantly to the magnitude of the gravity forces. Consequently, this approach cannot be extended to macroscopically horizontal fractures, because neglecting deviations of the aperture midpoints from the horizontal fracture plane leads to neglecting gravity. In particular, this conventional approach neglects gravity in IP simulations of NAPL invasion in macroscopically horizontal fractures by treating capillary pressure as the only dominant force during invasion (Petchsingto and Karpyn, 2010; Weerakone *et al.*, 2012; Yang *et al.*, 2012a). Accounting for local gravity effects caused by variations in the aperture midpoints requires an alternate approach.

Previous studies have attempted to validate DNAPL invasion in a fracture using experimental data. Glass and Yarrington (2003) utilized a modified IP model that allowed the defending fluid (air) to reinvade against the invading fluid (water) if the capillary pressure is below a predetermined threshold. The effect of this imbibition-drainage cycle is that gravity fingering is produced with pulsation and fragmentation in a vertical fracture (Glass and Yarrington, 2003). While there is comparison to an experiment in which the IP simulation performs reasonably well against the experiment, there are distinct disagreements in shape between simulation and experiment. Petchsingto and Karpyn (2010) utilized a capillary-driven IP model that neglected gravity and viscous forces to simulate NAPL invasion in a saturated fracture based on geometry from a real fracture. An NAPL invasion experiment was performed in the real fracture and the simulation was able to predict the NAPL invasion pattern with 70% accuracy (Petchsingto and Karpyn, 2010). In this case, capillary forces were considered dominant and the inclusion of gravity was not necessary to accurately simulate invasion in a horizontal fracture. More recently, Weerakone *et al.* (2011) utilized a finite difference continuum-scale model to attempt to model an experiment in which DNAPL was injected into a brine-saturated horizontal fracture. In this case, the model failed to simulate the observed invasion pattern and the authors indicated that local undulations in the mid-aperture field neglected in the model were likely the cause of the discrepancy (Weerakone *et al.*, 2011).

The objectives of this study are to: i) modify an IP model to include gravity forces at the local scale, ii) calibrate the modified model by comparison to a DNAPL invasion experiment into a water-saturated horizontal fracture using optimized model parameters; and iii) develop a criterion based on fracture statistics and DNAPL properties to estimate the percentage difference between the DNAPL invasion pattern when including versus neglecting gravity. This criterion is developed by comparing the model used in this study to simulate DNAPL invasion in randomly generated fractures to simulations of invasion using the conventional model.

2.2 Methods

IP Model Conception

IP algorithms are often used to simulate immiscible fluid invasion into porous media, and modifications have also been made to examine immiscible fluid invasion into fractures (Glass and Yarrington, 1996; Petchsingto and Karpyn, 2010). When considering the invasion of a saturated fracture by an immiscible uid, the original saturating fluid is denoted as the defender and the invading fluid is denoted as the invader. Applying an IP model to a fracture requires discretization of the fracture into elements along the fracture plane with an aperture and elevation assigned to each element. The IP algorithm considers the interface between the invader and defender, in this case the non-wetting and wetting fluids respectively, computes the pressure required to invade each adjacent element, and the invader "invades" the element with the lowest invasion pressure. The algorithm then repeats this computation and invasion step for each new interface location (Glass and Yarrington, 1996; Ji *et al.*, 2003; Glass *et al.*, 2004; Petchsingto and Karpyn, 2010). In this work, the invasion pressure is computed as a sum of the capillary pressure, P_c, and the gravitational pressure, P_g (Glass and Yarrington, 1996; Ioannidis *et al.*, 1996; Meakin *et al.*, 2000). P_c is calculated as follows:

$$P_c = \frac{\alpha\sigma\cos(\theta)}{b} \tag{2.1}$$

where σ is the interfacial tension, θ is the contact angle, b is the aperture, and α is a fitting parameter that accounts for the variable aperture geometry. Equation 2.1 represents a simplification of the Young-Laplace equation, where $\alpha = 2$ if the local aperture geometry is two parallel plates (Glass and Yarrington, 1996; Ji *et al.*, 2003; Glass *et al.*, 2004) and $\alpha = 4$ if the local interface geometry is a tubular pore (Kueper and McWhorter, 1991; Glass and Yarrington, 1996). It is expected that the value of α is between 2 and 4 as a fracture is neither a parallel plate nor tubular pore (Kueper and McWhorter, 1991). The model accounts for gravity as follows:

$$P_g = \Delta\rho g \Delta z \tag{2.2}$$

where $\Delta\rho = \rho_{inv} - \rho_{def}$ is the difference in densities between the invading and defending fluids, g is the acceleration due to gravity and Δz is the elevation difference between the aperture midpoints of the possible invasion elements and the invader, namely $\Delta z = z_{def} - z_{inv}$ (Corey, 1986; Glass *et al.*, 2001). In previous studies that utilize gravity in vertical fractures, Δz is simply the resolution of the fracture elements or 0 if the invasion proceeds laterally. In this study in a horizontal fracture, the aperture midpoint is defined locally at each element and can vary between adjacent elements, thus it must be computed for every potential invasion element from each invading element. In each step, the IP algorithm permits the invasion of the element with the least pressure, computed by summing P_c and P_g as follows:

$$P_I = \frac{\alpha\sigma\cos(\theta)}{b} + \Delta\rho g \Delta z \tag{2.3}$$

where P_I denotes total invasion pressure required to completely invade a potential invasion element. In this case, the capillarity part of equation 2.3 is always positive. In a horizontal fracture, Δz is negative if the invader is higher in elevation than the potential invasion element (defender), whereas Δz is positive if the invader is lower in elevation than the potential invasion element. During DNAPL invasion in a water saturated fracture, if the invading DNAPL is higher than the water saturated potential invasion element ($\Delta z < 0$), then the invasion pressure is lowered promoting DNAPL invasion; however, if the invading DNAPL is lower than the potential invasion element ($\Delta z > 0$), then the invasion pressure is raised thus lowering the likelihood of invasion.

In other IP models, typically only one element is invaded with each step (Glass and Yarrington, 1996; Ji *et al.*, 2003; Glass *et al.*, 2004; Petchsingto and Karpyn, 2010). In this study, the number of elements invaded within a single step is denoted as N. To account for increased viscous forces that stabilize invasion fronts, Ewing and Berkowitz (1998) modified the typical IP model by still allowing the invasion of single element, but choosing that element randomly between several potential elements rather than selecting the most favourable element in each step. In a previous study by Glass *et al.* (2001), a related modification was made, in which N elements with the lowest pressures were invaded during each step . It was found that increasing N increases the local saturation of the invading fluid by widening invasion fingers; this study did not, however, search for an optimal N value. This modification from the typical one element per step method attempts to model the effect of viscous forces decreasing the randomness associated with the local variations in the aperture at the invasion front while ultimately thickening the local DNAPL pooling (Glass *et al.*, 2001). This modification was included in this study; however, N was used as a parameter used for calibration. (Glass and Yarrington, 1996) allow for a single invasion step while also allowing for the defending fluid to simultaneously step back into the invader space in order to account for fragmentation in porous media. The model used in this study also considered trapping of the defender, where elements not connected to a flow boundary are removed from the list of potentially invaded elements (Wagner *et al.*, 1997; Glass and Yarrington, 2003; Tsimpanogiannis and Yortsos, 2004). As no small regions of trapped water (defender) were observed in the physical experiment (Figure 2.1a), if the defender was trapped in a single element, then this element was considered to be invaded.

Experimental Methodology

An approximately 14 cm $\times$ 23 cm $\times$ 3.5 cm rock sample was removed from a dolomitic limestone outcrop and a tension fracture was induced in the sample using the technique described by Reitsma and Kueper (1994). To enable the visualization of DNAPL invasion, a transparent cast of each fracture face was fabricated, using a transparent epoxy (Stycast 1269A, W.R. Grace Co.); the fracture faces were then mated to replicate the fracture plane.

The DNAPL invasion experiments involved first saturating the fracture cast with degassed water dyed red. DNAPL invasion was induced by setting a pressure gradient across the fracture using a Marriott bottle on the influent end and fixing the elevation of the spigot on the effluent end. The DNAPL, HFE 7100, was then released into the fracture under a constant head, and photographs were taken throughout the experiment to record the invasion pattern. The head difference across the fracture was recorded throughout the experiment using inclined piezometers. Further details regarding the DNAPL invasion experimental methodology are provided in Dickson and Thomson (2003). The physical properties of the fluids in these experiments were measured as follows: the contact angle of water (with respect to the epoxy and HFE 7100) $\theta = 81^{\circ}$, ρ_{water}=996.7 kg/m^3, $\rho_{HFE7100}$=1520 kg/m^3 and the interfacial tension, σ=42.4 dynes/cm. It should be noted that since the contact angle of HFE 7100 is near 90°, gravity will be more important relative to capillary pressure (equation 2.3) thus helping to elucidate upon the effects of gravity on the invasion of DNAPL in a horizontal fracture.

To characterize the fracture, each face was laser scanned using a Roland LPX600 (Roland DG, Shinmiyakoda, Japan) to generate a three dimensional model of the aperture field with a resolution of 0.2 mm $\times$ 0.2 mm. Because the casts had to be separated for scanning, determining the aperture field for use in the simulations required that the fracture wall scans of both casts be aligned such that the simulated volume matched the volume of the fracture in the experiments. This volume in the experiments was obtained by measuring the time and flow rate required to fill the mated fracture with water, and was found to be 53.8 $\pm$ 2 cm^3. To match this volume, a genetic algorithm (Haupt and Haupt, 1998) was employed, using Matlab (R2011b, Math Works Inc., Natick, MA, USA). The matched alignment was obtained using a discretization of 2 mm $\times$ 2 mm (i.e., scanned values at a resolution of 0.2 mm were averaged to obtain up-scaled values at a resolution of 2 mm). This discretization was chosen as the optimization of the IP model parameters required several hundred iterations, and 2 mm elements provided a reasonable fracture resolution while maintaining practical run times of a few weeks per optimization.

IP Model and Experiment Comparisons

DNAPL invasion under constant head in variable aperture fractures is a dynamic process, as capillary pressure depends on aperture size (equation 2.1), which changes as the interface progresses through the fracture. Along the invasion front, local changes in elevation contribute to gravitationally related changes in entry pressures and viscous forces related to local DNAPL migration velocity may also have an effect on the local pressures. The effects of the three forces can cause local dynamic effects such as pulsation and fragmentation (Glass and Yarrington, 2003; Glass *et al.*, 2000). Therefore, the goal of the simulation was to replicate the final state of the experiment rather than the dynamic progression of the interface through the fracture. The final photograph of the DNAPL invasion experiment (Figure 2.1a) was turned into a binary image (Figure 2.2a) using a 2 mm resolution to enable comparisons between the DNAPL and water locations between the IP simulations, and the experimental observations. The accuracy of the simulations was determined by:

$$A = 1 - \frac{\sum |S_{i,sim} - S_{i,exp}|}{n_t} \tag{2.4}$$

where A is the accuracy of the simulation, n_t is the total number of elements, $S_{i,sim}$ is the water saturation of the ith element in the simulations, and $S_{i,exp}$ is the water saturation of the ith element in the experiments; both have values of 1 or 0 if occupied by water or DNAPL, respectively.

Two cases of the IP model were considered in this paper to determine the effects of gravity. Case 1, representing the conventional model, neglected the second term on the right-hand side of equation 2.3 in the calculation of the total pressure of each potential invasion element, which is equivalent to assuming negligible height difference between aperture regions ($\Delta z = 0$) such that the total pressure is given only by capillary pressure (i.e., $P_I = P_c$). Case 2, representing the gravity-modified model, considered both capillary pressure and gravity in the calculation of the total pressure (i.e., $P_I = P_c + P_g$). During model calibration to the experimental results, fluid density, contact angle and interfacial tension were measured independently and inputted into the model. As well, the aperture field and mid-aperture field were determined from the optimized fracture face matching and were utilized in the simulations for invasion pressure computations. The two remaining model parameters, α and N, were set as calibration parameters (Table 2.1, Model Calibration). A genetic algorithm written in Matlab was used to optimize the parameter N in the conventional model, and N and α in the gravity modified model by maximizing the accuracy (equation 2.4)(Haupt and Haupt, 1998). Optimization of α was not necessary in the conventional model as it only scales P_c with respect to P_g.

Synthetic Fracture Generation and Simulations

The importance of considering gravity was further explored by conducting IP simulations in synthetic fractures in the second and third parts of this study (Table 2.1). In particular, examination of the differences between the model used in this study and the conventional model was undertaken in two steps: i) the percentage difference between models versus the mid-aperture field standard deviation (SD_z) using two DNAPL and fracture material combinations; and ii) the percentage difference between models versus a single value made up of fracture statistics and DNAPL physical properties using six DNAPL and fracture material combinations (Table 2.1). In both the second and third parts of this study, simulated fractures were utilized to generate data for analysis.

The simulated fractures were generated using Matlab code based on SPRT2D (Gutjahr, 1989; James and Chrysikopoulos, 2000; Zheng *et al.*, 2009a). The synthetic fracture generation was performed using different combinations of aperture field distribution (normal or log-normal), mean aperture (μ_b), aperture field standard deviation (SD_z), aperture field correlation length (λ_b), SD_z, and mid-aperture field correlation length (λ_z) totaling 84 possible combinations (Table 2.2). Three replicates of each combination of field statistics were created for a normally distributed aperture field giving 252 synthetic fractures. The discretization and experimental domain were consistent with the experimental fracture at 2 mm and 14 cm $\times$ 23 cm respectively. A random sample of 138 synthetic fractures was selected from the 252 generated synthetic fractures, and DNAPL invasion was simulated for each using both conventional model (gravity neglected) and gravity-modified simulations. Considering the five values of α and the 138 fractures, the total number of conventional model and gravity modified simulation pairs for a given DNAPL in a given fracture was 690. For each pair of simulations, the differences between simulations using the conventional model and the model used in this study were calculated using equation 2.4, where the gravity-included results were treated as the reference state and the accuracy is referred to here as a difference.

The second and third parts of this study were performed under two and six different DNAPL-fracture material conditions respectively (Table 2.1) with density, contact angle and interfacial tension given in Table 2.3. DNAPL and interface types were selected to provide breadth in simulation conditions. As well, HFE 7100 in epoxy was used in the simulations.

Some media and DNAPL characteristics have been simplified into a single number representing the ratio of gravity forces to capillary forces, the Bond Number (Bo). Pennell *et al.* (1996) defined Bo as follows:

$$Bo = \frac{k \Delta \rho g}{\sigma \cos \theta} \tag{2.5}$$

where the permeability, k, is the square of a characteristic length related to the fracture (in cm^2) and chosen to be equal to μ_b^2 for the purposes of this study. $\Delta\rho$ is the difference in density between the DNAPL and water (in g/cm^3), σ is the interfacial tension (dynes/cm), and θ is the contact angle. Furthermore, SD_z and SD_b were included as additional fracture characteristics resolving in a ratio representing the effects of gravity to the effects of capillarity, R:

$$R = Bo \frac{SD_z}{SD_b} \tag{2.6}$$

where SD_z and SD_b are in cm. R is a dimensionless number including information regarding the DNAPL, fracture interface material and fracture statistical characteristics.

2.3 Results

IP Model and Experimental Comparisons

Figure 2.1 shows the mid-aperture field and the aperture field of the discretized experimental fracture, as well as the experimental invasion pattern of the DNAPL into the fracture. The mid-aperture field is shown in Figure 2.1b, and the resultant aperture field is shown in Figure 2.1c. The aperture field was normally distributed with $\mu_b = 1.8$ mm and $SD_b = 0.7$ mm. In natural subsurface formations, Cady *et al.* (1993) found mass balance apertures of approximately 1.5 mm in dolomite, while Snow (1970) directly measured fracture apertures from 29 different sites and various rock types measuring from 1.5 to 2 mm; thus, the mean aperture of the fracture utilized in this study is akin to what is found naturally in the subsurface. A fracture with large mean aperture was selected for this study as this would encourage any gravitational effects during invasion. It is apparent that there is great variability and undulation in the mid-aperture field (Figure 2.1b, $SD_z = 4.5$ mm) suggesting that gravity is of importance in modelling the invasion of DNAPL into the water-saturated horizontal fracture.

Figure 2.2 depicts the digitized representation of DNAPL invasion in the experimental fracture (Figure 2.2a) along with simulation results from the conventional model (Figure 2.2b) and the gravity modified model (Figure 2.2c). The simulation results for the optimized conventional model (N=5) produced an accuracy of 70% (Figure 2.2b). In this case, the model failed to capture the overall shape of the invaded DNAPL. Particular regions of note are shown in Figure 2.2a. The simulation was unable to duplicate the DNAPL in region I, the trapping of water in region II, and the DNAPL pinch-point in region III. Furthermore, the simulation predicted substantial DNAPL invasion in region IV, which did not occur in the experiment. Errors associated with regions I and IV are attributed to neglecting gravity, as the smaller apertures in region I were at lower elevations and the larger apertures in region IV were at higher elevations (Figures 2.1b and c). There was good agreement between the simulations and experiments in region V, where larger apertures coincided with lower elevations (Figures 2.1b and c). A comparison of the distribution of apertures invaded by DNAPL shows that when gravity is included in the model, on average smaller apertures are invaded (data not shown). This effect is due to the spatial relationship of the aperture field (induces capillary pressure) and the mid-aperture field (induces pressures caused by gravitational forces) combining to mitigate the effects of only considering the aperture field (conventional model) (Figures 2.1b and c).

The simulation results for the optimized gravity modified model (N=4, $\alpha = 2.7$) produced an accuracy of 80% and provided a more accurate representation of the major features observed in the experiment (Figure 2.2c). The best-fit $\alpha = 2.7$ (equation 2.3) indicates that the fracture geometry lies between the parallel plate ($\alpha = 2$) and tubular ($\alpha = 4$) geometries. This notion is intuitively correct, as the geometry of a fracture aperture field is undulous; the void space is neither a parallel plate nor a tubular pore. In a fracture, the parameter α would be locally defined depending on the local geometry of the fracture and the invasion front. In order to reduce computation intensity, this model treated α as an aperture field averaged property. Unlike the conventional model simulation, the gravity modified simulation predicted DNAPL in region I, trapped water in region II, the presence of a pinch-point near region III, and no DNAPL in region IV. Although the pinch-point near region III was predicted, it was not localized in the correct position and it is speculated that the relatively large resolution of the discretization scheme (2 mm $\times$ 2 mm elements) may be a cause. The increased accuracy, particularly in these key regions, is attributed to including gravity in the total pressure required for DNAPL invasion. As in the conventional model, good agreement is achieved in region V. The inclusion of gravity was not sufficient to correct the presence DNAPL in region VI predicted by both the conventional model and gravity modified simulations, which occurs in a larger aperture region (Figure 2.1c). Also, neither case displays the smooth DNAPL invasion pattern observed in the experiment which may also be due to the resolution of the fracture data. While the smooth invasion pattern is not ideally replicated by the optimized simulation, the inclusion of gravity in the simulation (Figure 2.2c) produces a far more accurate model than the simulation neglecting gravity (Figure 2.2b), thus showing the importance of considering gravity when modelling DNAPL invasion in a horizontal fracture.

A local sensitivity analysis was performed by perturbing each parameter (N or) while holding the other parameters constant and evaluating the accuracy of the model output (equation 2.4). The value for α was perturbed by up to 10% and N by up to 75%. Accuracy was found to be reduced by a maximum of 4% for α, and less than 4% for N. Therefore, while α is the most sensitive parameter, the IP model is not very sensitive overall.

Relative Effect of Gravity on Invasion

The optimal model settings (N=4, α=2.7) were utilized to further investigate the impact of gravity on the invasion of DNAPL in a horizontal fracture. At each invasion step, the absolute value of the ratio of P_c to P_g was recorded. Figure 2.3 displays the histogram of $|P_c/P_g|$ values and shows that approximately 80% of the $|P_c/P_g|$ ratios fall between 1 and 10, whereas less than 10% of the $|P_c/P_g|$ ratios fall between 0 and 1. This suggests that capillary pressure is generally dominant over gravitational forces although in the majority of iterations, P_c is within an order of magnitude of P_g.

To gain insight as to when P_c dominates P_g, the IP model was set to utilize the optimal parameters from case 2 (N=4, α=2.7), and the total pressure was computed using the function:

$$P_I(x) = \begin{cases} P_c + P_g & \text{if } |P_c/Pg| \leq x \\ P_c & \text{if } |P_c/Pg| > x \end{cases} \tag{2.7}$$

Therefore, gravity is included in the model when $|P_c/P_g|$ is greater than or equal to a specified ordinate value, x, of $|P_c/P_g|$ (Figure 2.4). A simulation was run for each of 160 different x values ranging from 1 to 200. The accuracy (equation 2.4) of each simulation was plotted against the specified x value. Therefore, gravity is included in the simulations plotted on Figure 2.4 when P_c is less than x times greater than P_g. As gravity is increasingly included in the model (as the x ordinate increases), the accuracy values tend to a plateau at the optimal 80% value. Moreover, the maximum accuracy is not achieved until capillary pressure is 2 orders of magnitude larger than gravitational pressure. Thus, even when P_g is small compared to P_c, the inclusion of P_g is still vital in providing the best prediction of DNAPL invasion and location in this horizontal fracture.

Figure 2.5a shows the difference between the conventional model and gravity modified simulations were plotted against the SD_z conducted using the selection of 138 fractures for HFE 7100 invasion. As expected, the conventional model simulations show greater discrepancy from the gravity included model in more undulous fractures (i.e. those with lower mid-aperture field standard deviations). However, even in the less undulous fractures, the error in accuracy caused by neglecting gravity can be substantial, as high as 30% for the conditions tested here. In addition, as the SD_z, the effect of neglecting gravity increases, causing differences between 35% and 50%.

It is noteworthy that the contact angle of the DNAPL employed in the physical experiments is 81° thus causing capillary pressure values to be smaller (equation 2.1) than that for many DNAPLs found in the subsurface. For example, the contact angle in a PCE, water, dolomitic limestone system is 20° which results in capillary pressures six times larger than a contact angle of 81°; this is well below the two orders of magnitude required to dominate the gravitational forces found in the experimental fracture (Figure 2.4). To demonstrate this point, the simulations conducted for Figure 2.5 a were also conducted using a PCE in a dolomite fracture (contact angle of 20°) (see Table 2.3 for other constants). A similar trend was observed in both systems with the error in accuracy caused by neglecting gravity ranging from 13% to 45% in the roughest fractures (Figure 2.5b).Furthermore, even in the smoothest fractures, the error in accuracy can be as high as about 22%. It should be noted that the percentage difference between the conventional model and the model used in this study (× in Figure 2.5a) produced a result consistent with the simulated fracture data.

In order to generate estimates for when gravity may be neglected in an IP model of DNAPL invasion, the percentage difference between the conventional model and gravity modified simulations in the 138 fracture set were conducted with five values of α and for six different DNAPL-fracture characteristics (Table 2.3). Figure 2.6 shows the percentage difference between the conventional model and gravity modified simulations (equation 2.4, with the gravity included simulation used as the reference invasion pattern) plotted against the natural logarithm of R (equation 2.6). An increase in the value of R implies the increase of the importance of gravity in DNAPL invasion. Accordingly, these results show that as R increases the minimum and maximum differences between conventional model and the gravity modified model increase. Varying values of α does not seem to have a significant impact on the percentage difference results in horizontal fractures.

To estimate the minimum and maximum percentage differences between no-gravity and gravity included simulations, the boundaries of the simulation data were fitted with the logistic equation (Figure 2.6).

$$PD = \frac{c_1}{1 + c_2 \exp\left(c_3 lnR\right)} \tag{2.8}$$

where c_1, c_2, and c_3 are constants.

The minimum percentage difference between no-gravity and gravity included simulations, PD_{min}, based on the composite ratio, R, is estimated by (after simplification):

$$PD_{min} = \frac{37.0\%}{1 + 11.358R^{-0.835}} \tag{2.9}$$

The maximum percentage difference between no-gravity and gravity included simulations, PD_{max}, is estimated by:

$$PD_{max} = \frac{46.3\%}{1 + 1.596R^{-0.761}} \tag{2.10}$$

Implicit in equations 2.6, 2.9 and 2.10 is that the DNAPL and fracture characteristics used in the equations must be within the bounds of the characteristics used in the generation of simulation data (Table 2.3). For example, in a simulation where PCE invades a fracture in dolomite (Table 2.3), where the fracture has the characteristics μ_b=0.1 cm, SD_b=0.02 cm, and SD_z=0.08 cm, then R = 0.049 and the maximum difference between gravity included and no-gravity simulations is PD_{max} = 13.6%. In this instance, it is possible to neglect gravity in the simulation. Alternatively, in a simulation where chloroform invades a clay fracture (Table 2.3), where the fracture has the characteristics μ_b=0.03 cm, SD_b=0.001 cm, and SD_z=0.6 cm, then R = 0.659 and the minimum and maximum differences between gravity included and conventional model simulations is PD_{min} = 12.3% and PD_{max} = 34.8% indicating that inclusion of gravity is necessary in the simulation.

2.4 Conclusions

We have shown that it is possible to optimize an IP model for the invasion of DNAPL into a horizontal fracture using a genetic algorithm and the resulting invasion output maintains many of the key features shown experimentally. In particular, the optimization has yielded the value of α=2.7 as the optimal coefficient to use when computing capillary pressure based on the Young-Laplace equation (equation 2.1). Moreover, it was shown that including pressure caused by gravitational head is vital to producing a good model of the invasion of DNAPL in a horizontal fracture despite pressure due to gravity generally being considered negligible compared to capillary pressure in horizontal fractures (Glass and Yarrington, 1996; Weerakone *et al.*, 2012; Petchsingto and Karpyn, 2010; Yang *et al.*, 2012a). In particular, gravity is important in how the model selects the invasion path, even when it is up to two orders of magnitude smaller than capillary pressure. More to this effect, examining a set of simulated fractures shows that even at low midpoint aperture elevation variability, neglecting gravity can produce far different simulated DNAPL invasions from simulations including gravity (up to 50% difference). Further investigation showed that a criterion based on the ratio, R (equation 2.6), can discern whether or not gravity should be included in DNAPL invasion simulations (equations 2.9 and 2.10) based on the DNAPL, type of media in which the fracture exists and 3 statistical characteristics of a fracture aperture field mean, aperture field standard deviation and elevation field standard deviation.

Chapter Contents

The contents of this chapter are in preparation for submission. The authors are Sean P. L. Cianflone, Sarah E. Dickson, and Kevin G. Mumford.

Table 2.1: Simulation Conditions

Experiment	**Fracture Type**	**DNAPL-Fracture**	α	**N**
Model Calibration	Experimental $\mu_b = 1.8$ mm $SD_b = 0.7$ mm $SD_z = 4.5$ mm	HFE 7100-Epoxy	Calibrated	Calibrated
Percentage difference vs. SD_z (Figure 2.4)	Simulated; random sample of 138 fractures (Table 2.2)	HFE 7100-Epoxy PCE-Dolomite	2.5, 2.75, 3 3.25, 3.5	4
Percentage difference vs. R (Figure 2.5)	Simulated; random sample of 138 fractures (Table 2.2)	Table 2.3	2.5, 2.75, 3 3.25, 3.5	4

Table 2.2: Simulated Fracture Statistics

Aperture Distribution	μ_b **(mm)**	SD_b **(mm) possibilities**	SD_z **(mm) possibilities**	λ_b **(mm)**	λ_z **(mm)**
normal	0.75	0.01, 0.05, 0.1	0.1, 0.5, 1, 2.5, 5, 10	10	100
normal	1.50	0.01, 0.05, 0.1, 0.25	0.1, 0.5, 1, 2.5, 5, 10	10	100
log-normal	0.75	0.01, 0.05, 0.1	0.1, 0.5, 1, 2.5, 5, 10	10	100
log-normal	1.50	0.01, 0.05, 0.1, 0.25	0.1, 0.5, 1, 2.5, 5, 10	10	100

Table 2.3: DNAPL Characteristics (All data from Cohen *et al.* (1993))

DNAPL	**Fracture Interface**	**Density (g/cm^3)**	**Wetting Angle (°)**	**Interfacial Tension (dynes/cm)**
PCE	Dolomite	1.623	20	44.4
PCE	Silica	1.623	40	44.4
Carbon Tetrachloride	Clay	1.593	27	45.0
Chlorobenzene	Clay	1.105	34	37.4
Chloroform	Clay	1.402	30	32.8

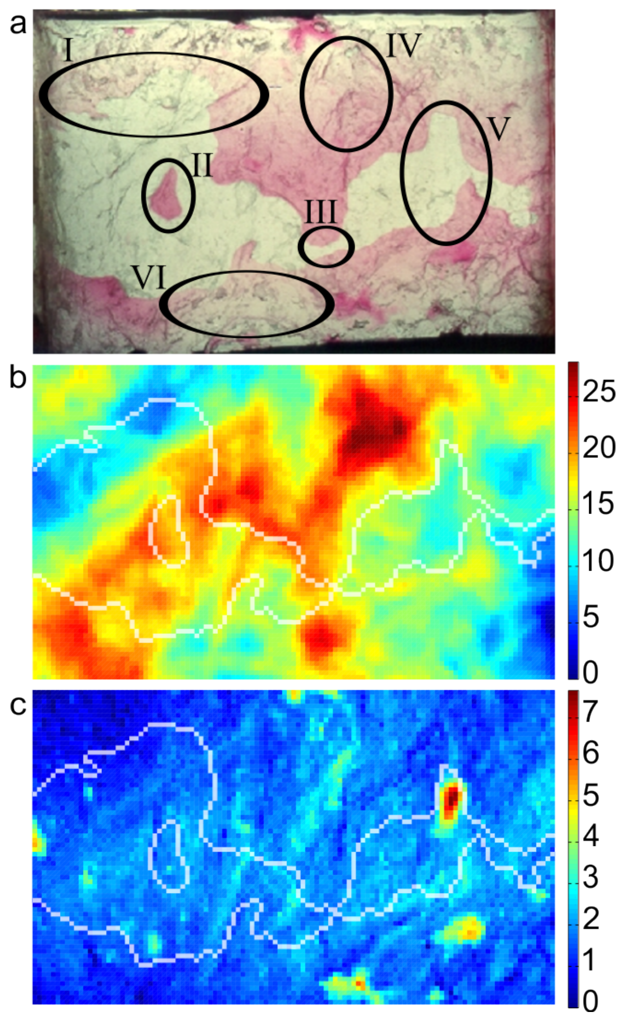

Figure 2.1: A) A heat map of the heights of the midpoint aperture elevation of the fracture (colour map in mm). The final state of the invaded DNAPL is shown as a translucent white outline. B) A heat map of the aperture field of the fracture (colour map in mm). The final state of the invaded DNAPL is shown as a translucent white outline. C) A photo of the final state of the invaded DNAPL experiment (DNAPL is clear, water was dyed red using red food colouring). Important regions are shown as labelled black ellipses.

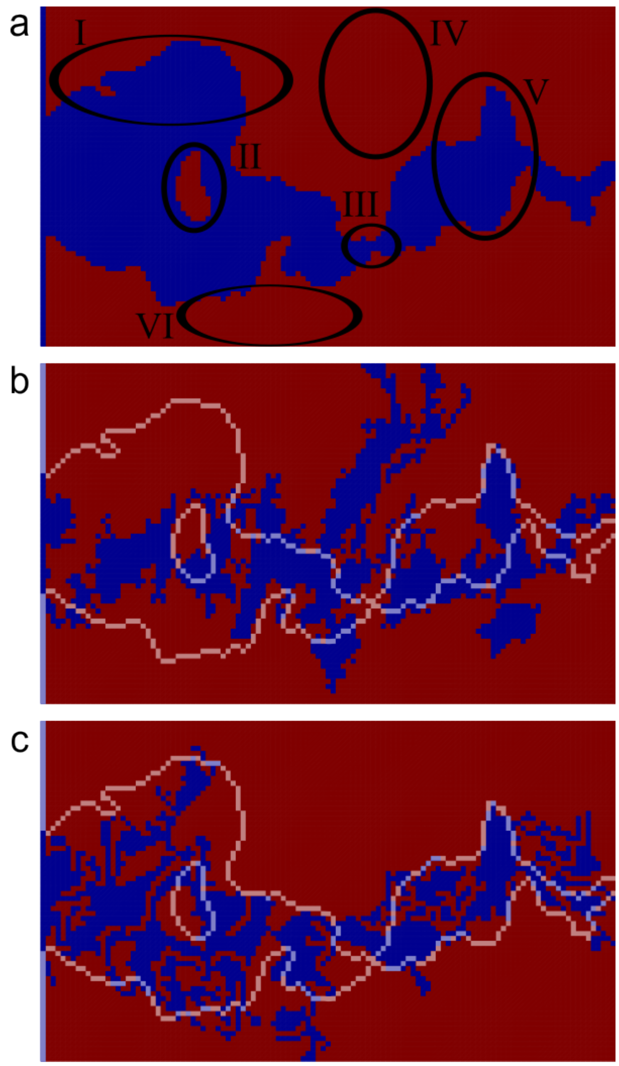

Figure 2.2: A) A binary digital representation of the end point of invasion of the transparent fracture by HFE 7100 (blue). Here water is shown in red. Important regions are shown as labelled black ellipses B) End point of the most accurate IP simulated invasion of the fracture by HFE 7100 (blue) with gravity not considered (ie. $P_g = 0$). Water is displayed as red. The final state of the invaded DNAPL is shown as a translucent white outline. C) End point of the most accurate IP simulated invasion of the fracture by HFE 7100 (blue) with gravity considered. The final state of the invaded DNAPL is shown as a translucent white outline.

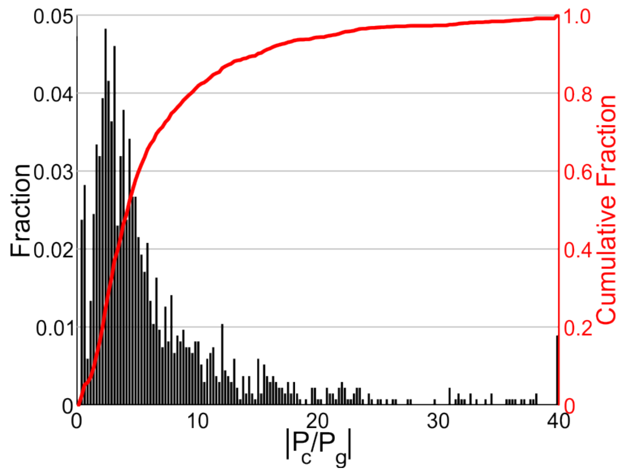

Figure 2.3: Histogram of the ratio of the absolute value of capillary pressure (P_c) to pressure due to gravity (P_g) for all invasion steps of the most accurate IP simulation (includes gravity) in the digitized experimental fracture. The red line represents the cumulative fraction below the $|P_c/P_g|$ (x-axis) value.

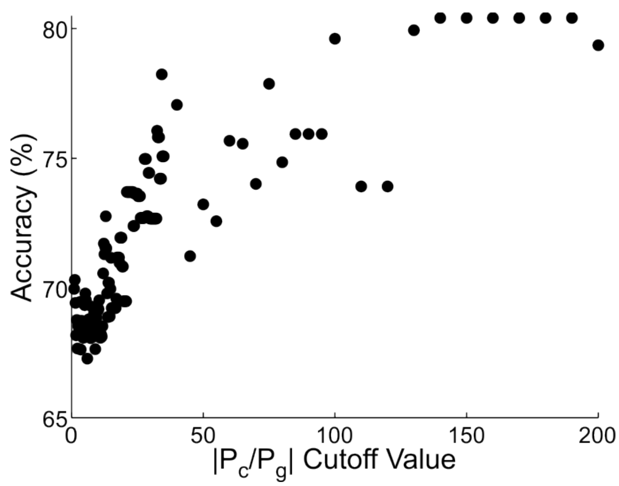

Figure 2.4: In each step of the IP simulation (using the most optimal parameters), the ratio P_c/P_g was computed and if $|P_c/P_g|$ is less than the x-axis value, then P_g is included in the invasion step calculation, otherwise P_g is set to 0 (see equation 2.7). As $|P_c/P_g|$ increases, P_g is more frequently included.

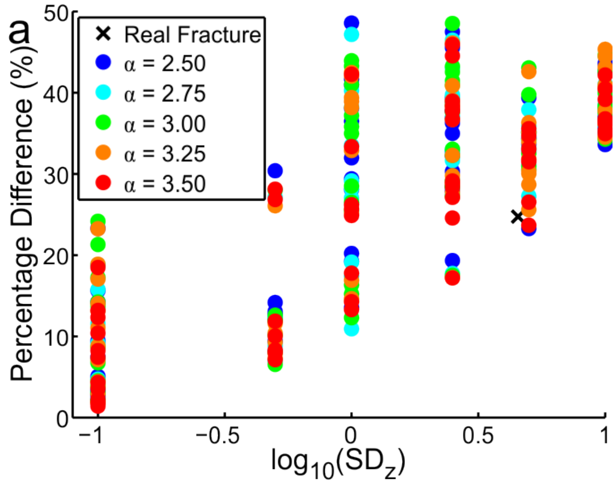

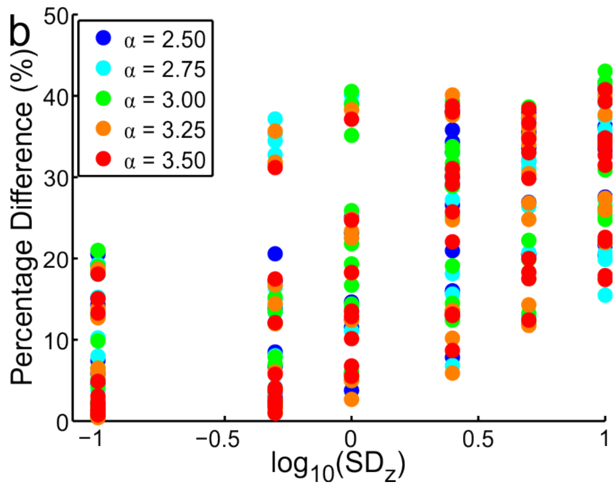

Figure 2.5: A) Percentage difference between no-gravity and gravity included simulations for generated fractures with varying values with HFE 7100 invading the water saturated fracture. SD of the midpoint aperture field is plotted on the x-axis. B) Percentage difference between no-gravity and gravity included simulations for generated fractures with varying values with PCE invading the water saturated dolomite fracture. SD of the midpoint aperture field is plotted on the x-axis.

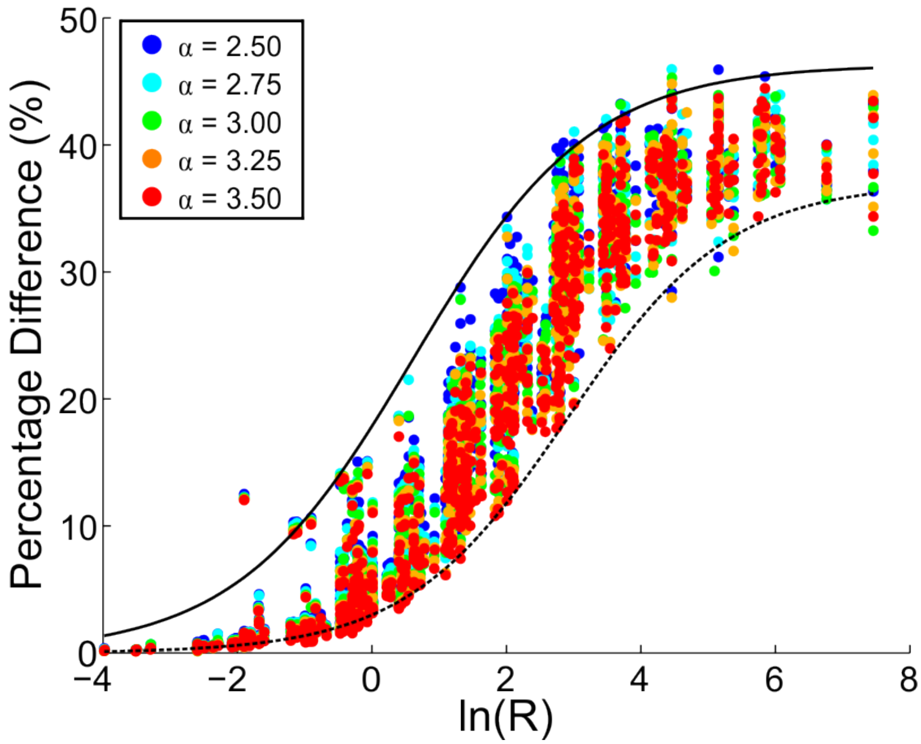

Figure 2.6: Results of 4140 simulations comparing no-gravity versus gravity included simulations considering multiple DNAPL invasion scenarios (Table 2.3). Using the natural logarithm of R (equation 2.6), it is possible to fit a logistic equation to estimate the lower (---) and upper (—)bounds of the differences between no-gravity and gravity included scenarios to allow for determining possible errors when neglecting gravity based on DNAPL and fracture characteristics.

Chapter 3

Effects of fracture angle, aperture and mid-aperture field statistics on DNAPL entrapment in fractures

Abstract

This work investigates trapped DNAPL saturation in variable aperture fractures using an invasion percolation approach to simulate imbibition in a set of single, DNAPL-saturated fractures. The relationship between the trapped DNAPL saturation, aperture field statistics and fracture orientation was investigated by varying a number of parameters; overall, 52 992 simulations were completed. The standard deviation and arithmetic mean of the apertures were varied from 0.01-0.3 mm and 0.5-1.5 mm, respectively. The standard deviation and correlation length of the mid aperture field were varied from 0.01-10 mm and 5-50 mm, respectively. The fracture orientation was varied from 60° above (inclined) to 60° below (declined) horizontal.

The results demonstrate that: 1) depending on aperture field and mid-aperture field statistics, declined fractures permit the possibility of little to no retained DNAPL in the fracture, and complete removal of DNAPL can only occur with a coefficient of variation less than 0.1; however, DNAPL is always retained in horizontal and inclined fractures regardless of aperture field statistics; 2) when the coefficient of variation of the aperture field is larger than 0.1 the fracture orientation has little effect on the trapped DNAPL saturation when compared to the horizontal case; 3) increasing standard deviation of the mid-aperture field increases the range of the trapped DNAPL saturation; and 4) equations estimating the minimum and maximum trapped DNAPL saturation based on aperture field statistics together with physical properties of the DNAPL are developed.

3.1 Introduction

Contamination of groundwater by dense non-aqueous phase liquids (DNAPLs) is generally related to releases from industrial and storage facilities (Darwish *et al.*, 2003). DNAPLs of concern include chlorinated solvents, which can be carcinogenic, coal tars and heavy crude oil (Darwish *et al.*, 2003; Kueper and McWhorter, 1991; Mackay and Cherry, 1989; Yang *et al.*, 2012a). When DNAPLs migrate into the subsurface, they can become trapped and despite being generally immiscible, small volumes do dissolve and can contaminate large volumes of groundwater at levels greater than regulated standards. Thus, the trapped DNAPL can become a persistent source of contamination (Mackay and Cherry, 1989; Yang *et al.*, 2012a).

Hydraulic displacement of DNAPLs by flushing with water is often undertaken when DNAPL is present (Darwish *et al.*, 2003; Kueper *et al.*, 2014) as a first step in the remedial process. The mass remaining post-flush is typically difficult to mobilize, and many remedial techniques used to target immobile mass focus on DNAPL present in the aqueous phase. These remedial strategies are relatively slow, as they rely on the DNAPL dissolving into the aqueous phase, which is a fundamentally slow process. One common remedial strategy focusing on dissolved DNAPL is the addition of highly oxidative chemicals, such as potassium permanganate or hydrogen peroxide, to the DNAPL plume (Kueper *et al.*, 2014). However, the amount of oxidative chemical required is based on an estimation of the volume of trapped DNAPL. This information is also required in the design of other remedial strategies targeting dissolved DNAPL, and developing long-term management strategies for DNAPL plumes. While interfacial tracers have been employed to estimate the volume of trapped DNAPL in unconsolidated aquifers (e.g. Annable *et al.*, 1998; Hartog *et al.*, 2010; Jawitz *et al.*, 2000; Jin *et al.*, 1995), this approach is resource intensive, and there are questions surrounding accuracy in field situations (e.g. Culligan *et al.*, 2004, 2006; Rao *et al.*, 2000). A better understanding of the relative importance of the mechanisms controlling DNAPL entrapment in fractured media is a first step towards estimating or predicting the mass of DNAPL trapped in fractures following a hydraulic flush.

While considerable research has been done on the transport of DNAPLs in unconsolidated porous media, comparatively little research has been done in fractured media. DNAPL migration in fractured media is governed by capillary, gravity and viscous forces. These forces are affected by the surface properties of the matrix, physical properties of the fluid(s) involved, and the aperture field and mid-aperture field characteristics (Hakami and Larsson, 1996; Darwish *et al.*, 2003; Ewing and

Berkowitz, 1998; Yang *et al.*, 2012a). Yang *et al.* (2012a) found that increasing aperture standard deviation (SD_b) and decreasing correlation length in fractures increased the saturation of entrapped DNAPL. Longino and Kueper (1999) studied non-wetting retention in two fractures experimentally using tetrachloroethene (PCE) and found there was a decrease in retention with decreasing fracture angle. As well, it was found that despite waterflooding the fractures, the non-wetting phase was never completely removed (Longino and Kueper, 1999). Longino and Kueper (1999) focused on two fractures and one DNAPL; however, this study suggests a larger scope may elucidate further upon DNAPL retention mechanisms in fractures. It is difficult to observe the migration of water in DNAPL saturated fractures in a laboratory setting. Observing this process can be accomplished using CT scanning or light transmittance through a transparent fracture or thin-slab porous media (Tidwell and Glass, 1994; Weerakone *et al.*, 2011). High-level equipment (e.g. CT scanner) is very expensive limiting general use in a laboratory setting. Epoxy casts of real fractures are required for light transmission methods but have different surface properties and roughness which affects the magnitude of the forces influencing the two-phase flow system. Therefore, computer simulations have taken on a more dominant role in investigating two-phase flow in fractured media. Both local and global modeling approaches have been employed in previous two-phase flow investigations. A global approach utilizing numerical solutions to the differential equations governing two-phase flow has been used to model invasion of trichloroethylene in a saturated fractured clay network (Reynolds and Kueper, 2002). While this global approach has the advantage of including a temporal component, the simulations are time consuming and therefore this approach does not lend itself to running thousands of simulations to generate data (Ewing and

Berkowitz, 1998). A local method, invasion percolation (IP), is based on a simple growth algorithm, accounting for the physics of two-phase flow locally as the invasion process progresses (Ewing and Berkowitz, 1998; Yang *et al.*, 2012a). In effect, an IP model computes local entry or terminal pressures for drainage or imbibition scenarios respectively, based on local forces such as capillary pressure (often, gravity and viscous forces are considered negligible) and fluid migration proceeds in the areas of lowest entry or terminal pressure (Glass and Yarrington, 1996; Glass *et al.*, 2004; Petchsingto and Karpyn, 2010; Wilkinson and Willemsen, 1983; Yang *et al.*, 2012a). The IP approach is far more computationally efficient than the global approach, and therefore lends itself to the generation of large sets of simulated data (Ewing and Berkowitz, 1998).

Several modifications have been applied to the IP approach to enable the inclusion of various physical processes. Previous studies have incorporated capillary fingering of DNAPL (Wilkinson and Willemsen, 1983) and fragmentation of invading DNAPL (Glass and Yarrington, 2003) into the IP approach. Further work has sought to improve capillary pressure computations by including local in-plane curvature and local fracture geometry (Glass and Yarrington, 1996; Glass *et al.*, 1998; Petchsingto and Karpyn, 2010). While capillary pressure is usually considered dominant in the drainage process, gravitational forces have been included in vertical fracture simulations by simply adding a constant gravitational component (Glass and Yarrington, 2003; Yang *et al.*, 2013b). A recent study, however, has demonstrated that gravity should not be neglected when simulating DNAPL migration in macroscopically horizontal fractures with variable apertures (Chapter 2). The inclusion of gravity in this scenario, however, requires a detailed map of the fracture geometry. As macroscopically horizontal or vertical fractures rarely exist in nature, it is also important to investigate the effects of the macroscopic orientation of a fracture on DNAPL migration and entrapment.

Recent work by Yang *et al.* (2012a) used a continuum approach to investigate imbibition in an initially DNAPL-saturated vertical fracture, and found that certain aperture field statistics influenced the volume of trapped DNAPL. More specifically, high aperture field standard deviations and low aperture field correlation lengths allows for potential flow paths for water migration to exist resulting in larger volumes of trapped DNAPL. It is important to note that trapped DNAPL is not sensitive to aperture field standard deviation. However, this work did not investigate the effects of mid-aperture plane statistics, nor did it investigate the effect of fractures oriented in a non-vertical but inclined or declined fashion (Yang *et al.*, 2012a). Work by Weerakone *et al.* (2011) monitored of the injection of DNAPL and brine (the fluids are immiscible; however, they were injected simultaneously into the fracture end cap) in a brine saturated fracture; however, the attempts to model the behavior of the DNAPL migration were unsuccessful. The reason for the discrepancy between simulations and experiments was that the undulous nature of the fracture was not accounted for in the model (Weerakone *et al.*, 2011). Detwiler *et al.* (2009) investigated imbibition in a DNAPL-saturated fracture using IP with the objective of determining the relationship between trapped DNAPL, interfacial area, mass transfer rate, and the Peclet number (Detwiler *et al.*, 2009). While Detwiler *et al.* (2009) examined features related to DNAPL entrapment, the effects of macroscopic fracture orientation on entrapment were not explored.

This study determines the relationship between aperture field statistics, macroscopic fracture orientation and trapped DNAPL saturation utilizing an IP approach to simulate imbibition in a suite of single, DNAPL-saturated fractures. The aperture field statistics considered in this work include aperture field mean (μ_b), SD_b, and mid-aperture field standard deviation (SD_z). Macroscopic fracture orientations range from -60° to 60° from horizontal. The first part of this paper presents the simulation schemes used in this study and provides a discussion of the statistical methods employed in this work. The second part of this paper discusses results regarding trapped DNAPL with respect to aperture field statistics and macroscopic fracture orientation. Finally, equations estimating the range of the trapped DNAPL saturation are developed based on aperture field statistics and the physical properties of the DNAPL.

3.2 Methods

This study utilizes an IP model that incorporates gravity (Chapter 2) in order to examine the effects of aperture field statistics, including the μ_b, SD_b, SD_z, and macroscopic fracture angle, on the saturation of trapped DNAPL following imbibition in a DNAPL-saturated fracture. In rough fractures, the mid-aperture field does not lie on a plane; however, the points can be defined to lie about a plane such that the overall macroscopic profile is a plane. For the purposes of this study, 2 304 fractures were randomly generated and each fracture was rotated through several macroscopic orientations. Cluster computing was employed to conduct IP experiments simulating imbibition in single DNAPL-saturated fractures. The resulting volume of trapped DNAPL was computed and reported as a saturation of the entire fracture volume.

Fracture Generation

A total of 2304 fractures, with specified (list stats here see Table 3.1) were generated stochastically with Matlab code based on SPRT2D (Gutjahr, 1989; James and Chrysikopoulos, 2000; Zheng *et al.*, 2009b,a). The fractures were created by combining two generated fields; one representing the aperture field and another representing the mid-aperture plane. Both the aperture fields and mid-aperture planes were normally distributed. The fractures were 13.8 cm by 22.8 cm (Figure 3.1) generated with a resolution of 2 mm × 2 mm; previous studies have demonstrated that these dimensions result in an accurate representation of the final state of invasion while maintaining reasonable simulation run times (Yang *et al.*, 2012a). For each point on the generated fracture, (x, y, z), the macroscopically horizontal fracture plane was rotated about the y-axis (Figure 3.1) along the fracture inlet to inclined (30°, 60°) and declined (-30°, -60°) using a three-dimensional rotation matrix:

$$\begin{bmatrix} x' \\ y' \\ z' \end{bmatrix} = \begin{bmatrix} \cos\varphi & 0 & \sin\varphi \\ 0 & 1 & 0 \\ -\sin\varphi & 0 & \cos\varphi \end{bmatrix} \begin{bmatrix} x \\ y \\ z \end{bmatrix} \tag{3.1}$$

where φ represents the rotation angle of the fracture and $[x, y, z]^T$ is the coordinate of the rotated fracture. The simulated fractures were used to investigate the relationship between aperture field variability, fracture orientation, and trapped DNAPL saturation following a high-gradient water flush.

Description of Invasion Percolation Model

An IP model (e.g. Glass and Yarrington, 2003; Petchsingto and Karpyn, 2010; Wilson *et al.*, 2009; Yang *et al.*, 2012a,b, 2013b) was used to simulate imbibition in DNAPL-saturated fractures (Detwiler *et al.*, 2009). The fractures had three distinct boundary conditions: 1) an inlet - the only entrance to the fracture at which a constant pressure induced imbibition in the fracture; 2) an outlet - the only exit from the fracture; and 3) sealed sides representing no flow conditions. These conditions are all consistent with a previous study in which the current IP model was calibrated with experimental data (Chapter 2). In the context of field-scale fractures, where pressure across the fracture may not be exceed the terminal pressure, the maximum values for trapped DNAPL may be larger than those observed in this work.

An invasion model was written in Matlab (Mathworks, Natick, MA, USA) utilizing the IP algorithm to simulate the invasion of water into a single DNAPL saturated fracture. The IP algorithm describes the invasion process of one immiscible fluid by another immiscible fluid in porous media or a fracture. IP algorithms assume that primary viscous effects are small relative to capillarity and gravity, which is valid in slow invasion processes. In this study, DNAPL diffusion into the rock matrix is neglected as the focus is on shorter time scale events such as waterflooding post a DNAPL invasion event. Furthermore, as laboratory fractures are being modelled, it is assumed that there is sufficient head for the invading fluid to migrate across the entire fracture. The process is simulated by first discretizing the medium to allow for the computation of physical properties in each element. During model initialization, the invading-defending fluid boundary is selected and an invasion pressure is calculated for each element adjacent to the boundary. The defending fluid is checked for trapped pockets where any element not connected to a defending fluid boundary is removed from the list of potential invasion elements as the fluid must be able to escape in order to be invaded. The N elements with the lowest invasion pressures are then considered invaded and the defending fluid is displaced. The IP algorithm is iterative repeating with a new invasion boundary at each step. The process ends when the invading fluid reaches the opposite end of the fracture. The simulations performed in this study utilized N=4 as this value was shown to be most appropriate in two-phase flow simulations in fractures in a previous study (Chapter 2). The purpose of N is to account for secondary viscous effects, as it decreases the randomness caused by capillary forces at the invasion front (Glass *et al.*, 2001).

Invasion pressures due to capillary and gravity forces are computed via:

$$P_I = \frac{\alpha\sigma\cos(\theta)}{b} + \Delta\rho g\Delta z \tag{3.2}$$

where σ is the interfacial tension, θ is the contact angle between the invading (water) and defending (DNAPL) fluids with respect to the fracture wall, b is the aperture, α is a scaling parameter, $\Delta\rho = \rho_{inv} - \rho_{def}$ is the difference in density between the invading and defending fluids, g is the acceleration due to gravity and Δz is the elevation difference between the invading and defending elements (Corey, 1986; Glass *et al.*, 2001). The first term in equation 3.2 computes the capillary pressure of the element, while the second term computes the pressure difference caused by gravitational forces. The capillary pressure term is a simplification of the Young-Laplace equation where the parameter, α, is dependent on the local geometry of the fracture. In an infinite parallel plate fracture geometry, $\alpha = 2$ (Glass and Yarrington, 1996; Glass *et al.*, 2004; Kueper and McWhorter, 1991), whereas $\alpha = 4$ in a tubular pore configuration

(Glass and Yarrington, 1996; Kueper and McWhorter, 1991). It is expected that in a variable aperture fracture where the geometry is somewhere between a tubular pore and a parallel plate, the value of α will lie between two and four (Kueper and McWhorter, 1991). In this work, the parameter, α, scales capillary pressure to the pressure caused by gravity (equation 3.2). The parameter, α, is representative of the local geometry of the fracture; however, in the context of this study, is used as a globally averaged parameter for the fracture. As experimental results are required to fit the value of α, and all fractures in this study are simulated, values of 2.5, 3, and 3.5 were used to cover a large part of the range over which it can vary (between 2 and 4) (Kueper and McWhorter, 1991). Furthermore, the contact angle is typically measured as a value between 0° (perfectly wetting) and 90° (neutral) with respect to the wetting fluid. In this work the value of θ is measured with respect to the non-wetting DNAPL ($\theta \in [90^\circ, 180^\circ]$). This produces a negative value for the capillary term in equation 3.2. As the IP algorithm selects the elements with the lowest terminal pressures to invade, the elements with the smallest apertures will be selected for invasion which is consistent with the imbibition process (Kueper and McWhorter, 1991).

In the case of imbibition, the gravity term will have a $\Delta\rho < 0$ since the DNAPL is denser than water. If the elevation of the potential invasion element is higher elevation than that of the invading element, then $\Delta z > 0$, the result is a more negative terminal pressure, P_I, thereby increasing the likelihood that water will invade this element. If the elevation of the potential invasion element is lower than that of the invading element, then $\Delta z < 0$, and the gravity term is positive making invasion of this element less likely. The IP model for imbibition thus describes the physical tendency that DNAPL will tend to the lower elevations and the water will tend towards the higher elevations when considering the effect of gravity.

IP Simulation Setup and Parameters

To examine the effects of water flushing a (macroscopically) non-horizontal DNAPL saturated fracture, several thousand imbibition simulations were conducted on non-horizontal fractures and the trapped DNAPL saturation was recorded. The DNAPL employed in these experiments was tetrachloroethene, and the fracture matrix was dolomite (Table 3.2).

Results of the initial set of simulations showed that while horizontal fractures always retain DNAPL, there is little to no DNAPL retention in a subset of the declined fractures. To investigate this effect further, 100 fractures in which simulations produced the lowest trapped DNAPL saturation, for each value of the SD_z, were selected from the horizontal case ($\varphi = 0°$) and the fractures and α values used in those simulations were then used in further simulations with angles -2.5°, -5°, -7.5°, -10°, and -15° to elucidate upon the trend allowing for no retention of DNAPL to some retention of DNAPL, the differences observed between the trapped DNAPL saturation graphs in the declined angles from the horizontal angle.

In order to develop equations to estimate the trapped DNAPL saturation in an initially DNAPL-saturated fracture after imbibition, additional simulations were conducted using the physical properties from each of the DNAPL/fracture interface scenarios listed in Table 3.2. These simulations employed combinations found in natural formations: PCE-dolomite, PCE-silica, carbon tetrachloride-clay, chlorobenzene-clay and chloroform-clay (Cohen *et al.*, 1993) as well as one from a laboratory experiment that examined HFE 7100-epoxy (Chapter 2). More specifically, imbibition in a

DNAPL-saturated fracture was simulated for 768 fractures sampling all combinations of the fracture statistics listed in Table 3.1, with four replicates per set of statistics, and two values of α (2.5, 3.5). Together, these scenarios resulted in 18432 additional simulations. All simulations were conducted using SharcNET cluster computing.

Statistical methods used in analysis of trapped DNAPL

The trapped DNAPL saturation was calculated for each fracture using the following equation:

$$DNAPL_{saturation} = \frac{(2mm)\,(2mm)}{V_F}\sum_i b_i\delta_i \tag{3.3}$$

where the area of the potentially invaded element is represented by 2 mm $\times$ 2 mm, b_i is the aperture of the ith element δ_i is defined as 0 if the ith element contains water or 1 if the ith element contains DNAPL summed over all elements of the fracture and V_F is the total volume of the fracture.

The percent difference of entrapped DNAPL between simulations conducted in an unique fracture geometry subject to different orientations was calculated as follows:

$$PD = \frac{F\left(\varphi_{ref}\right) - F\left(\varphi\right)}{F\left(\varphi_{ref}\right)} \tag{3.4}$$

where F is the DNAPL saturation in the fracture of interest, and φ_{ref} is the macroscopic orientation of the fracture in degrees used as the reference angle and φ is the macroscopic orientation used as a comparison to the reference. In this study, the reference orientation is horizontal ($\varphi_{ref} = 0°$).

The coefficient of variation (COV) is a dimensionless measure of aperture roughness and is calculated using the following equation for each fracture:

$$COV = \frac{SD_b}{\mu_b} \tag{3.5}$$

where SD_b is the aperture standard deviation and μ_b is the mean aperture. Larger COVs indicate more local variation within an aperture field.

The results of the simulations were used to develop empirical equations estimating ranges entrapped DNAPL based on fracture and DNAPL characteristics. A selection of statistics that are typically measured or estimated relating to the DNAPL and fracture-DNAPL-water interface (interfacial tension, σ; contact angle, θ; and the difference in density between DNAPL and water, $\Delta\rho$) as well as aperture field statistics (μ_b; SD_b; SD_z) were projected into a single variable, R_φ, in order to relate these quantities to the trapped DNAPL saturation. Figures 3.2-3.4 demonstrate that fracture at orientations of $\varphi \geq 0°$ and $\varphi \leq -15°$, respectively, behave in a similar fashion regarding the trapped DNAPL saturation. For the purposes of generating equations estimating the level of trapped DNAPL saturation, fracture angles only φ=0° and φ=-15° orientations are considered. Furthermore, each statistical variable in R_φ was exponentiated to a value ni to enable modification of the relationship of the variables included in R_φ. Thus, R_φ is given in the following equation:

$$R_\varphi = \sigma^{n_1} \cos^{n_2} \theta \Delta\rho^{n_3} \mu_b^{n_4} SD_b^{n_5} SD_z^{n_6} \tag{3.6}$$

Generation of the empirical equations estimating the range of the trapped DNAPL saturation requires plotting the saturation (equation 3.3) against the natural logarithm of R_φ. As such, for a given fracture angle, φ, the values of n_i must be such that across all values of R_φ, the range of possible trapped DNAPL saturation values is as small as possible. A genetic algorithm was utilized that varied each n_i value in integers from -5 to 5 in order to minimize the trapped DNAPL saturation range. For a given set of n_i values, a plot of trapped DNAPL saturation (y-axis) versus $\ln(R_\varphi)$ (x-axis) was created. A fitness function was constructed by fitting the upper and lower most DNAPL saturation values with a 3rd order polynomial, then calculating the area between the curves and normalizing this value with the total area of the graph. This fitness function was minimized in the genetic algorithm.

Once optimization was reached for both fracture orientations (φ=0° and φ=-15°), the logistic equation:

$$S = \frac{c_1}{1 + c_2 e^{-c_3 \ln(R_\varphi)}} \tag{3.7}$$

was used to fit the upper most trapped DNAPL saturation values for the results of both fracture orientations and the lower most trapped DNAPL saturation values of the φ=-15° orientation. The constants c_1, c_2 and c_3 were modified as fitting parameters in the regression. For the lower most trapped DNAPL saturation values in the φ=0° orientation, an exponential equation was used to fit the data via varying the constants c_1, c_2 and c_3 as fitting parameters in the regression:

$$S = c_1 + c_2 e^{c_3 \ln(R_\varphi)} \tag{3.8}$$

The resulting fitted equations (equations 3.113.14) estimate the minimum and maximum trapped DNAPL saturation based on the fracture orientation, physical properties of the DNAPL, fracture matrix properties, and aperture field statistics. It is important to note that retained DNAPL in an inclined fracture may be estimated using the functions derived for the horizontal fracture while fractures oriented such that $\varphi < -15°$ may be estimated using the functions derived for the fracture oriented at $\varphi = -15°$.

3.3 Results and Discussion

Effect of COV and SD_z on DNAPL entrapment

Fracture COV heavily influences the amount of entrapped DNAPL in fractures following a water flush (Figure 3.2). An increase in the trapped DNAPL saturation level is observed with increasing fracture COV; a high COV reduces the number of potential flow paths for water due to high local variation, thus hindering the displacement of DNAPL by water as the water invades along the few available flow paths (Figures 3.2-3.3). The result of a preferential flow path for water is a larger trapped DNAPL saturation. Figures 3.2A and B show that, in declined fractures, it is possible for little to no DNAPL to be retained. Specifically, in the declined fractures, when the COV is less than 0.1, the trapped DNAPL saturation is much lower than in fractures characterized by COV values greater than 0.1 (Figure 3.2A-B). This effect occurs because the gravitational forces together with the planar characteristics of the fracture enable DNAPL to exit the fracture with little resistance. Figures 3.2A-E show that when the COV is greater than 0.1, the orientation of the fracture (declined, horizontal or inclined) does not greatly influence the trapped DNAPL saturation in the fracture. The

DNAPL retained is a minimum of 30% of the fracture volume, and has an increasing trend with increasing COV. Figures 3.2C-E show that for fractures with horizontal and inclined orientations and COVs less than 0.1, the DNAPL saturation does not vary with COV. In summary, these data show that for fractures with COV<0.1, declined orientations enable the possibility of little or no retained DNAPL; however, for horizontal or inclined orientations there is always some DNAPL saturation. When COV>0.1 there is always some DNAPL retained regardless of fracture orientation.

Figure 3.3 shows the trapped DNAPL saturation as a function of SD_z, which is an alternate measure of fracture roughness, and shows that the upper bound of entrapped DNAPL is relatively unaffected by SD_z for all fracture orientations; the maximum DNAPL saturation in all scenarios employed in this work is approximately 80% (Figure 3.3). Little to no DNAPL is retained in declined fractures with COVs less than 0.1 (Figure 3.3A-B); however, lower bound of entrapped DNAPL decreases as SD_z increases in horizontal and inclined fractures (Figure 3.3C-E). For example, the minimum trapped DNAPL saturation in horizontal fractures with similar COVs with a SD_z of 0.01 mm is 48%, whereas it was 30% in horizontal fractures with a SD_z of 10 mm (Figure 3.3C). This effect is counter intuitive as it is expected that increasing the variability in the mid-aperture plane (SDz) should increase the likelihood of DNAPL trapping and is discussed further in the next paragraph. A similar trend is observed for both sets inclined simulations (Figure 3.3D-E). Figure 3.3 also shows that the COV has a larger effect on the trapped DNAPL saturation, as the largest trapped DNAPL saturation occurs in fractures with the highest COV regardless of the SDz, and fracture orientation, and the lowest trapped DNAPL saturation occurs in fractures with the lowest COVs regardless of SD_z and fracture orientation.

The decrease in the minimum bound of trapped DNAPL with increasing SD_z in horizontal and inclined fractures can be explained by considering the invasion computation. The elevation difference used in the calculation of pressure caused by gravity (equation 3.2) is the difference in elevation between two adjacent elements in the mid-aperture field. Therefore, the magnitude of local gravitational forces aiding or opposing invasion are dependent on the variability of the mid-aperture field. An uphill portion of a fracture will cause a component of the gravitational force to oppose imbibition (but is generally dominated by capillarity). However, a downhill section of a fracture will cause a component of the gravitational forces to aid imbibition thereby trapping less DNAPL. As SD_z increases, the potential for more downhill sections of the fracture increases, thus smaller values of trapped DNAPL saturation are observed.

Fracture Angles Permitting Little or No Retained DNAPL

It is apparent that only declined fractures enable little to no trapping of DNAPL (Figures 3.2-3.3); however, to determine the orientation at which this occurs, additional simulations were performed at orientations between φ = -30° and φ = 0°. The fractures from 100 simulations retaining the minimum DNAPL saturation were selected from the horizontal case and these fractures were used in simulations with orientations ranging from φ = -15° to φ = 0°. The resulting trapped DNAPL saturations show that little to no trapped DNAPL occurred at φ = -15°, with a few simulations with orientations of φ = -10° and φ = -7.5° also trapping no DNAPL (Figure 3.4). As these fractures were selected because their aperture field statistics minimize the amount of trapped DNAPL, they demonstrate the extreme case where there is little to no trapping of DNAPL for φ = -15° or less; however, if fractures with higher COV >

0.1 (Figure 3.2) or $SD_z > 1$mm (Figures 3.2-3.3) were used, these simulations would result in the trapping of DNAPL. In summary, trapped DNAPL saturation increases with both fracture angle and COV; whereas increasing SD_z enables the possibility of trapping less DNAPL in horizontal and inclined fractures.

Preferential Flow Paths

Fractures with COV>0.1 have been shown to trap DNAPL post flushing. This high variance in the aperture field contributes to flow channeling, and therefore the final invasion path of water into the DNAPL saturated fracture was examined for several sets of parameters for a range of fracture orientations (φ = -60° to φ = 60°). Imbibition occurs through smaller aperture regions with less local variation. Increasing fracture COV implies greater variation within the fracture and is therefore more likely to produce a preferential flow pattern of water thereby resulting in more trapped DNAPL. To illustrate this point, an example of a preferential flow path that is retained despite changes in fracture angle is shown in Figure 3.5. This fracture has a COV of 0.57, which should result in trapped DNAPL following imbibition (COV > 0.1). A flow pathway develops through the smaller aperture regions (Figure 3.5A, blue colored pixels), while there is no obvious relationship between the flow pathway and the mid-aperture field (Figure 3.5B). For a given fracture geometry, the preferential flow path was similar regardless of orientation (Figure 3.5), indicating that flow pathway is not necessarily dependent upon the fracture orientation. The flow path is, however, closely tied to the aperture field statistics, and specifically the small aperture regions, and therefore distinct flow pathways are more likely to develop at higher COVs.

In fractures with COVs less than 0.1, the water flow pattern is less likely to be restricted to a tight preferential flow path (e.g. Figure 3.5), allowing for fractures at declined angles to retain less DNAPL in the fracture. A fracture with no retained DNAPL at φ = -60° (COV = 0.01, SD_z = 1mm) was selected as an illustrative example (Figure 3.6). This fracture shows no obvious preferential flow path (Figure 3.6A); however, higher elevations in the mid-aperture field are more likely to permit water during the invasion process as DNAPL is denser, and therefore tends towards the lower elevations. DNAPL is observed to be retained in the lower elevations of the mid-aperture field (Figure 3.6B) at fracture angles greater than -5° (Figure 3.6E-G) with the retained DNAPL pools becoming larger with increasing fracture angle. At low declined fracture angles (φ = -30°, (Figure 3.6C); φ = -20° (Figure 3.6D)) nearly all of the DNAPL has been removed from the fracture; however, as the fracture angle increases to φ = -10° or φ = -5° more DNAPL is retained (Figure 3.6E-F) as expected based in the results from Figures 3.2-3.4.

Differences between trapped DNAPL saturation in inclined and declined orientations

The percent difference of trapped DNAPL saturation (equation 3.4, with the horizontal fracture used as reference) between the declined orientation ($\varphi < 0°$) and the horizontal orientation ($\varphi = 0°$) was computed for simulations in each fracture. As well, the percentage difference in trapped DNAPL saturation between the inclined orientation ($\varphi > 0°$) and the horizontal orientation ($\varphi = 0°$) was computed for simulations in each fracture. The results of this analysis show that there are greater percentage differences of retained DNAPL observed between declined fractures ($\varphi < 0°$) and the horizontal reference fractures than observed between inclined and horizontal simulations. Comparisons of simulations in declined orientations with the same fracture in a horizontal orientation had a mean percentage difference of 51.4% ($\varphi = -60°$) (Figure 3.7A) and 36.2% ($\varphi = -30°$) (Figure 3.7B); simulations in the same inclined fracture compared to fractures oriented horizontally had a mean percentage difference of 7.8% ($\varphi = 30°$) (Figure 3.7C) and 10.1% ($\varphi = 60°$) (Figure 3.7D). These data suggest that a given fracture will retain similar DNAPL saturation levels in orientations ranging from horizontal to inclined orientations (up to 60°). Declined orientations significantly reduce the trapped DNAPL saturation when compared to simulations in the same fracture oriented horizontally.

Estimating the trapped DNAPL saturation

This study has shown that DNAPL retention in declined fractures differs from horizontal and inclined fractures in that horizontal and inclined fractures always retain DNAPL, whereas declined fractures permit cases where little to no DNAPL is retained (Figures 3.2-3.3). More specifically, it was observed that fractures oriented at $\varphi \leq$ -15° tend to behave similarly in terms of DNAPL retention permitting cases where there is little to no DNAPL retention; whereas, fractures oriented at $\varphi \geq 0°$ behave similarly. Simulated data enabled the generation of empirical equations to estimate the trapped DNAPL saturation in a fracture given various parameters: $\Delta\rho$, θ, σ, μ_b, SD_b, SD_z, and φ. DNAPL density, θ, and σ define various possible fracture-DNAPL-water relationships, and μ_b, SD_b, and SD_z incorporate aperture field statistics into the empirical equations. Simulations were conducted using 1 536 of the generated fractures selected to cover the full range of aperture field statistics (Table 3.1). The simulations utilized the various fracture-DNAPL-water interface data given in Table 3.2, which were chosen based on previously published data (Cohen *et al.*, 1993). The trapped DNAPL saturation is heavily dependent on φ for fractures oriented between $-15° < \varphi < 0°$, and thus it was not possible to attain appropriate minimum and maximum functions in this range. For fractures oriented between -15° and 0°, the minimum trapped DNAPL saturation may be estimated by computing the minimum trapped DNAPL saturation for both of the φ = -15° and φ = 0° cases for a given set of fracture and DNAPL characteristics and simply using the minimum of the two values. A similar method can be used to compute the maximum trapped DNAPL saturation in fractures oriented between -15° and 0°.

For the two fracture angles investigated, a total of 9216 simulations were conducted varying the six aforementioned parameters based on realistic fracture-DNAPL-water relationships and aperture field statistics. The trapped DNAPL saturation in each simulation was computed and added to the data set. In order to simplify the estimation of the trapped DNAPL saturation based on fracture and DNAPL characteristics, a composite ratio for each fracture angle ($R_{\varphi=-15°}$ and $R_{\varphi=0°}$) was defined (equation 3.6). Utilizing a genetic algorithm, the tightest and most increasing trend was determined by plotting the trapped DNAPL saturation versus the natural logarithm of R_φ and varying the values of n_i, for i from 1 to 6 (equation 3.6). The resultant optimized R value for fractures angled $\varphi \leq$ -15° is:

$$R_\varphi = \sigma^1 \cos^2\theta \Delta\rho^{-2} \mu_b^{-2} SD_b^2 SD_z^1 \tag{3.9}$$

The resultant optimized R_φ equation for fractures angled $\varphi \geq 0°$ is:

$$R_{\varphi} = \sigma^{1} \cos\theta \Delta\rho^{-1} \mu_b^{-1} SD_b^{-2} SD_z^{-2} \tag{3.10}$$

After determining the values for R_{φ}, it was possible to fit a logistic equation (equation 3.7) to the upper bound of each data set ($\varphi \leq -15°$ and $\varphi \geq 0°$) and to the lower bound of the $\varphi \leq -15°$ data set (Figure 3.8). Given the shape of the $\varphi \geq 0°$ data set, an exponential function was chosen to represent the lower bound (Figure 3.8A). The resultant minimum and maximum trapped DNAPL saturation in a fracture with angle $\varphi \leq -15°$ may be estimated using the simplified equations:

$$FR_{min,\varphi \leq -15°} = \frac{0.388}{1 + 0.280 \frac{cm^{6.027}}{s^{1.722} g^{0.861}} R_{\varphi=-15°}^{-0.861}} \tag{3.11}$$

$$FR_{max,\varphi \leq -15°} = \frac{0.800}{1 + 1.701 \times 10^{-8} \frac{cm^{11.739}}{s^{3.354} g^{1.677}} R_{\varphi=-15°}^{-1.677}} \tag{3.12}$$

The resultant minimum and maximum trapped DNAPL saturation in a fracture with angle $\varphi \geq 0°$ (Figure 3.8B) may be estimated using the simplified equations:

$$FR_{min,\varphi \geq 0°} = 0.345 + 0.0019 s^{0.282} cm^{0.282} R_{\varphi=0°}^{0.141} \tag{3.13}$$

$$FR_{max,\varphi \geq 0°} = \frac{0.870}{1 + 2.941 \frac{1}{s^{0.412} g^{0.412}} R_{\varphi=0°}^{-0.206}} \tag{3.14}$$

3.4 Conclusions

The results of this study demonstrate that declined fractures permit the possibility of little to no trapped DNAPL after waterflooding whereas horizontal and inclined fractures always trap DNAPL at a saturation level of at least 25%. Fractures that retain DNAPL at any orientation with COV > 0.1 demonstrate a preferential flow path of water through the fracture. In these cases, the aperture field dominates the invasion path with water flowing along the smallest of the aperture values with the mid-aperture field playing little role during the invasion process throughout any fracture angle. For fractures that demonstrate little to no DNAPL retention at declined orientations, occurring only COV < 0.1, the mid-aperture field greatly affects the overall entrapment pattern. In these cases, DNAPL tends to lower elevations and water tends to higher elevations in the horizontal and inclined orientations and DNAPL trapped at inclined orientations is greatly eroded in the declined orientations.

Equations estimating the lower and upper bounds of the trapped DNAPL saturation were developed for fractures of varying geometries (measured by μ_b, SD_b and the SD_z) as well as varying contact angle, interfacial tension and DNAPL density. These equations were developed for fracture orientations of $\varphi = -15°$ and $\varphi = 0°$ to account for orientations less than $-15°$ and greater than $0°$, respectively. Fracture orientation coupled with the fracture statistics of COV and SD_z have proven valuable in determining the trapped DNAPL saturated in waterflooded fractures.

Chapter Contents

The contents of this chapter are in preparation for submission. The authors are Sean P. L. Cianflone, Jason A. Beattie, and Sarah E. Dickson.

Table 3.1: Fracture Generation Parameters

Parameter	**Aperture Field (b)(mm)**	**Mid-aperture Field (z) (mm)**
μ	0.5, 1, 1.5	0
SD	0.01, 0.05, 0.1, 0.3	0.01, 0.1, 1, 10
λ	10	5, 10, 25, 50

Table 3.2: DNAPL Characteristics (HFE 7100 from Chapter 2), rest fromCohen *et al.* (1993))

DNAPL	**Fracture Interface**	**Density (g/cm^3)**	**Wetting Angle (°)**	**Interfacial Tension (dynes/cm)**
HFE 7100	Epoxy	1.520	81	42.4
PCE	Dolomite	1.623	20	44.4
PCE	Silica	1.623	40	44.4
Carbon Tetrachloride	Clay	1.593	27	45.0
Chlorobenzene	Clay	1.105	34	37.4
Chloroform	Clay	1.402	30	32.8

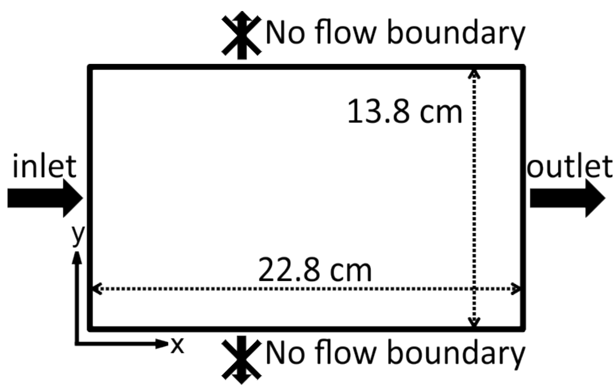

Figure 3.1: Fracture dimensions and simulation boundary conditions used in all simulations. Initially, the fracture was saturated with PCE (DNAPL) and water was used as the invading fluid invading at the inlet.

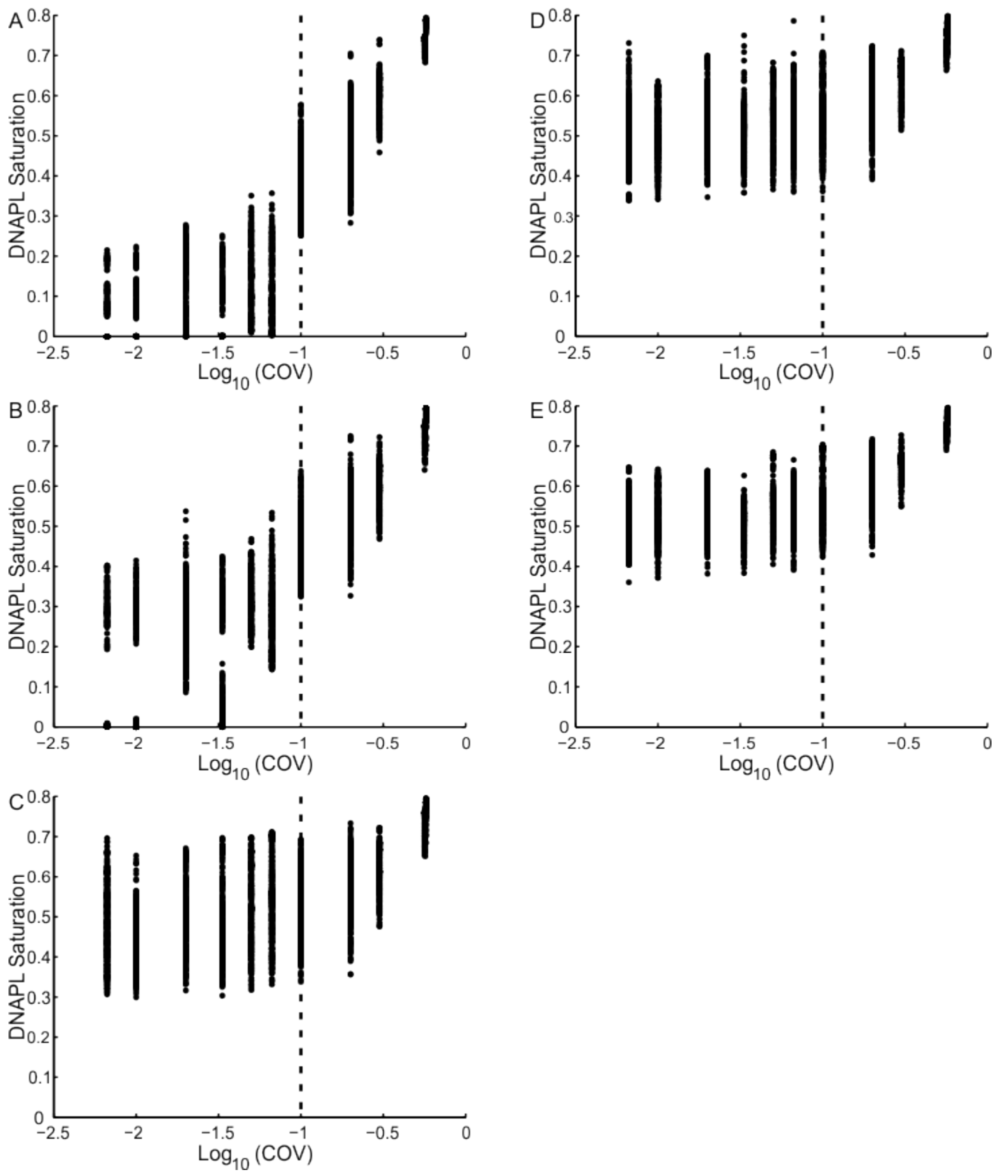

Figure 3.2: Fraction retained DNAPL post flushing plotted against the base ten log of the COV for fracture simulations at varied fracture angle, φ. The dotted line at -1 on the x-axis is the boundary indicating when gravitational effects start being dominated by capillarity. A) sub-horizontal fracture angle of $\varphi = -60°$; B) $\varphi = -30°$; C) horizontal fracture angle $\varphi = 0°$; D) super-horizontal fracture angle $\varphi = 30°$; E) $\varphi = 60°$.

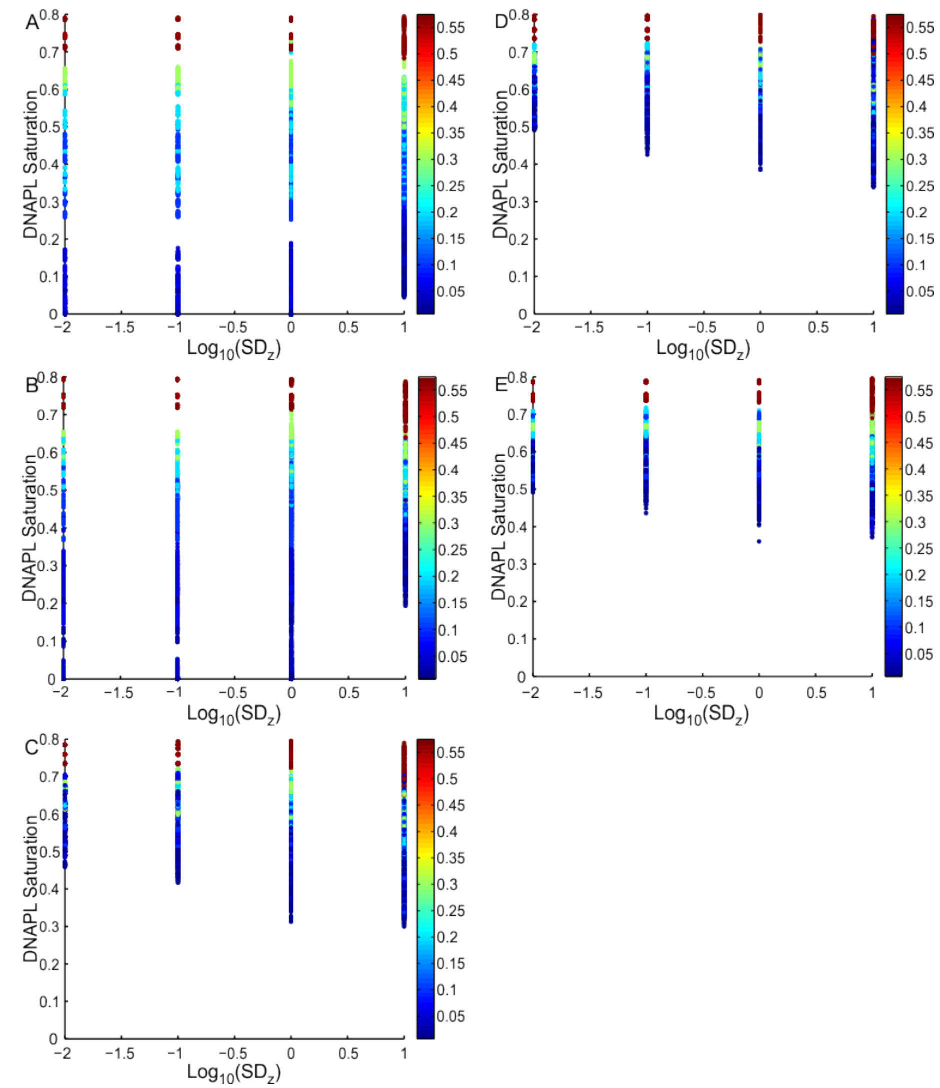

Figure 3.3: Fraction DNAPL by volume for different angle orientations plotted against the base ten log SD_z. The heat map indicates the different values of the fracture COV. A) sub-horizontal fracture angle of $\varphi = -60°$; B) $\varphi = -30°$; C) horizontal fracture angle $\varphi = 0°$; D) super-horizontal fracture angle $\varphi = 30°$; E) $\varphi = 60°$.

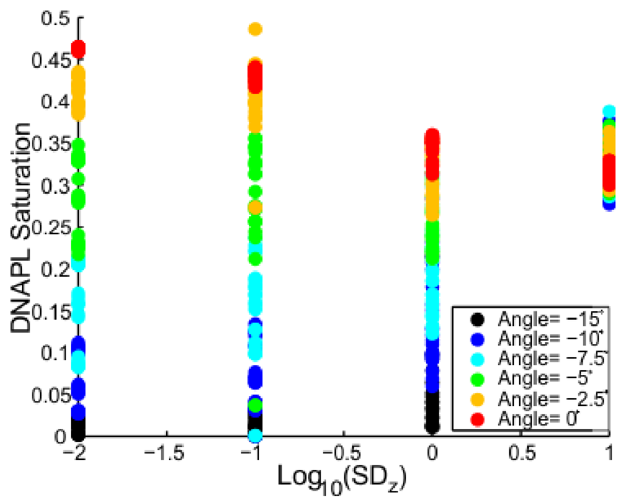

Figure 3.4: A selection of fractures with the lowest DNAPL retention at fracture angle $\varphi = 0°$ for each SD_z value. Simulation of resultant fraction DNAPL by volume for each fracture is plotting against the $\log_{10}(SD_z)$. Intermediate angles between $\varphi = -15°$ and $\varphi = 0°$ are shown in color.

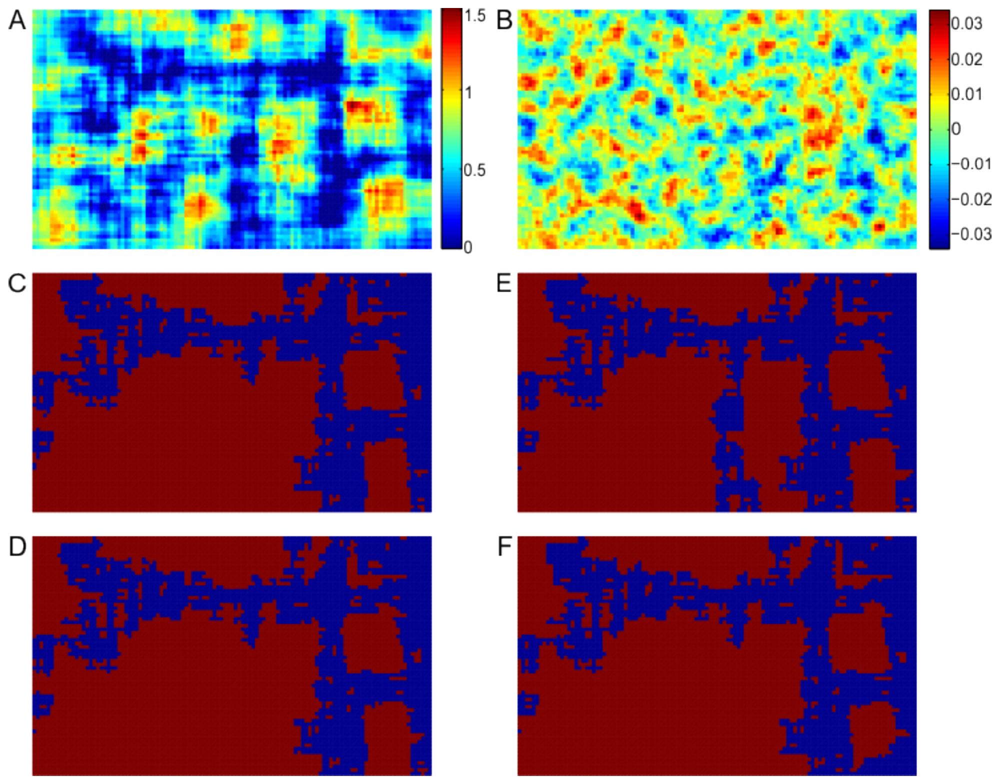

Figure 3.5: A) the aperture field of a randomly generated fracture with high COV (COV = 0.57, μ_b=0.5, SD_b=0.29 mm). The colour bar shows the aperture value in mm. B) the mid-aperture field of the same randomly generated fracture (SD_z = 0.01mm, λ=5). The colour bar shows the mid-aperture field value in mm. C) A schematic view of the preferential flow path of water (blue, invader) in the fracture with a fracture angle of $\varphi = -60°$. DNAPL (defender) is shown in red. D) Fracture angle of $\varphi = -30°$. E) Fracture angle of $\varphi = 0°$. F) Fracture angle of $\varphi = 60°$.

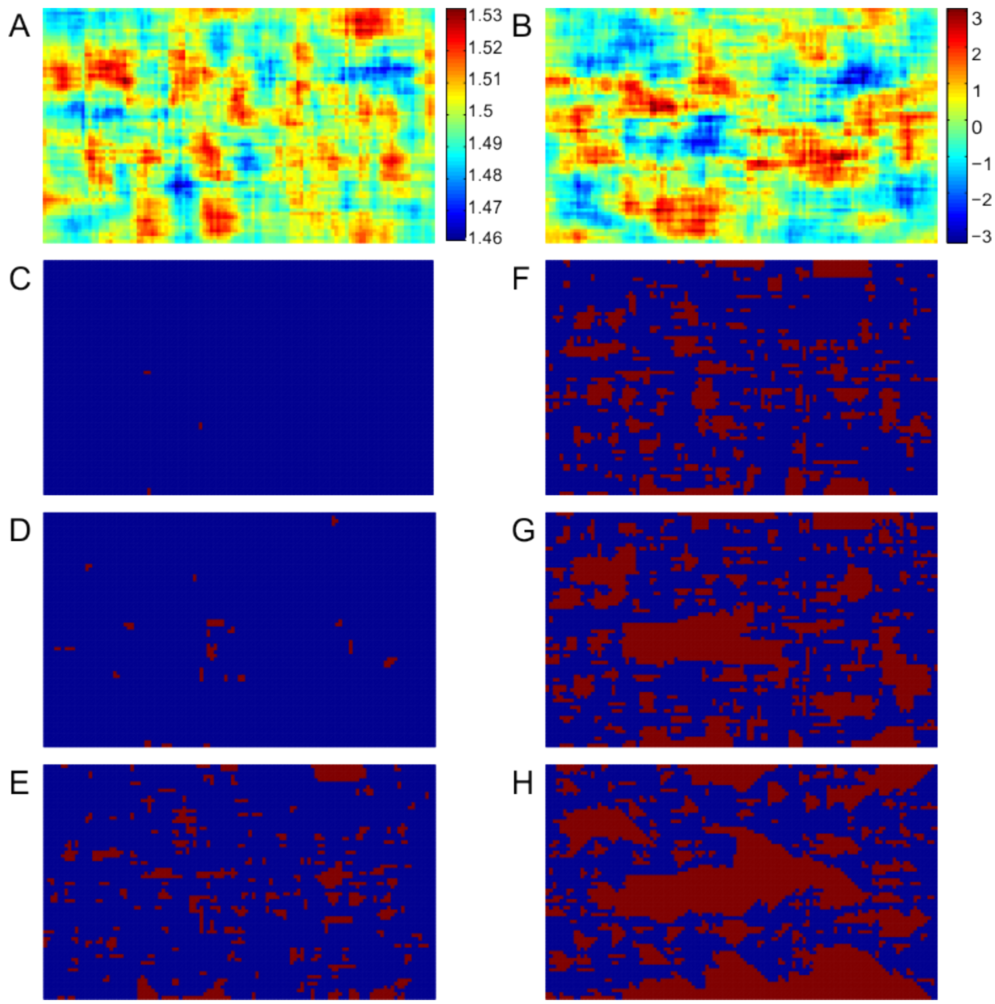

Figure 3.6: A) the aperture field of a randomly generated fracture with low COV (COV = 0.01, μ_b=1.5, SD_b=0.01 mm). The colour bar shows the aperture value in mm. B) the mid-aperture field of the same randomly generated fracture (SD_z = 1mm, λ=26). The colour bar shows the mid-aperture field value in mm. C) A schematic view of the lack of preferential flow path of water (blue, invader) in the fracture with a fracture angle of $\varphi = -30°$. DNAPL (defender) is shown in red. D) Fracture angle of $\varphi = -20°$. E) Fracture angle of $\varphi = -10°$. F) Fracture angle of $\varphi = -5°$. G) Fracture angle of $\varphi = 0°$. H) Fracture angle of $\varphi = 60°$.

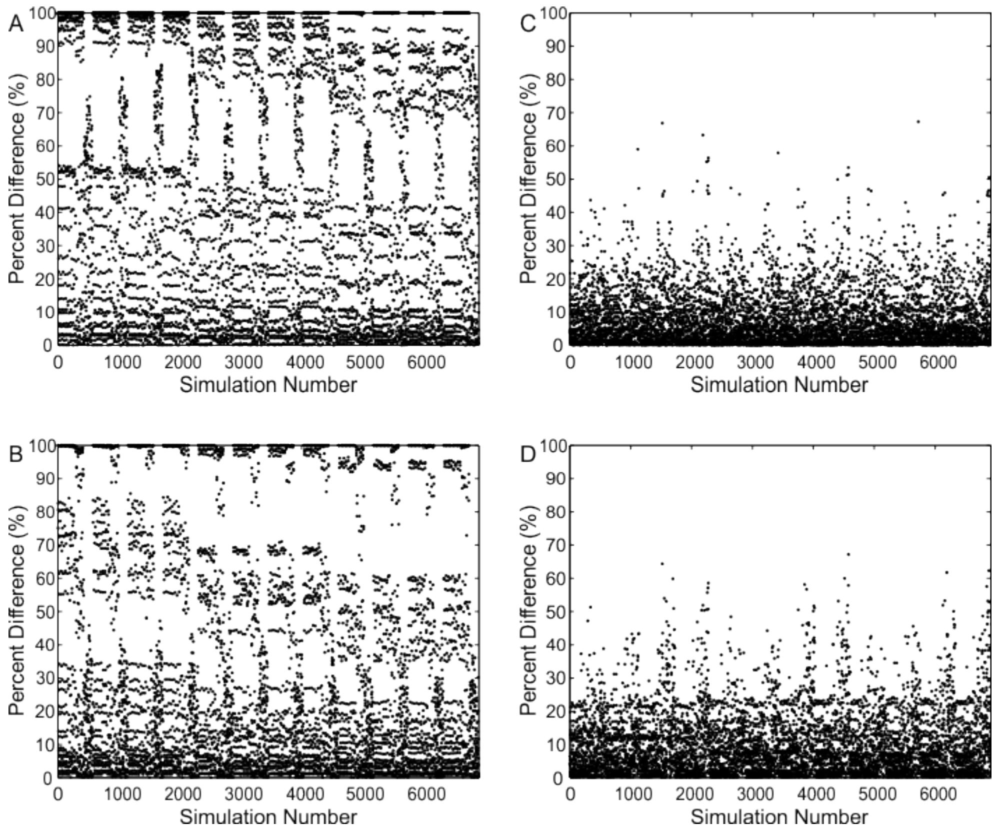

Figure 3.7: Percentage difference (equation 3.4) between simulations (denoted by simulation number) with $\varphi_{ref} = 0°$ and $\varphi_n = -60°$; B) $\varphi_{ref} = 0°$ and $\varphi_{ref} = 0°$ and $\varphi_n = -30°$; C) $\varphi_{ref} = 0°$ and $\varphi_n = 30°$; D) $\varphi_{ref} = 0°$ and $\varphi_n = 60°$.

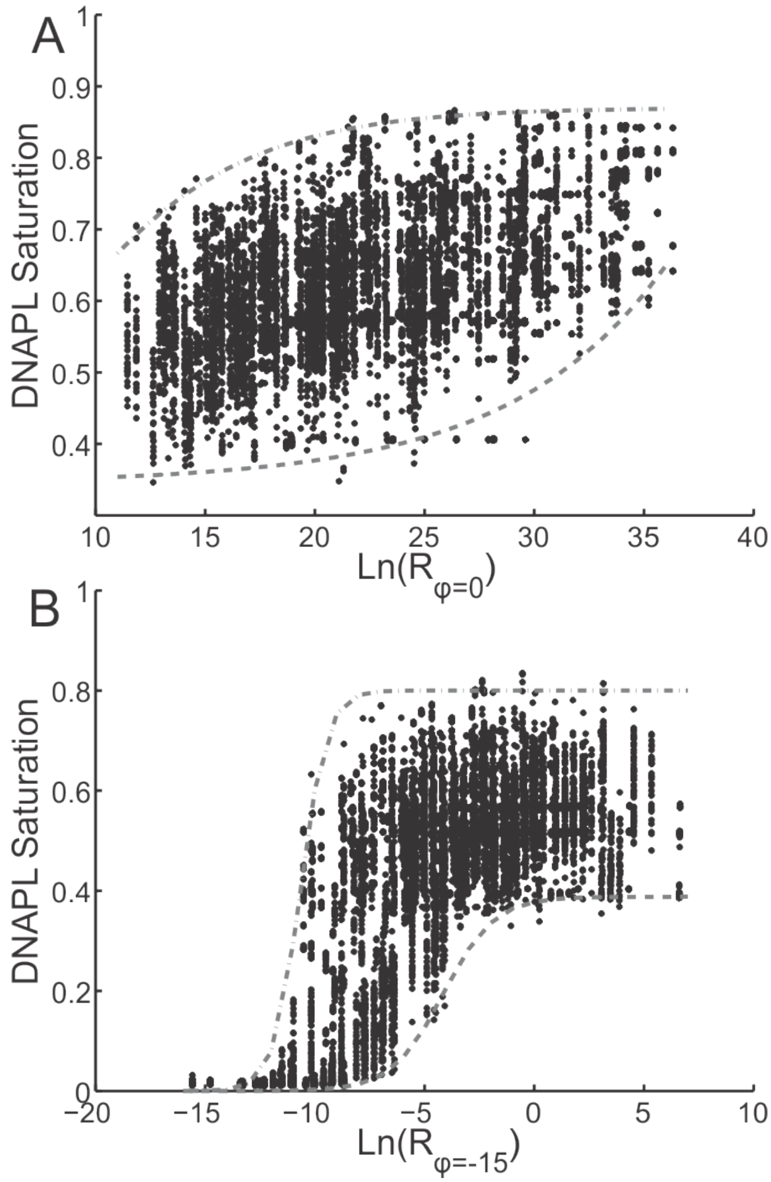

Figure 3.8: A) A plot of the fraction DNAPL retained in horizontal fractures ($\varphi = 0°$) after flushing with water given various fracture characteristics and fracture-DNAPL-water interfaces producing various $R_{\varphi=0°}$ values. The lower ((---); equation 3.13) and upper (-·-; equation 3.14) bounds are shown. B) Fraction DNAPL retained in sub-horizontal fractures ($\varphi = -15°$) after flushing with water given various fracture characteristics and fracture-DNAPL-water interfaces producing various $R_{\varphi=-15°}$ values. The lower ((---); equation 3.11) and upper (-·-; equation 3.12) bounds are shown.

Chapter 4

Effect of Hydrodynamics and Geometry on Particle Transport in Saturated Fractures: Experimental and Simulation Results

Abstract

An experiment to measure the transport of particles (0.046 μm and 0.55 μm microspheres) in randomly generated variable aperture fractures where variation only occurred in the xy-plane, not along the z-axis, were conducted. The fracture geometry was then used to computationally generate a fluid velocity field via the Navier-Stokes equations and optimize a random walk particle tracking (RWPT) algorithm that included hydrodynamic effects on transport, including the velocity field, shear, gravity,

and diffusion. The experiments were used to optimize parameters in the RWPT model and the resulting simulations were analyzed for insight into the effects of hydrodynamics on particle transport. Results show that shear has a small but appreciable effect on the transport of particles causing an increase in dispersion. Shear represents less than 1% of the particle movement when compared to movement caused by fluid migration. Examination of fracture geometry showed that local narrowing of the fracture aperture field causes particles to shift the area of the fracture where transport occurs. More specifically, it was found that some pinch points can force particles into the center of the fracture thus eliminating any chance of collision with fracture walls, thereby 1) reducing the likelihood of retention due to adhesion to the fracture walls; and 2) increasing the mean particle velocity which results in a higher peak concentration of particles exiting the fracture. These effects depend on the local geometry and are not predictable from typical fracture characterization statistics alone (e.g. aperture mean, covariance, and correlation).

4.1 Introduction

Many people in Canada and the United States rely on groundwater for their drinking water supply. As groundwater may not be municipally treated, there is a possibility for contaminants to appear in the drinking water of these residents (Mondal and Sleep, 2013; Rodrigues and Dickson, 2014). Some of the more acute health hazards arise from particulate contaminants, such as viruses (e.g. hepatitis A, norovirus), bacteria (*E. coli*, *Salmonella*), and protozoa (e.g. *Giardia lamblia*, *Cryptosporidium*) for which there have been numerous documented cases of waterborne illness (Schuster *et al.*, 2005). Most research regarding the transport of these particles in groundwater systems has primarily been concerned with porous media. The methods developed for study and prediction of particulate transport in porous media have been applied to fractured aquifers. There are, however, important physical differences between fractured and porous media aquifers that affect the hydrodynamic properties, surface adhesion of particles, and ultimately the transport of particles in these system (Rodrigues and Dickson, 2014). Understanding the particle transport mechanisms involved in these less studied fracture systems will aid in the characterization, management and potential remediation of fractured aquifers.

Previous studies attempting to model particle transport in fractures have focused on both single fractures (Abdel-Salam and Chrysikopoulos, 1995; Chrysikopoulos and James, 2003; James and Chrysikopoulos, 2000; James *et al.*, 2005; Keller *et al.*, 1999; Rodrigues and Dickson, 2014; Zheng *et al.*, 2009b) and fracture networks (Kim *et al.*, 2015; Masciopinto *et al.*, 2008; Robinson *et al.*, 1998; Willmann *et al.*, 2013; Zhang *et al.*, 2015). While fracture networks are often coupled with experimental data, these studies use stochastic or deterministic methods that simplify the variable fracture geometries into parallel plates for computational efficiency, and thus do not seek to attain the relationship between hydrodynamic forces in the flow field and particle transport. While single fracture modelling studies generally compute the flow field and use random walk particle tracking (RWPT) methods or the advection-dispersion equation, they typically do not include physical experimental data for calibration, as the 3D geometries of fractures are difficult to attain; when geometries are attained, it is computationally intensive to solve the explicit Navier-Stokes equations governing flow in 3D fractures without simplifications and coupling a flow field to equations of particulate transport (Berkowitz, 2002).

Efforts to examine the effects of fracture geometry on transport have been limited to 2D fracture studies using the Navier-Stokes equations for flow field generation (Boutt *et al.*, 2006; Cardenas *et al.*, 2007; Koyama *et al.*, 2008b) or 3-D studies that utilize simplified equations of flow (Zheng *et al.*, 2009b,a). Cardenas *et al.* (2007) presented evidence of eddy formation in a 2D section of a real fracture, and showed that solutes became trapped in the eddy. While this study demonstrates the potential for solute trapping, the effect of the eddy on less diffusive particles is not investigated. Koyama *et al.* (2008b) demonstrated that particle concentration profiles (induced by the flow field) in a fracture differ from the expected parabolic shape found in a parallel plates because of the geometry of the fracture. Koyama *et al.* (2008b) used a 2D using particle tracking approach that lacked a diffusive process, thus forcing the particles to follow a single stream line. In reality, particles will move between streamlines during transport via diffusion and other hydrodynamic effects, and therefore the results of Koyama *et al.* (2008b) are difficult to interpret. Boutt *et al.* (2006) established that particles became trapped in small eddy zones along rough fracture walls; however, their use of a 2D fracture with no experimental validation limits greater applicability of their results to field scale problems.

One of the hydrodynamic effects of interest noted by Segre and Silberberg (1962) is that particles transported in a tube tend to migrate away from both the center of the tube and the walls. This effect has been accounted for in channels by increasing the dispersion in models through modifying the diffusion coefficient in the RWPT algorithm with a term that increases the value (Aris, 1956; James and Chrysikopoulos, 2003; Taylor, 1953). A larger diffusion coefficient increases dispersion, but particles are not affected in a directional way as diffusion is a random process. Recent studies in microchannels have shown that the migration away from the center of the channel is proportional to fluid shear (Di Carlo *et al.*, 2009; Marcos *et al.*, 2012; Rusconi *et al.*, 2014). A hydrodynamic wall effect lift force has been shown to force the migration of particles away from walls and it tends towards zero as the particles move away from the wall (Di Carlo *et al.*, 2009; Masaeli *et al.*, 2012). Di Carlo *et al.* (2007) showed that not only does this effect move particles away from both the center line and walls of a microchannel, the microchannel geometry influences the particles migration pathway when compared to the straight microchannel. While these effects appear in microchannels where the particle size is large compared to the channel (9 μm particles in 50 μm square channels (Di Carlo *et al.*, 2007)), the effect would be negligible in a much larger aperture fracture because the effect would be localized to the wall, only occurring over a very small fraction of the aperture; however, the shear induced migration away from the center of a fracture should be accounted for in the transport of particles in fractures as it occurs over nearly the entire fracture aperture.

The goal of this study is to elucidate upon particle transport mechanisms in fractured media rooted in hydrodynamics and fracture geometry by calibrating a transport model using experimental data. While it is evident that the geometry of a fracture affects the flow field, and hence the transport of particles, there are other hydrodynamic forces (such as shear) which are typically not considered. This study also examines the mechanisms involved in transport (fluid velocity, diffusion, shear, gravity) both to each other and the fluid velocity field by including them in the model. Finally, the calibrated transport model is used to examine the local variations in the fracture geometry (e.g. pinch points) to elucidate upon their effect on particle transport and ultimately, the effluent concentration profiles. This work substantiates the dominant mechanisms involved in transport of particles in saturated fractures and how these mechanisms affect effluent concentrations of those particles.

4.2 Methods

Experimental Fracture Creation

A variant of the random field generation code, SPRT2D written in python (Gutjahr, 1989; Zheng *et al.*, 2009b,a), was employed to generate two 2D fractures for both the simulations and physical model experiments. Two-dimensional fractures were employed as fully realized 3D variable aperture fractures would complicate the analysis of geometric effects on particulate transport; a 3D fracture geometry implies variability in three axes, which would cause hydrodynamic effects on particles to be combined in a space that is not easily visualized. Limiting the variability of the fracture aperture field (but not the fracture itself) to 2D allows for the hydrodynamic effects to be more easily studied via comparison of simulations to experimental data. In this study, the fractures used in both simulations and experiments were quasi-3D in the sense that the variable aperture part of the fracture was in the xy-plane, while in the z-axis there was no variation creating a fracture where two walls are rough while the other two are flat parallel plates.

The two randomly generated aperture fields were used to fabricate the experimental fractures by laser-etching (Epilog Mini 24 Laser, Eiplog Laser, Golden, CO, USA) the 2D aperture field into poly(methyl methacrylate) (PMMA) blocks to a depth of 2.3 mm (this depth exists in the z-direction). The cut fractures were sealed with an additional PMMA block and epoxy, thus creating the quasi-3D experimental fractures. For the purposes of this study, the fracture plane with variability is the xy-plane and the dimension without variability (2.3 mm) is the z-direction (Figure 4.1). The total volume of each fracture was approximately 1.4 mL. The characteristics used to generate these fractures are given in Table 4.1 with resolution of 0.5 mm in the x-direction. Each fracture consists of lines connecting points in the x-direction, thus the aperture values in the y-direction were known exactly. The mean apertures for both fractures were chosen to be equal at 2.03 mm so that the effect of different geometries could be compared between fractures. Other measurable characteristics were kept nearly identical (e.g. aperture field standard deviation, aperture field correlation length, mean elevation of the mid-aperture field, standard deviation of the mid-aperture field, and fracture length) (Table 4.1). The only characteristic not kept similar between the two fractures was the mid-aperture field elevation correlation length; these were set to 70.84 mm and 34.40 mm respectively, which is large compared to the fracture length of 300 mm. While the mid-aperture field elevation correlation length values are different, the fact that they are large means that significant changes in the mid-aperture field cannot occur over short distances, and therefore the two fractures very similar. The mean aperture and standard deviation values used in this study are consistent with those measured in various field settings (Snow, 1970).

Experimental Methods

Figure 4.1 shows a schematic of the particle transport experiment as conducted in each of the two PMMA fractures. The influent and effluent ends of the fracture were each fitted with a 2 cm long end cap, with a width of 2 mm and depth of 2.3 mm.

A syringe pump was connected to the influent end cap to generate controlled steady state flow in the fracture (Figure 4.1). The effluent end cap housed a light emitting diode (LED) with peak emission at 440 nm, and was fitted with a spigot to enable the collection of all effluent flow. The LED was powered using a constant current power supply as specified by the manufacturer. A 600 μm diameter optical fiber was inserted in the outlet end cap, opposite to the LED, which provided the light intensity data to a USB spectrometer tuned to collect measurements at 440 nm (USB2000, Ocean Optics, Dunedin, FL, USA) (Figure 4.1). The USB transmitted the collected data to a computer.

A 0.01% by volume Triton X-100 solution was used in the experiments to ensure that only geometric and hydrodynamic mechanisms influenced transport (Microspheres and Guide, 2012). Triton X-100 is a surfactant which prohibits particle-particle aggregation and particle-fracture wall adhesion. It should be noted that the water-Triton X-100 solution did not significantly differ from water in either density or viscosity. Three volumetric flow rates were employed in these experiments: 0.00835 mL/min, 0.0835 mL/min, and 0.363 mL/min, which correspond to average horizontal flow rates of 2.6 m/day, 26 m/day, and 114 m/day respectively.

Two sizes of yellow-green fluorescent non-carboxylated latex microspheres (Polysciences, Inc., Warrington, PA, USA) were used in these experiments: 1) a virus analogue with a mean diameter of 0.046 μm (0.005 μm standard deviation); and 2) a bacteria analogue with a mean diameter of 0.55 μm (0.015 μm standard deviation). The density of both latex microspheres is 1.05 g/mL (Mondal and Sleep, 2013; Sheet, 2013).

The effluent microsphere concentration was observed by reading the intensity of the LED using the USB spectrometer. The total intensity reading time was kept at a constant 50 ms per sample for all experiments. The intensity information was converted to absorbance, which was then converted to concentration data using calibration curves. Absorbance data were sampled every 56 seconds for the 2.6 m/day flow rate, 5.6 seconds for the 26 m/day flow rate, and 1.39 seconds for the 114 m/day simulations. This produced approximately 2500 absorbance readings for each experiment.

The microsphere tracer experiments were initiated by injecting approximately 9.3×10^{12} microspheres (diameter 0.046 μm) or 5.6×10^{9} microspheres (diameter 0.55 μm) into the influent end cap at a volume of 0.05 mL using a syringe. The injection produced a slug approximately 1.2 cm in length in the end cap. A minimum of 15 fracture volumes of fluid were passed through the fracture to ensure complete recovery of the microspheres. These experiments were conducted in both fractures, using two different microsphere sizes at three different flow rates. Each experiment was repeated three times, and since the results were highly repeatable, the effluent breakthrough curves (BTC) were averaged for comparison to simulation results.

Transport Simulations

The governing equations of flow for this system are the steady-state Navier-Stokes equations for an incompressible fluid with the no-slip condition imposed at the fracture walls (Bird *et al.*, 2002):

$$\rho \left(\mathbf{u} \cdot \nabla \mathbf{u}\right) \mathbf{u} = \eta \nabla^2 \mathbf{u} - \nabla p \tag{4.1}$$

$$\nabla \cdot \mathbf{u} = 0 \tag{4.2}$$

where ρ [ML^{-3}] is the density of the fluid, $\mathbf{u}$ is the fluid velocity vector, η [$ML^{-1}t^{-1}$] is the dynamic viscosity of the fluid, and$p$ [$ML^{-1}t^{-2}$] is total pressure. Typical fluid properties for water were used in these calculations: $\rho = 1.00$ g/mL and $\eta = 0.0009$ Pa·s at a temperature of 298K. For the purposes of this study, equations 4.1 and 4.2 were solved in 2-dimensions using COMSOL Multiphysics (COMSOL, Inc., Burlington, MA, USA) which employs finite element analysis (FEA) with approximately 35000 elements solved in the 2D varying fracture geometry (xy-plane) similar to the approach used by Cardenas *et al.* (2007). The no slip condition was employed on the fracture walls and there is no matrix flow. In order to realize a 3D flow field, the velocity of a particle the 2D flow field (based on the (x,y) coordinate of the particle) was taken and multiplied by a weighting factor based on a parabolic flow profile that is zero when z = 0 mm and 2.3 mm (the depth of the fracture)(Bird *et al.*, 2002):

$$W = \left(\frac{-6}{h^2}\right)\left(z - \frac{h}{2}\right)^2 + \frac{3}{2} \tag{4.3}$$

where h is the aperture along the z-axis (in this study, $h = 2.3$ mm) and z is the z location of the particle (from 0 to 2.3 mm). This weight function W is then multiplied by the velocity from the average FEA developed velocity field; however, it is assumed that this parabolic field does not permit the fluid to have a non-zero component in the z-direction. It should also be noted that in parabolic flow, the average velocity is 2/3 of the maximum velocity; hence the maximum weighting factor is 3/2. The pressure difference inducing flow across the fracture in the 2D flow field was optimized by numerically integrating the 3D flow field at the outlet to match each volumetric flow rate used in the experiment. For fracture 1, the head differences across the length of the fracture are 0.0009 cm, 0.009 cm, and 0.039 cm for volumetric flow rates of

0.00835 mL/min, 0.0835 mL/min, and 0.363 mL/min respectively. For fracture 2, the head differences across the length of the fracture are 0.0015 cm, 0.015 cm, and 0.065 cm for volumetric flow rates of 0.00835 mL/min, 0.0835 mL/min, and 0.363 mL/min respectively.

Particle transport was based on a RWPT scheme which determines transport based on the flow field and random diffusion. A picture of the transport process emerges when many particles are tracked in this manner. This particle centered approach enables the direct analysis of the hydrodynamic effects on the transport of the particles of the system and is a relatively straight-forward and efficient computation method. The basic equation for RWPT is (Tompson and Gelhar, 1990):

$$\mathbf{X}_{t+1} = \mathbf{X}_t + \mathbf{V}\left(\mathbf{X}_t\right)\Delta t + \boldsymbol{\zeta}\left(0,1\right)\sqrt{2D\Delta t} \tag{4.4}$$

where $\mathbf{X}_t$ [L] is the 3D position vector of the particle at time t, $\mathbf{V}\left(\mathbf{X}_t\right)$ [Lt^{-1}] [Lt-1] is the fluid velocity vector at the position $\mathbf{X}_t$, Δt [t] is the time step, $\boldsymbol{\zeta}\left(0,1\right)$ [-] is a 3D vector with each element randomly chosen from a Gaussian distribution with mean of 0 and standard deviation of 1 to mimic the random diffusion process, and D [L^{2}t^{-1}] is the diffusion coefficient. The diffusion coefficient for a particle is typically computed using the Stokes-Einstein equation:

$$D = \frac{k_B T}{3\pi\eta d_p} \tag{4.5}$$

where k_B is the Boltzmann constant [ML^{2}t^{-2}T^{-1}], T [T] is the absolute temperature, η [ML-1t-1] is the dynamic viscosity of water, and d_p is the particle diameter [L]. In this study, the approximate temperature of the room in which the experiments were conducted was used: $T = 298$K.

In previous studies, inclusion of gravity in the RWPT algorithm was accomplished by adding the velocity of the particle induced by gravity multiplied by the time step, Δt, to the particle motion equation (equation 4.4) (Chrysikopoulos and James, 2003; James and Chrysikopoulos, 2011). The gravitational velocity term, $\mathbf{U}_g$, is defined as (Gregory, 2006):

$$\mathbf{U}_g = \begin{bmatrix} 0 \\ 0 \\ -\frac{d_p^2 g \Delta\rho}{18\eta} \end{bmatrix} \tag{4.6}$$

where g [Lt^{-2}] is the gravitational constant and $\Delta\rho = \rho_p - \rho_{water}$ [ML^{-3}], ρ_p is the density of the particle and ρ_{water} is the density of water. Gravity only acts in the z-direction in this study as indicated by equation 4.6.

The effect of shear on particles is proportional to the negative of the spatial derivatives of the flow field (Bird *et al.*, 2002; Rusconi *et al.*, 2014). To approximate the effects of shear in this simulation, only the largest velocity spatial derivatives were considered. The largest spatial derivatives are associated with the velocity field in the direction of flow(x-direction). As the largest spatial derivatives dominate the remaining spatial derivatives, and as such the shear term used in this study, $\mathbf{S}(\mathbf{X}_t)$ [t^{-1}], was computed using (Bird *et al.*, 2002):

$$\mathbf{S}(\mathbf{X}_t) = \begin{bmatrix} \frac{\partial V_y}{\partial x} \\ \frac{\partial V_x}{\partial y} \\ \frac{\partial V_x}{\partial z} \end{bmatrix} \tag{4.7}$$

where $\mathbf{V}(\mathbf{X}_t) = [V_x, V_y, V_z]^T$ is defined in local coordinates. It should be noted that the x component of $\mathbf{S}(\mathbf{X}_t)$ is very small as flow is in the x-direction. The shear term in the RWPT computation was multiplied by the radius of the particle as the effect of fluid shear is proportional to the size of the sphere and then multiplied by the time step, Δt, in order to achieve a distance traveled by the particle.

Finally, in this study, coefficients are added to several terms in the RWPT algorithm as follows:

$$\mathbf{X}_{t+1} = \mathbf{X}_t + \alpha\mathbf{V}(\mathbf{X}_t)\Delta t + \beta\boldsymbol{\zeta}(0,1)\sqrt{2D\Delta t} - \gamma\mathbf{S}(\mathbf{X}_t)\frac{d_p}{2}\Delta t + \mathbf{U}_g\Delta t \tag{4.8}$$

where α, β, and γ are coefficients for each term. The diffusion parameter, β, is multiplied by a value from a Gaussian distribution, $\boldsymbol{\zeta}(0,1)$ as this form of motion is random. The flow field used in the simulations was steady state; however, the introduction and movement of particles in the fluid would cause minor local variations in the flow field that may affect the transport of the particles. In order to account for the variation in hydrodynamics without requiring the computational overhead of resolving the Navier-Stokes equations (equations 4.1-4.2) for each time step, a similar approach of modifying the velocity and shear parameters, by drawing them from a distribution, was applied. For each time step and each particle, the parameters α and γ were drawn randomly from Gaussian distributions with a given mean (denoted α_{mean} and γ_{mean}, respectively) and standard deviation (denoted α_{SD} and γ_{SD}, respectively)(Table 4.2). If, for example, α_{mean} is found to be less than 1 ($\alpha_{mean} = 1$ and $\alpha_{SD} = 0$ in standard RWPT, equation 4.4), this indicates that the particles are, on average, not traveling at the same velocity as the local steady-state flow field, while an $\alpha_{SD} > 0$ value indicates local disturbances in the flow field that vary randomly with location. A final parameter utilized in this modified RWPT approach concerns the situation of a particle interacting with a fracture wall, specifically, when a collision and bounce occurs. Physically, this bounce should not be perfectly elastic and the resulting vector accounting for particle movement away from the wall was scaled by the collision efficiency parameter, denoted τ, with the maximum vector being a perfectly elastic collision ($\tau = 1$) (Table 4.2). Particle-particle aggregation and particle-wall adhesion was neglected in these simulations, as the experiments included Triton X-100 to eliminate these interactions. The result of this modified RWPT algorithm is that six different parameters (α_{mean}, α_{SD}, β, γ_{mean}, γ_{SD}, and τ) must be optimized. As well, equation 4.8 reduces to the standard RWPT algorithm if α_{mean} =1, $\alpha_{SD} = 0$, $\beta = 1$, $\gamma_{mean} = 0$, and $\gamma_{SD} = 0$. This particle centered approach enables easy extraction of the unique aspects of flow and transport through the examination of each term in equation 4.8, which can be done on a particle by particle basis.

For a given set of experimental parameters (fracture, particle size and flow rate), the RWPT algorithm was initialized with 1 000 particles randomly seeded across a 1.2 cm length in the inlet end cap to mimic the experiments (Figure 4.1). The particles were then tracked with a time step chosen to not allow more than 10% of the average fracture aperture of movement in a single step based on the average velocity profile. Based on this condition, a series of simulations was conducted with time steps decreasing in length. After examining the BTCs of the simulations with a decreasing set of time steps, it was determined that time stepping could be limited to 10 seconds for 2.6 m/day flow rates, 1 second for 26 m/day flow rates, and 0.2 seconds for 114 m/day flow rates as smaller values for the time step did not significantly alter the BTCs. Furthermore, these time steps allowed for reasonable simulation times while producing reasonable results, and are comparable to other time steps utilized in other studies (James *et al.*, 2005; Zheng *et al.*, 2009a).

For each of the 12 fracture-particle size-flow rate experiments, the parameters of a modified RWPT simulation were optimized using a genetic algorithm with simulations running on a cluster computing system (SharcNET: http://www.sharcnet.ca). The genetic algorithm uses a fitness function to test each set of parameters used in the process, which is minimized during the optimization process. The fitness function used for each experiment-simulation comparison was devised to split up the time values into 75 steps, count all simulated particles in each step, compare this result to the expected number of particles derived from the experiment, and finally minimize the sum of the squares of the difference in particles numbers between simulation and experiment at each time step. For each set of experimental parameters (fracture, particle size and flow rate), approximately 3000 simulations were completed before an optimal values for the simulation parameters (α_{mean}, α_{SD}, β, γ_{mean}, γ_{SD}, and τ) were reached. The optimal values of each parameter are given in Table 4.2. The top 10 optimal simulations for each of the 12 fracture-particle size-flow rate scenarios were recorded for analysis.

Methods of Simulation Analysis

Once the optimal parameter values for each of the 12 fracture-particle-flow rate experiments were determined, these calibrated simulations were performed with 10 000 particles for comparison to the experimental BTCs. The data accumulated from the optimal simulations and experimental BTC were converted to a particle mass fraction where the divisor is the total mass injected into the system for ease of comparison.

Binning of the time axis of the BTC into 75 bins was performed with the last 25% of the bins accounting for the tail because the number of particles in the tail was comparatively low and this provided a more accurate representation of the BTC. Furthermore, the time axis was converted to fracture volumes for ease of comparison between experiments and simulations. One of the main goals of this study was to compare the parameters of the RWPT model used in this work (equation 4.8) across various flow rates and both fractures. This comparison was used to assess the effects of flow on the individual transport mechanisms. To compare parameter trends across flow rates and fractures, the top 10 most optimal parameter sets were collected for each of the 12 fracture-particle size-flow rate scenarios, and the median, maximum, and minimum values were computed for each parameter.

Another goal of this study is an analysis of transport pathways in the fracture and how this path is affected by local geometry. This analysis was performed using calibrated simulations with optimized parameters. For elucidation of the effects of geometry, the particle paths during transport in the 2D xy-plane were examined as this plane had a variable aperture field. Three sections (lengths in x) were selected in each fracture to show the effects of the variable aperture on the transport of particles. In order to demonstrate the most likely locations for particles to be present in the fracture section, each 2D section was divided into approximately 1500 triangular regions. Then, for each triangular region each unique particle that entered the region was counted. Finally, to compute the probability of a particle entering the triangular region, the count of unique particles entering was divided by the total number of particles in the system (10 000). The resultant probability field was then calculated.

4.3 Results and Discussion

Analysis of Breakthrough Curves

Figures 4.2 and 4.3 show the experimental and calibrated simulation BTCs for both fractures at all flow rates for the 0.046 μm microspheres and 0.55 μm microspheres respectively. In each figure, the fracture 1 results are shown in panels A-C with increasing flow rate (2.6 m/day, 26 m/day and 114 m/day, respectively) and fracture 2 results are shown in panels D-F with increasing flow rate. The experimental BTCs all showed increasing dispersion of the particles as fluid velocity increased in a given fracture and, therefore higher flow rates induce greater hydrodynamic-dispersive effects on particle transport.

The calibrated simulations for both the 0.046 μm and the 0.55 μm microspheres in fracture 1 match the peak concentration measured in the physical experiments across all flow rates (Figure 4.2, 4.3). For the 0.046 μm particles, the concentration of the BTC tail was higher in the simulations than observed in the experiments (Figure 4.2A, D), particularly at the 2.6 m/day flow rate; however, the simulated higher tail concentration values decrease towards the experimental BTCs as the flow rate increases (Figure 4.2A-C, D-F). Simulated BTC tail concentrations of 0.55 μm particles were also higher in fractures 1 and 2, but to a lesser degree than for 0.046 μm particles. However, the tail only decreases towards experimental observations as flow rate increases in fracture 2 (Figure 4.2D-F). During the experimental analysis it was noted that the detection of the larger microspheres produced higher absorbance values and thus the concentrations of larger particles were more accurately resolved. This observation suggests that the discrepancy between simulated and observed BTC tail concentrations may be caused by the spectrophotometer/optical fiber system, which underestimates low concentrations. Another characteristic of the BTCs is a marked shoulder observed in the experimental BTCs from fracture 1 with 0.55 μm microspheres at 2.6 m/day at approximately 1.5 fracture volumes (Figure 4.3A) and at 26 m/day at about 2.5 fracture volumes (Figure 4.3B). These shoulders were very well reproduced by the simulations (Figure 4.3A-B). The likely mechanism creating this shoulder is shear making some particles travel in slower flow lines. For the slowest flow rate, the shoulder is near the peak concentration and begins before two fracture volumes (Figure 4.3A). With increasing flow rate, the shoulder is observable at approximately three fracture volumes (Figure 4.3B). At the fastest flow rate, the shoulder is no longer observable being largely enveloped by the increased dispersion (Figure 4.3C). In this case, the greater dispersion associated with greater flow rates out competes the shear force smoothing the shoulder.

It is important to note that Figures 4.2 and 4.3 also show that the initial arrival of the particles was observed earlier in the experiments than in the simulations. This effect increases with increasing flow rate, such that at 114 m/day, the experimental particles are detected approximately 0.6 fracture volumes before the simulated particles (Figure 4.2 C, F; Figure 4.3 C, F); however, the initial arrival time and peak concentrations are quite well matched by the simulation at 2.6 m/day for both 0.046 μm and 0.55 μm microspheres. The earlier detection of experimental microspheres appears to be less pronounced in fracture 1 than in fracture 2, which is likely related to differences in the geometries between the two fractures. These results support the notion that hydrodynamic dispersion increases with flow rate, but the dispersion is not well replicated by the simulations at the fastest flow rates. The model used in this study incorporates a steady state flow field in the xy-plane and an approximated parabolic flow field along the z-axis. This approximation may not account for increased hydrodynamic effects caused at the fastest flow rates (e.g. eddies or turbulence) that may also increase the dispersion observed in the experiments.

Model Parameter Analysis

Figure 4.4 shows the parameter values relative to that observed at the 2.6 m/day flow rate across each flow rate for 0.046 μm particles in fracture 1 and fracture 2 (Figure 4.4A and B respectively) and for 0.55 μm particles in fracture 1 and 2 (Figure 4.4C and D respectively). In order to compare parameters across flow rates and fractures, the top 10 most optimal parameter sets were collected for each of the 12 fracture-particle size-flow rate scenarios. As all of the top 10 simulations were reasonable representations of the experimental BTCs, the median, maximum, and minimum values were collected for each parameter. Then, for a given parameter unique to a fracture, flow rate, and microsphere size, the parameter values for 26 m/day and 114 m/day flow rates were normalized to the 2.6 m/day value, hence, the value for the 2.6 m/day parameters is shown as 1 across all parameters, fractures and particle sizes. The maximum/minimum (normalized) value is shown as the upper/lower error bar respectively thus showing the spread in the top 10 optimal parameter sets in their entirety.

Several trends were observed in these results. In the RWPT model used in this study, advection is scaled by the parameter α_{mean}. If α_{mean}=1, then the particles are moving at the local fluid velocity; however, if α_{mean} <1, then drag or dispersive mechanisms are causing particles to not move at the full fluid velocity. For each microsphere size and each fracture, the α_{mean} decreases with increasing flow rate (Figure 4.4, Table 4.2), suggesting that drag forces increase with flow rate. The α_{mean} values were all between 0.43 and 0.58 suggesting that advection is affected by drag and dispersion at all flow rates (Table 4.2). This effect is does not align with to the α_{mean}=1 and α_{SD}=0 value typically used in the standard RWPT algorithm (equation 4.4). For both particle sizes, the α_{SD} decreases with increasing flow rate in fracture 1 (Figure 4.4A, C), but in fracture 2 the trend is increasing with increasing flow rate (Figure 4.4B, D), which is a numerical representation of the fact that dispersion with flow rate (Figure 4.2, 4.4).

Diffusion has been shown to obey the Stokes-Einstein diffusion coefficient equation (equation 4.5) in viscous fluids reasonably well (Dunstan and Stokes, 2000; Ernst and Kohler, 2013), thus the parameter, β, was only permitted to take on values from 0.1 to 2. The diffusion coefficient increased with increasing velocity up to 26 m/day for all cases, but there is no obvious trend between 26 m/day and 114 m/day (Figure 4.4). The β values for 0.046 μm microspheres were generally lower than the β values found in the same fracture and at the same flow rate for 0.55 μm microspheres (Table 4.2); however, the smaller particles did have higher overall diffusion components (total diffusion component, $\beta\boldsymbol{\zeta}\left(0,1\right)\sqrt{2D\Delta t}$) than the larger particles. A possible explanation for this is that the larger particles (0.55 μm) create greater disturbances in the local flow field than the smaller ones (0.046 μm), which, while minor, are not accounted for in the steady-state flow field used in the simulations but could cause minor variations in the movement of the particles. These variations in the movement should be accounted for in the diffusion term, and thus the larger β value for 0.55 μm particles over those for 0.046 μm particles must account for this effect.

The collision efficiency coefficient, τ, measures the energy lost when a particle bounces off of a wall by scaling the movement vector post bounce. This coefficient followed no obvious trend when examined across flow rates for a particular fracture and particle size. The values of τ for the virus sized microspheres (0.046 μm) were observed to be significantly smaller, approximately 0.05, than for the bacterial sized microspheres (0.55 μm), approximately 0.5 (Table 4.2). This may be caused by the fact that the laser cut surface of the fracture wall is likely slightly rough, and this roughness may inhibit the bouncing of the smaller particles while the larger particles are large enough to not be affected by the roughness and bounce off of the wall as though it was smooth. Another possible explanation is that the larger particles carry more momentum and accordingly bounce off the fracture walls with greater efficiency.

The mean shear coefficient, γ_{mean}, directly scales the effect of shear on the particles. Shear moves particles away from the center of the fracture. This coefficient generally decreased with increasing flow rate, as does the standard deviation value of the shear coefficient distribution (Figure 4.4). It should be noted that this component of movement ($\gamma \mathbf{S}\left(\mathbf{X}_t\right) \frac{d_p}{2} \Delta t$) generally represented less than 1% of the advective term ($\alpha \mathbf{V}\left(\mathbf{X}_t\right) \Delta t$). Figure 4.5 shows the mean distance of the particles to the mid-aperture plane (xy plane) normalized to the local aperture throughout the fracture. In general, for each particle size and fracture, the mean distance of the particles from the mid-aperture is approximately the same across flow rates (Figure 4.5). Slow flow rates generally result in a slightly higher mean distance from the mid-aperture (Figure 4.5) except in fracture 2 from 160 mm to approximately 220 mm where the effect is reversed (Figure 4.5B, D). Particles traveling at slower flow rates diffuse more during a given time step compared to faster flow rates indicating that particles at slower flow rates are more likely to be away from the mid-aperture of the fracture. Particles farther away from the mid-aperture experience greater shear forces, thus moving them even farther from the mid-aperture. Where this trend is reversed in fracture 2 (from 160-220 mm), the likely cause is the local geometry of the fracture.

Figure 4.6 shows experimental BTCs, the calibrated simulation BTCs and BTCs from simulations where shear has been neglected by setting $\gamma_{mean} = 0$ and $\gamma_{SD} = 0$ but keeping the other parameters set to the optimized values. The BTCs representing the experiments and simulations conducted at flow rates 2.6 m/day and 26 m/day were chosen for examination as the model is more robust at these flow rates (Figure 4.6). Figure 4.6A shows both experimental and simulation data for fracture 1 at 2.6 m/day, and shows that the model including shear represented the experimental BTC of 0.55 μm microspheres well, while the model without shear eliminated the obvious shoulder from the simulation and resulted in slightly higher peak concentration than observed in the experiment. Figure 4.6B shows both experimental and simulation data for the transport of 0.55 μm particles in fracture 1 at 26 m/day, and again shows the model fit worsens when shear is not considered. The model excluding shear shows a marked drop in concentration followed by an increasing concentration at 1.5 fracture volumes, which is not observed in either the experiment or simulations including shear. Figures 4.6C and D show that the simulation results in higher peak effluent concentrations of 0.046 μm microspheres than observed in experiments when shear is neglected in the model in fracture 2 at 2.6 m/day and 26 m/day respectively.

These data show that shear has a relatively minor, but not negligible, effect on the transport of particles in the experimental fractures used in this study. In general, shear acts to slightly stretch out the BTC, which is expected as shear force increases with increasing distance from the mid-aperture or center of the fracture (the center is the location of the peak velocity). Thus, the bulk of the particles transported in the fastest flow lines remain relatively unaffected by shear but particles in the slower flow lines migrate to even slower flow lines thus stretching the BTC by decreasing the peak concentration (Figure 4.6). It should be noted that the microspheres used in the experiments and simulations do not have the same shape as the viruses or bacteria that they are used to represent; it is likely that the shear parameters associated with different shaped particles would be different. In particular, the SD of the shear parameter would be expected to be larger for non-spherical particles as the hydrodynamic effect would depend on the orientation of the particle (Masaeli *et al.*, 2012).

Effect of Fracture Geometry on Transport

When comparing the transport of 0.046 μm particles at 2.6 m/day in fractures 1 and 2, the BTCs show remarkable differences. The experimental BTC in fracture 1 has a much lower peak concentration and shows much greater dispersion with higher effluent particle concentrations observed at two fracture volumes (Figure 4.2A) than what is observed in fracture 2. The BTC observed in fracture 2 displays much less dispersion with the effluent concentration curve tapering off before 2 fracture volumes (Figure 4.2D). Similarly, with 0.55 μm particles at 2.6 m/day, the BTC in fracture 1 also shows much greater dispersion (Figure 4.3A) than is observed in fracture 2 (Figure 4.3D).Furthermore, there is a distinct shoulder in the transport of 0.55 μm particles in fracture 1 at 2.6 m/day that is not observed in fracture 2 (Figure 4.3A, D). These observations may be extended to faster flow rates, but focusing on the groundwater velocity of 2.6 m/day, it is obvious that despite the very similar statistical characteristics of the two fractures used in this study (Table 4.1), the effluent BTCs are distinctly different for both particle sizes. This observation suggests that there is an important geometrical aspect to the transport of particles in the fractures is responsible for the differences in the BTCs.

Figures 4.7Ai-Ci and 4.8Ai-Ci show the FEA generated average flow field and a map of particle entry probabilities in 2D (xy plane) sections of fracture 1 and 2. Figures 4.7Aii-Cii and 4.8Aii-Cii also include histograms of the probabilities of entry of the triangular regions in each fracture section. The histograms are hue coded to the map of entry probabilities with black being lowest probability and white being the highest possible probability in the fracture section. The 2.6 m/day flow rates were examined using the 0.55 μm particle transport in fracture 1 (Figure 4.7) and the 0.046 μm particle transport in fracture 2 (Figure 4.8).

The simulations for the 0.55 μm particles in fracture 1 show that near the inlet of the fracture, from 15-55 mm, the particles are well distributed across the aperture of the fracture (Figure 4.7Ai). As well, in the 15-55 mm section of fracture the distribution of entry probabilities is fairly Gaussian with a mean of about 0.15 (Figure 4.7Aii). Further along the fracture length, from 85-125 mm, the particles are forced into faster stream lines due to a pinch point (93 mm), and the larger aperture region immediately downstream of the pinch point (95 mm) does not have particles sampling the entire space (Figure 4.7Bi). The effect of this pinch point forcing particles into faster stream lines promotes an artificial boundary and results in the majority of the particles traveling near the center of the 2D fracture (Figure 4.7Bi). The histogram associated with this region shows that nearly half of the fracture is essentially not sampled by particles during the transport process (Figure 4.7Bii). The particle transport pathway undergoes another important change caused by the local geometry in the section from 255-295 mm (as shown in Figure 4.7Ci). In particular, from 255 mm to 272 mm, the particles are only in the center portion of the fracture; however, at 272 mm a severe pinch point with a slight decline in the y direction forces all of the particles into the lower half of the fracture only (Figure 4.7Ci, Cii). Transport simulations of the 0.046 μm particles in fracture 2 show that immediately downstream of the inlet the particles have already begun to travel in only the upper portion of the fracture (30-57 mm), at which point a pinch point again forces nearly all particles into the center of the fracture (Figure 4.8Ai). At 66 mm, there is a large aperture section in the upper portion of the fracture which has a relatively low velocity and is not accessed by the particles (Figure 4.8Ai). The histogram of probabilities shows that particles do not sample approximately 40% of the aperture (Figure 4.8Aii), and a few aperture regions have nearly 80% probability that a particle will enter. The particles remain in the center portion of the fracture until the pinch point at 167 mm (Figure 4.8Bi), where there is a slight decline in the geometry forcing the flow to carry the particles into the lower two thirds of the fracture (Figure 4.8Bi). Nearly 40% of this section is not sampled by the particles while the probability that other regions will be sampled is nearly 100% (Figure 4.8Bii). Downstream, the particles in the lower portion are then forced into the upper portion of the aperture by the narrowing at 208 mm (Figure 4.8Ci). The particles remain in these stream lines until the geometry changes at 238 mm force all particles into the center of the aperture, and only a few particles are follow streamlines near the fracture walls (Figure 4.8Ci). In this section, 40% of the aperture is not sampled by the particles with particles not being observed in the lower part of the majority of this section (Figure 4.8Cii).

The particle probability regions show that when large changes in the fracture geometry occur, the particles are forced to follow specific flow lines and do not sample the entire aperture. In particular, local pinch points and how these pinch points modify the local flow field can force the majority of particles into specific aperture regions. Therefore, particulate contaminants such as viruses and bacteria may be forced into aperture regions where there is a diminished chance of contact with, and therefore adhesion to, a fracture wall (e.g. Figure 4.7Ci, Figure 4.8Bi). These simulations demonstrated several instances where there is little chance of encountering a fracture wall as the bulk of the particles follow flow lines well away from both walls (Figure 4.7Bi). Therefore, the local aperture geometry can affect the retention of particulates in a fracture, as it can either enhance or prevent the likelihood of a particle contacting a wall, which is the first step required for retention. Retention ultimately affects the shape of the effluent BTC through: time of first arrival, peak height, and tail shape. The shape of the BTC is further influence by the fact that geometry changes generally force particles are into aperture regions where the flow is faster than the average velocity; this results in earlier peak arrival times. This work demonstrated that these effects vary significantly between two fractures with different geometries but the same aperture field statistics (i.e. aperture field mean, aperture field standard deviation, aperture field correlation length, mean elevation of the mid-aperture field, standard deviation of the mid-aperture field, and fracture length). Therefore, aperture field statistics in the absence of exact aperture measurements do not provide sufficient information to predict particle transport pathways, and therefore retention, in fractures.

4.4 Conclusions

Analysis of the parameters and movement of the particles in the simulation revealed that, on average, the particles only travel at approximately half of the fluid velocity suggesting that there is greater drag on particles than is generally considered in RWPT simulations. In fact, in the reported literature, particles are assumed to travel at the same velocity as the fluid in this component of movement. Furthermore, effect of shear is small but not negligible with the shear component of particle movement being less than 1% of the particle movement caused by the fluid velocity field; however, this movement did demonstrate a decrease in the peak concentration of both particle sizes in the effluent. Shear was shown to increase the dispersive effect of the fluid velocity field on the particles being transported. In this study, both experimental and simulated particles were spherical; however, non-spherical particles would expose different shapes or faces to the local hydrodynamic effects and thus the shear parameter will likely have a greater distribution of values, in this case, effectively increasing the standard deviation associated with the parameter γ.

Investigation into the transport of particles in light of the geometry of the fractures provided insight into particle pathways through a fracture. The simulations at the groundwater analogous average velocity of 2.6 m/day demonstrated that a significant narrowing followed by the fracture opening up could direct the majority of particles into certain regions of the fracture. There were cases where particles ended up in only the upper or lower half of the fracture. As well, there were instances of the bulk of the particles only being transported in the very center of the fracture where advection is fastest. The importance of these observations is two-fold: 1) while particles being transported in fractures deposit and adhere to the fracture surface resulting in greater dispersion and retention, this data shows that there are segments of the fracture where parts of the fracture wall are unavailable for deposition effectively decreasing potential retention; and 2) as particles are transported in the fracture, the bulk of the transport may occur in faster flow lines. Ultimately, these observations show that particulate contaminants could not only move out of fractures at higher concentrations than expected but also much faster than expected after correcting for drag during advection. Furthermore, it is not possible to determine the nature and effect of a specific pinch point on particle transport path from a general fracture statistic (e.g. aperture mean, standard deviation, coefficient of variation, field correlations).

Chapter Contents

The contents of this chapter are in preparation for submission to *Water Resources Research*. The authors are Sean P. L. Cianflone, Vickram Lakhian, and Sarah E. Dickson.

Table 4.1: Fracture Statistics

Parameter	**Fracture 1**	**Fracture 2**
Aperture mean (μ_b)	2.03 mm	2.03 mm
Aperture standard deviation (σ_b)	0.54 mm	0.58 mm
Aperture field correlation (λ_b)	56.71 mm	52.12 mm
Mid-aperture field mean (μ_z)	-0.02 mm	0.01 mm
Mid-aperture field standard deviation (σ_z)	0.32 mm	0.29 mm
Mid-aperture field correlation (λ_z)	70.84 mm	34.40 mm
Fracture Length (excluding end caps)	300 mm	300 mm

Table 4.2: Simulation Parameters

Fracture	Flow Speed (m/day)	Particle (μm)	Experimental Recovery	**Parameters** Velocity α_{mean}	Velocity α_{SD}	Diffusion β	Shear γ_{mean}	Shear γ_{SD}	Collision τ
1	2.6	0.046	79%	0.533	0.152	0.409	1.163	0.327	0.055
1	26	0.046	80%	0.441	0.138	1.038	0.983	0.233	0.054
1	114	0.046	93%	0.442	0.023	0.930	0.569	0.198	0.041
2	2.6	0.046	80%	0.572	0.123	0.428	1.699	0.732	0.108
2	26	0.046	90%	0.455	0.202	0.601	0.961	0.251	0.041
2	114	0.046	99%	0.449	0.190	0.568	0.115	0.012	0.046
1	2.6	0.55	84%	0.549	0.246	0.942	0.054	0.018	0.348
1	26	0.55	90%	0.530	0.174	1.151	0.048	0.017	0.733
1	114	0.55	96%	0.460	0.195	1.037	0.060	0.025	0.537
2	2.6	0.55	78%	0.557	0.107	0.811	0.025	0.009	0.691
2	26	0.55	80%	0.461	0.106	1.269	0.024	0.003	0.700
2	114	0.55	94%	0.430	0.177	1.462	0.003	0.001	0.450

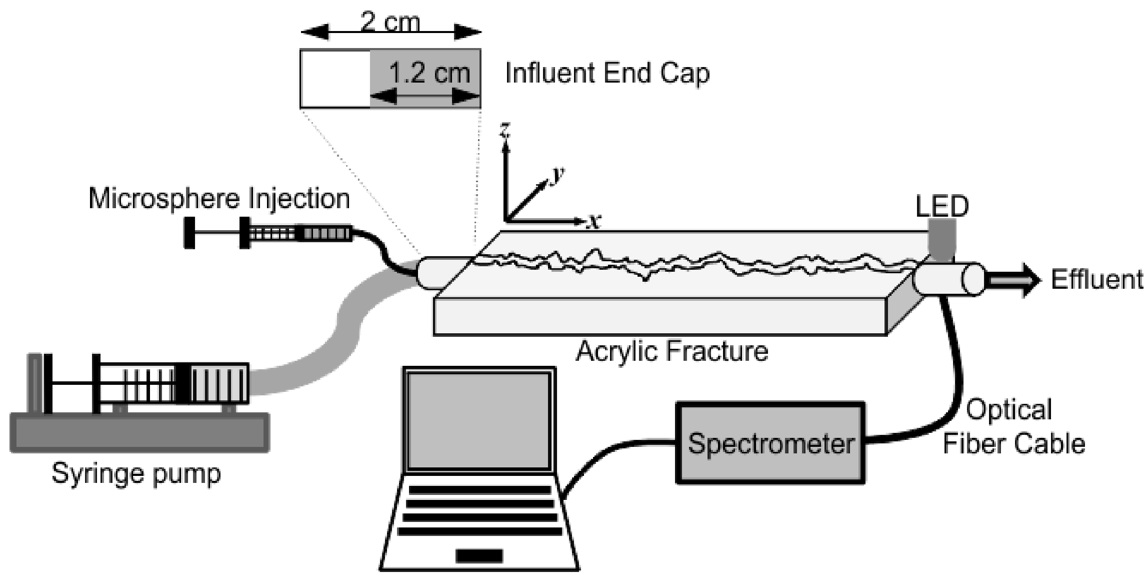

Figure 4.1: Schematic of the experimental setup showing the PMMA fracture, microsphere injection site, and the optical fiber cable allowing for the measurement of microsphere concentrations using a spectrometer. Microsphere injection in the influent end cap is shown. The z axis of the fracture is invariant (aperture of 2.3 mm) in the sense that there is no aperture variation along this axis. The variation in the fracture is in the xy plane (the length of the fracture being measured along the x axis), thus producing a quasi-three dimensional fracture.

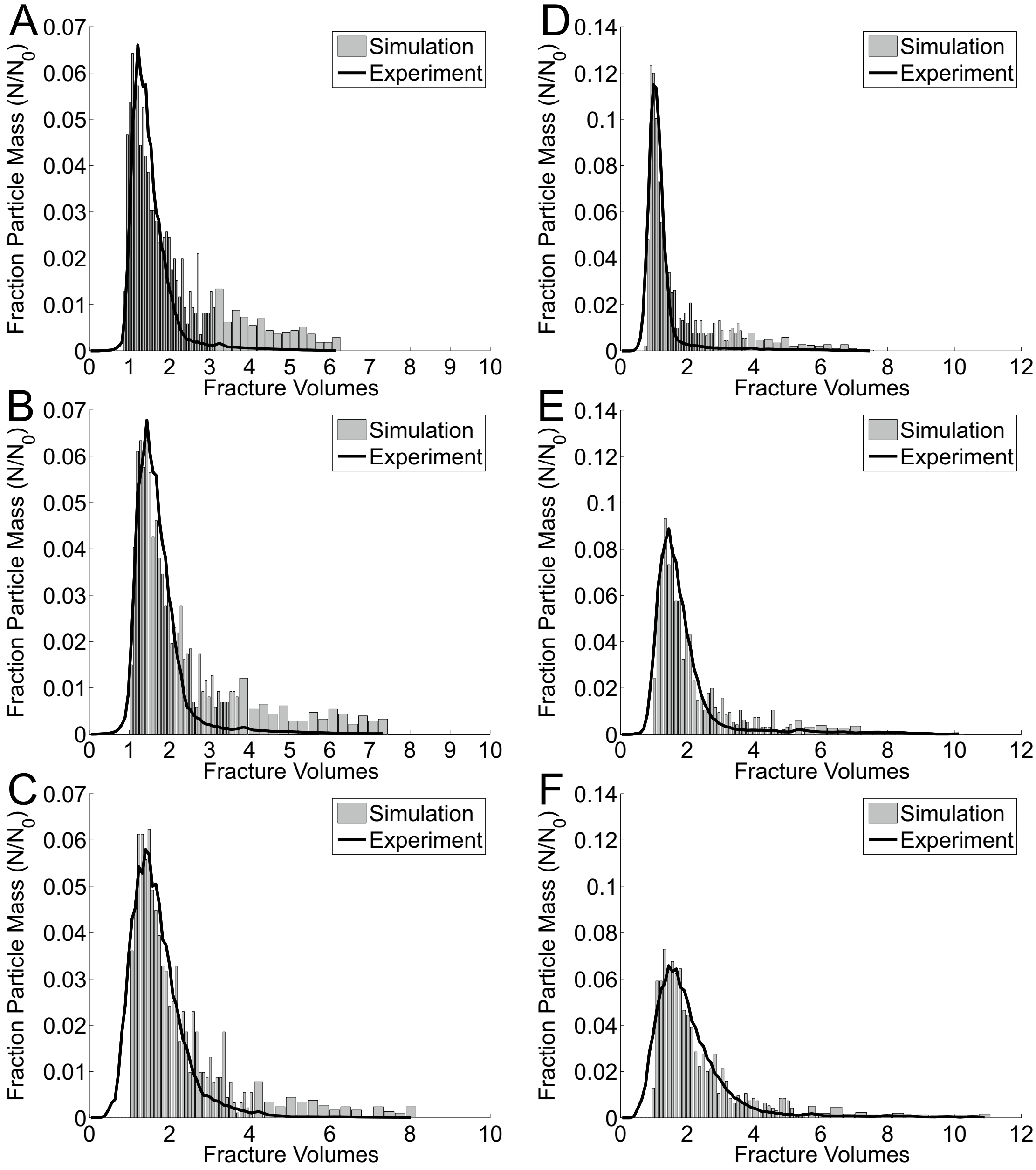

Figure 4.2: 0.046 μm breakthrough curves for both experiment and optimized simulation. N represents mass at the given fracture volume, N_0 represents total injected mass. A) Fracture 1 at 2.6 m/day; B) Fracture 1 at 26 m/day; C) Fracture 1 at 114 m/day; D) Fracture 2 at 2.6 m/day; E) Fracture 2 at 26 m/day; F) Fracture 2 at 114 m/day.

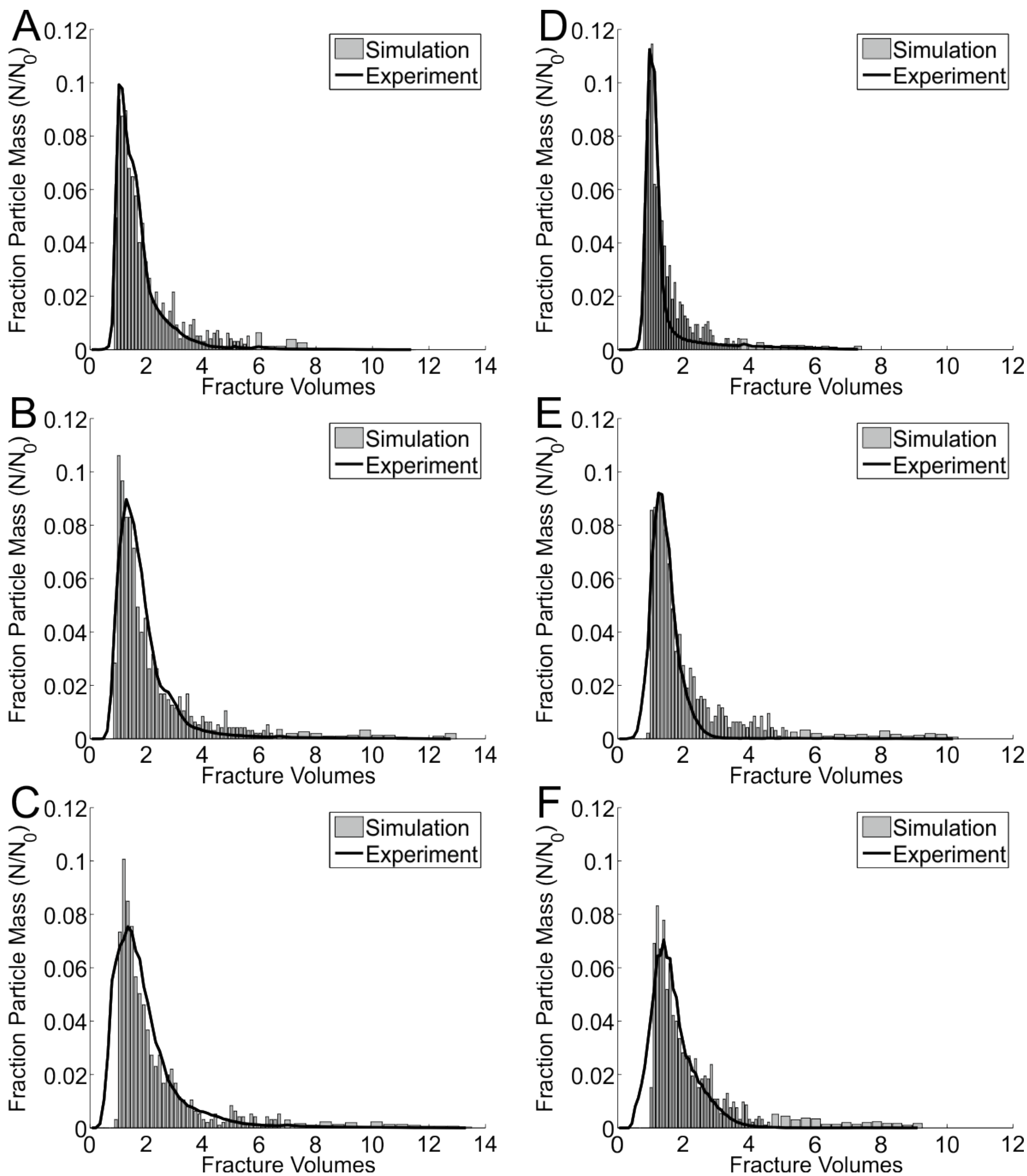

Figure 4.3: 0.55 μm breakthrough curves for both experiment and optimized simulation. N represents mass at the given fracture volume, N_0 represents total injected mass. A) Fracture 1 at 2.6 m/day; B) Fracture 1 at 26 m/day; C) Fracture 1 at 114 m/day; D) Fracture 2 at 2.6 m/day; E) Fracture 2 at 26 m/day; F) Fracture 2 at 114 m/day.

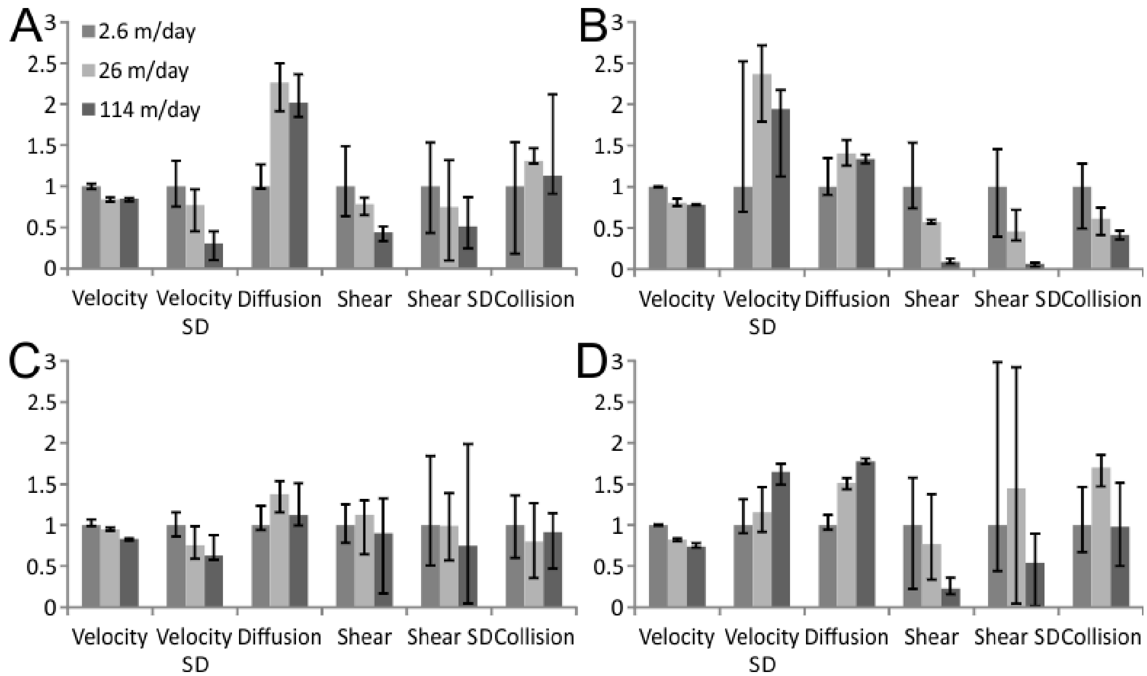

Figure 4.4: Parameter median (bar) and total range (error bars) of the top 10 most accurate simulations at each flow rate. Each parameter is set relative to the 2.6 m/day value for each parameter for comparison, with the parameters for the 2.6 m/day medians being set to 1. A) 0.046 μm microspheres in Fracture 1; B) 0.046 μm microspheres in Fracture 2; C) 0.55 μm microspheres in Fracture 1; D) 0.55 μm microspheres in Fracture 2.

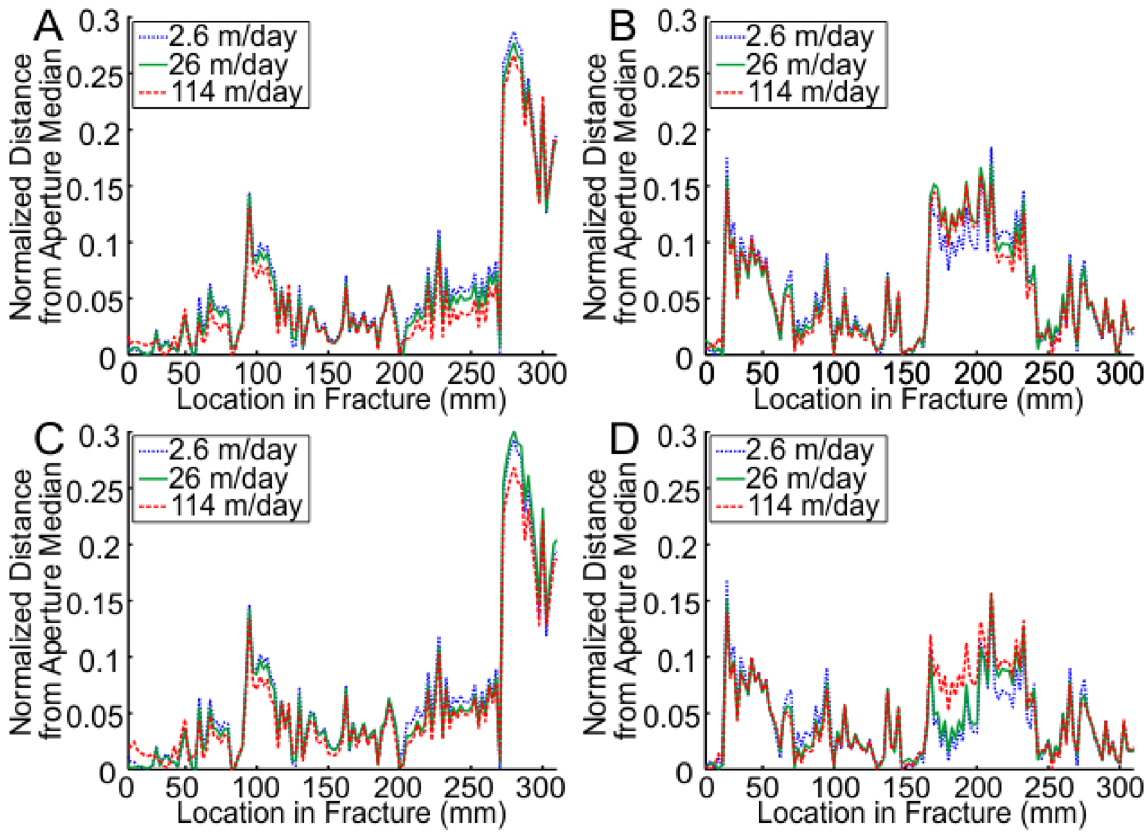

Figure 4.5: A plot of the mean normalized distance of particles from the aperture median line along the length of the fracture (x axis) in the xy plane at each flow rate. All distances are normalized to the local aperture (xy plane). A) 0.046 μm microspheres in Fracture 1; B) 0.046 μm microspheres in Fracture 2; C) 0.55 μm microspheres in Fracture 1; D) 0.55 μm microspheres in Fracture 2.

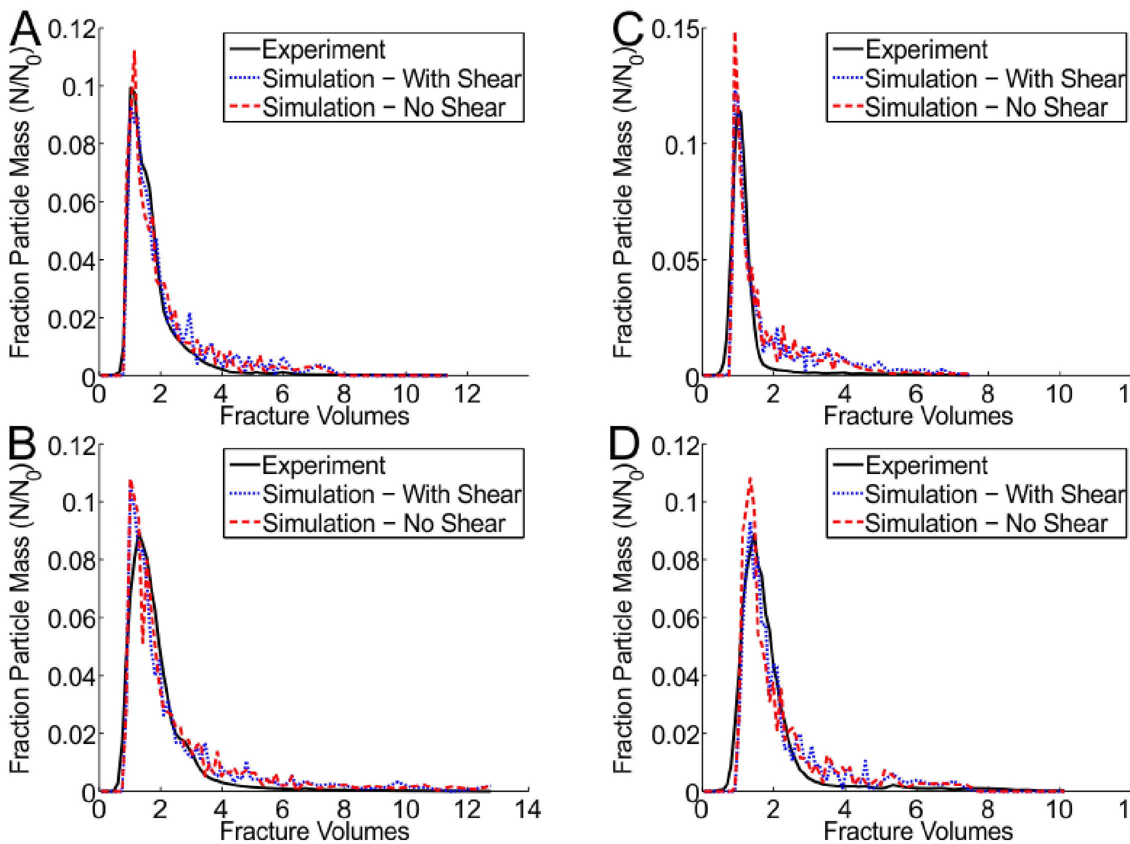

Figure 4.6: Breakthrough curve examples with experiment, optimized simulation and simulation neglecting shear. A) 0.55 μm microspheres at 2.6 m/day in Fracture 1; B) 0.55 μm microspheres at 26 m/day in Fracture 1; C) 0.046 μm microspheres at 2.6 m/day in Fracture 2; D) 0.046 μm microspheres at 26 m/day in Fracture 2.

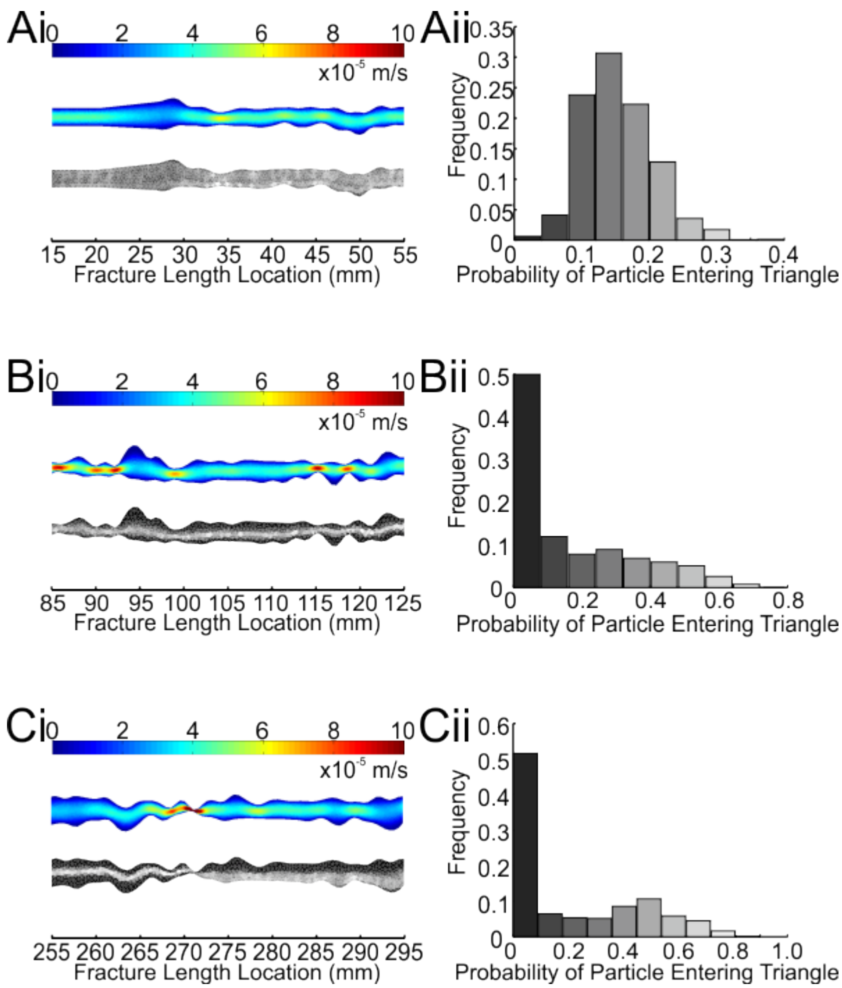

Figure 4.7: Each fracture region was discretized into approximately 1500 triangles in order to compute the probability of a 0.55 μm particle encountering a given triangular region in fracture 1 at 2.6 m/day. A) The fracture region from 15 mm to 55 mm where the initial particle release occurs from 10 mm to 22.5 mm. The flow velocity is shown in colour and the probability of a particle entering a triangular region is shown from 0 (black) to 0.4 (white). B) The histogram of probabilities from part A with bars colour coded to the probabilities. C) The fracture region from 85 mm to 125 mm. The flow velocity is shown in colour and the probability of a particle entering a triangular region is shown from 0 (black) to 0.8 (white). D) The histogram of probabilities from part C with bars colour coded to the probabilities. E) The fracture region from 255 mm to 295 mm. The flow velocity is shown in colour and the probability of a particle entering a triangular region is shown from 0 (black) to 1.0 (white). F) The histogram of probabilities from part E with bars colour coded to the probabilities.

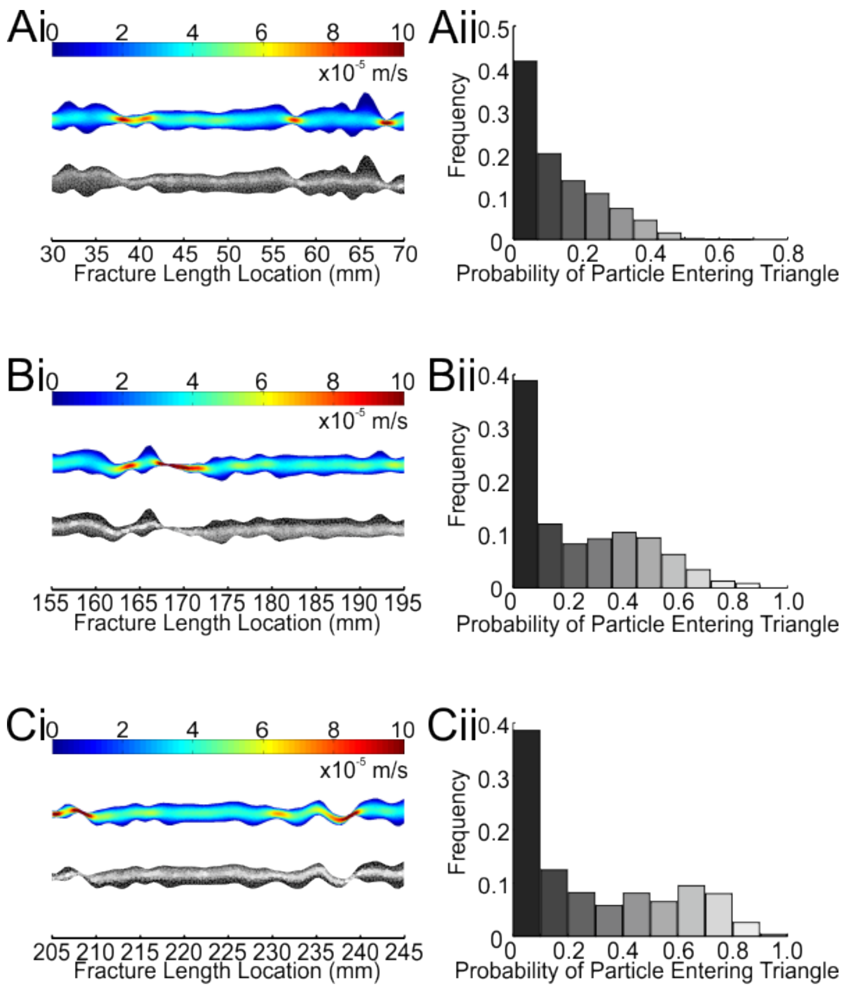

Figure 4.8: Each fracture region was discretized into approximately 1500 triangles in order to compute the probability of a 0.046 μm particle encountering a given triangular region in fracture 2 at 2.6 m/day. A) The fracture region from 30 mm to 70 mm where the initial particle release occurs from 10 mm to 22.5 mm. The flow velocity is shown in colour and the probability of a particle entering a triangular region is shown from 0 (black) to 0.8 (white). B) The histogram of probabilities from part A with bars colour coded to the probabilities. C) The fracture region from 155 mm to 195 mm. The flow velocity is shown in colour and the probability of a particle entering a triangular region is shown from 0 (black) to 1.0 (white). D) The histogram of probabilities from part C with bars colour coded to the probabilities. E) The fracture region from 205 mm to 245 mm. The flow velocity is shown in colour and the probability of a particle entering a triangular region is shown from 0 (black) to 1.0 (white). F) The histogram of probabilities from part E with bars colour coded to the probabilities.

Chapter 5

Conclusions and Recommendations

5.1 Conclusions

The overall goal of this research was to develop an understanding of how the geometry of a fracture influences the transport of two types of contaminants, dense non-aqueous phase liquids (e.g. tetrachloroethylene, trichloroethylene, creosote, and heavy crude) and particles or colloids (e.g. viruses, bacteria, and parasites). The following conclusions can be drawn from the research contained herein:

- The optimization of the parameters of an IP model of DNAPL invasion into a horizontal, saturated, variable aperture fracture in comparison to experiment is possible and helps to elucidate upon the different physical effects at work during DNAPL invasion. This work showed the effects of gravity and pressure during the invasion process (Chapter 2).

- In horizontal, saturated, variable aperture fractures, gravity is an important factor in discerning the invasion pattern associated with DNAPL entry and movement in the fracture. The effect of gravity on the invasion pattern is entirely related to the undulous nature of a fracture as measured by the mid-aperture plane. Even when the pressure values observed in the invasion process are two orders of magnitude greater than the effects of gravity, gravity is still important in producing an accurate invasion pattern for the experimental fracture. Furthermore, an equation was developed based on simulated fractures and different DNAPLs estimating the minimum and maximum differences between simulations including and neglecting gravity (the conventional model)(Chapter 2).

- Fracture orientation has little effect on the entrapped fraction of DNAPL in fractures with a COV greater than 0.1. This condition suggests a relatively high level of roughness in the fracture. As COV increases, so does the likelihood of a preferential flow path allowing water to exit the fracture without imbibing much DNAPL. Furthermore, only sub-horizontal fractures permit the near complete or complete removal of DNAPL in fractures initially saturated by DNAPL. At fracture angles of -15° and greater, the potential for complete imbibition tends to zero as the gravitational forces aiding the imbibition process are no longer able to overcome the local geometries in the fracture field (Chapter 3).

- It was possible to generate equations estimating the minimum and maximum volumetric fraction of DNAPL entrapped after flushing with water for fractures angled at 0° and -15°. As horizontal and super-horizontal fractures (angle $\geq 0°$) tended to behave in a similar fashion, the equations developed for the horizontal fracture may be used to estimate a minimum and maximum fraction of entrapped DNAPL. Similarly, the equations developed for the -15° fractures may be used to estimate the volumetric fraction of DNAPL entrapped for all sub-horizontal fractures with angles $\leq -15°$ (Chapter 3).

- It is possible to optimize parameters in an RWPT model and use the calibrated model to elucidate upon physical processes at work during particle transport in fractures. Calibrated RWPT simulations showed that particles do not move at the velocity of the fluid contrary to all other literature using standard RWPT. As well, it was shown that fluid shear has an appreciable effect on the dispersion of the contaminants in the effluent despite being less than 1% of the particle movement vector. Simulations were shown to be most robust at slower groundwater speeds (e.g. 2.6 m/day)(Chapter 4).

- Naturally, the geometry of the fracture induces the fluid flow field generated by numerically solving the Navier-Stokes equations; however, the effect that the geometry has on particles suggests that particles being transported may not encounter certain regions of the fracture. Ultimately, this geometric randomness can have a striking effect on the BTCs, as evidenced by differences in experimental BTCs between two fractures with very similar statistics. In particular, the experimental results show remarkable differences in dispersion and peak contamination concentrations between the two fractures for both microsphere sizes. These observations are mirrored by the simulations as particles may only experience certain regions in of the flow field (Chapter 4).

- The work contained in this thesis shows that the local geometry of the fracture was vital in determining the path of contaminants. During DNAPL invasion in a horizontal water saturated fracture, gravity can significantly influence the pattern of invasion (Chapter 2). During the process of water invading a DNAPL saturated fracture, fracture geometry and angle have a great influence on the amount of DNAPL retained in the fracture (Chapter 3). In particle transport, the local geometry affects the flow field and, in turn, the particle path taken during transport (Chapter 4). While these are two fundamentally different contaminants (DNAPLs and particles), fracture geometry plays a critical role in how these contaminants are transported in fractures.

5.2 Contributions

This thesis consists of work elucidating on physical effects on the transport of contaminants derived from the geometry of variable aperture fractures. The studies references herein provided several unique contributions to the body of research surrounding hydrologic modelling in fractured media.

- This is the first study to include gravity in simulations determining the invasion pattern of DNAPLs in saturated horizontal fractures and compare simulation results to experimental work. This work showed the importance of gravity in determining the final invasion pattern of DNAPL. As well, equations were developed based on these simulations to help determine when gravity will be a factor in a fracture based on fracture statistics and DNAPL characteristics (Chapter 2).

- The DNAPL invasion model presented here marks the first time a DNAPL invasion IP model in fractures was initialized with parameters and optimized to experimental results, in particular using a genetic algorithm (Chapter 2).

- This work is the first to study angled fractures with regards to DNAPL entrapment. As well, this research led to the conclusion that while angle matters in the entrapment of DNAPL after flushing by water, the main differences occur as the angle changes from -10° to -15°, where gravity begins to sufficiently aid in imbibition and permit significantly larger quantities of DNAPL to be flushed (Chapter 3).

- The RWPT model used in this work was the first to include the effects of fluid shear on particles during transport and shows that shear has a small but appreciable effect on BTCs by increasing dispersion. This effect is noticeable in 30 cm fractures, and thus would be much more appreciable at the field scale (Chapter 4).

- The RWPT model coupled with the Navier-Stokes based flow field (based on the geometry of the fracture) marks the first time not only parameters have been added to an RWPT model, but also the first time the parameters of a RWPT model were optimized to experimental results. This calibration led to the observation that drag, as scaled by the velocity coefficient, α_{mean}, is much greater than is used in all other literature utilizing RWPT. This measurement effectively shows that particles do not travel at the same speed as the fluid (Chapter 4).

- Particles were shown to only sample certain regions of a fracture during transport, effectively only presenting the particles with one or no fracture walls for adhesion. As well, there were times when the particles were forced into the middle half of the fracture where fluid flow is fastest. This observation shows that the peak concentration of particles may exit a fracture much sooner and with higher concentration than expected from the traditional parallel plate model often used in research (Chapter 4).

- In all three papers, cluster computing was heavily relied upon for simulations. In two of the three studies conducted (Chapters 2 and 4), cluster computing was utilized for model optimization. Optimization is infrequently performed in small scale transport modelling in fractured and porous media as the computational overhead is expensive. Cluster computing was a necessity in the optimization/calibration of the contaminant transport models as the computation time on a personal computer would have exceeded tens of years.

5.3 Recommendations for Future Work

- Chapter 3 included a simulations based approach to generate equations describing the fraction DNAPL retained in a fracture post flushing. A similar approach may be taken to the invasion of DNAPL leading to dissolved DNAPL in water. Once the pattern has been defined, the surface area of DNAPL in contact with flowing water could be calculated and the concentration of dissolved DNAPL could be estimated. The use of cluster computing would allow for analysis of thousands of iterations of fractures and invasion processes, estimates of dissolved DNAPL that would be found in the effluent of a given fracture can be estimated, likely within a range.

- Another important question that arises when studying single fractures is happens to DNAPL invasion or imbibition at the interface of two or more fractures.

Experimental work is needed to elucidate upon the physics involved in this process especially given the results of the simulations regarding entrapped DNAPL and the angles of fractures. Furthermore, if an understanding of the DNAPL interface physics can be effectively modelled, then the data generated from numerous simulations may also reveal some statistically significant patterns. Ultimately, if a fracture network is generated, it may be possible to assign DNAPL invasion or entrapment values to fractures in the system in the direction of flow based on data generated from the previous studies, thus leading toward a conceptual model of risk in fractured bedrock.

- The RWPT/Navier-Stokes algorithm may be extended to fully realized three dimensional fractures. Inclusion of additional effects such as adhesion and release of particles on the RWPT algorithm or matrix flow on the flow field would be of significant value (matrix flow negates the typical no-slip boundary condition typically used as fluid may flow in or out of a fracture in various regions depending on the matrix properties). Ultimately, this more physically tuned system could then be compared with experimental fractures and optimized for given contaminants. As well, future efforts attempting to combine multiple fractures in a network are needed to bring this laboratory scale model to the field.

Chapter 6

Appendices

6.1 Physics of Invasion Percolation in Fractures

Invasion percolation was utilized in Chapter 2 and 3 in order to model the invasion of a water saturated fracture by DNAPL (Chapter 2) or the invasion of a DNAPL saturated fracture by water (Chapter 3). The process of a non-wetting fluid (DNAPL) invading a wetting fluid (water) saturated fracture is known as drainage. Modelling drainage is rooted in the non-wetting fluid (or invading fluid) overcoming the entry pressure required to displace water in the fracture. Traditionally, the view of drainage is shown in Figure 6.1. A DNAPL pool is situated above a fracture with a height (measured to the middle of the fracture), h, and density ρ_{nw} (nw for non-wetting). The fracture is a parallel plate and is saturated with water (wetting). The fracture aperture is given by b and the density of water is ρ_w. The interfacial tension between the wetting and non-wetting fluid is given by σ and the wetting angle or contact angle of the wetting fluid and non-wetting fluid interface against the fracture medium is given by θ (where $\theta \in [0°, 90°]$).

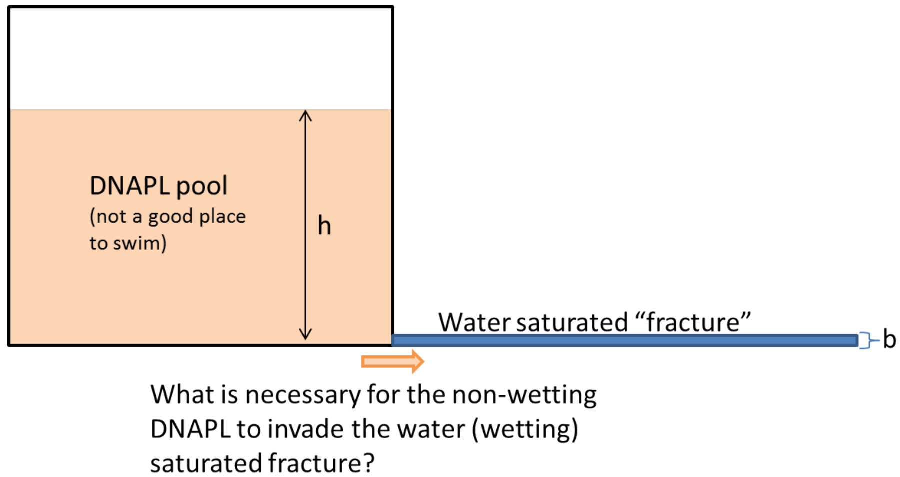

Figure 6.1: A pictorial view of drainage. A pool of DNAPL with a given height (h) above the fracture may induce DNAPL migration into the fracture if the head is large enough to ensure that DNAPL pressure can overcome the entry pressure into the fracture.

In this model of drainage, the fracture is seen as a parallel plate (Figure 6.1) and thus the entry pressure, P_{entry}, resisting invasion is based purely on capillarity and given by the solution to the Young-Laplace equation (a value that is always positive) (Singhal and Gupta, 2011):

$$P_{entry} = \frac{2\sigma\cos\theta}{b} \tag{6.1}$$

Since the DNAPL has a pressure head induced by the height above the fracture, we can compute the pressure acting to move the DNAPL into the fracture, P_{IN}(Singhal and Gupta, 2011):

$$P_{IN} = (\rho_{nw} - \rho_w)\, gh \tag{6.2}$$

where g is the gravitational constant. **Drainage occurs (namely, DNAPL invades the fracture) if P_{IN} exceeds P_{entry}.**

In the invasion percolation modelling of drainage, a fracture is modelled as a set of elements in a grid pattern of a given size (length and width), aperture (height), and median aperture value (a z value which is used to measure undulations in the fracture) (Figure 6.2A). With this in mind, the entry pressure for a water saturated element must be computed using both capillarity and a gravitational component, $P_{IPentry}$:

$$P_{IPentry} = \frac{\alpha\sigma\cos\theta}{b} + (\rho_{nw} - \rho_w)\, g\, (z_2 - z_1) \tag{6.3}$$

where α is a parameter ($\alpha = 2$ in the case of P_{entry} in the previous DNAPL pool example). Assuming that $\Delta\rho = (\rho_{nw} - \rho_w)$ and $\Delta z = (z_2 - z_1)$, then it is possible to analyze the effects of the additional gravitational component. In this case, $\Delta\rho$ is always positive because the density of the DNAPL is greater than water (by definition). In the case where the possible DNAPL invasion element is lower than the DNAPL element (Figure 6.2B), then this lower height will promote DNAPL invasion and accordingly, $\Delta z < 0$ which subtracts from the capillarity component of $P_{IPentry}$, effectively lowering the entry pressure and aiding invasion. If the water saturated element is situated above the DNAPL element (Figure 6.2C), then this should help to inhibit invasion. In Equation 6.3, $\Delta z > 0$ and thus the gravitational component adds to the entry pressure making it larger. Invasion percolation modelling drainage proceeds along the elements of lowest entry pressures; however, it must be ensured that invasion only occurs when the head inducing invasion is great enough to exceed the entry pressure. In studies utilizing IP, the entry pressure given above is typically generalized to invasion pressure or total invasion pressure. In the studies conducted herein, the simulations were assumed to be under laboratory conditions in which a high enough head is always available to drive the DNAPL to invade the fracture until it exits the opposite fracture side.

Imbibition occurs when a wetting fluid (water) invades a fracture saturated with a non-wetting fluid (DNAPL) and can also be modelled using IP. In this instance, the invasion pressure must be computed using the essentially the same equation but the terms are modified. The first modification is that the contact or wetting angle is now measured from the DNAPL side, and hence $\theta \in [90°, 180°]$. Thus, the invasion pressure or terminal pressure (specific to imbibition), P_{IPterm} is given by:

$$P_{IPterm} = \frac{\alpha\sigma\cos\theta}{b} + (\rho_w - \rho_{nw})\, g\, (z_2 - z_1) \tag{6.4}$$

In the case of imbibition, the cosine term is negative. The wetting fluid will tend to the smallest apertures, or when the capillarity term is smallest (or "most negative"). This capillarity term is then modified by a gravity term in which the DNAPL will tend to migrate towards lower elevations. Note that in equation 6.4, the $\Delta\rho$ term is negative as the order of wetting and non-wetting densities has switched. If water (at elevation z_1) is invading a site at a higher elevation (z_2), then the gravity term is negative because $z_2 > z_1$. This negative value is then subtracted from the already negative capillarity term, and P_{IPterm} is driven further into the negative. Since the IP model selects the lowest pressures, this lower term is more likely to be selected for invasion. Similarly, if water is attempting to invade a site at a lower elevation, then the gravity term is positive thus making it less likely that water will invade the site.

6.2 RWPT Model Verification

Verification of the Random Walk Particle Tracking (RWPT) code utilized in the Chapter 4 study was undertaken by comparing the breakthrough results of a simulation performed by Zheng *et al.* (2009a) to results of the code used herein under the same experimental conditions. The Zheng *et al.* (2009a) experimental conditions instantaneously introduced 10000 0.5 μm spherical colloids at the beginning of a 16 m long by 2 m wide parallel plate fracture with aperture of 300 μm. The flow in the fracture was set to 98.5 m/day in the direction of the 16 m long axis). Zheng *et al.* (2009a) also compared their RWPT breakthrough to an analytical solution to the 1D Advection-Dispersion equation with instantaneous introduction of colloids. The Advection-Dispersion equation is given by (Kreft and Zuber, 1978):

$$\tfrac{\partial C}{\partial t} = D_L \tfrac{\partial^2 C}{\partial x^2} - v \tfrac{\partial C}{\partial x} \tag{6.5}$$

$$C\left(0, t\right) = \tfrac{M}{Q} \delta\left(t\right) \tag{6.6}$$

$$C\left(x, 0\right) = 0, x > 0 \tag{6.7}$$

$$\lim_{x \to \infty} C\left(x, t\right) = 0 \tag{6.8}$$

where $C(x,t)$ $[ML^{-3}]$ is the concentration of colloids at position, x $[L]$, and time, t $[T]$, v $[MT^{-1}]$ is the mean transport velocity, D_L $[L^2T^{-1}]$ is the longitudinal dispersion coefficient, M $[M]$ is the mass of colloid injected, Q $[L^3T^{-1}]$ is the volumetric flow rate, and $\delta(t)$ is the Dirac delta function. The analytical 1D solution to equation 6.5 is given by the following equation Kreft and Zuber (1978):

$$C(x,t) = \frac{M}{Q} \frac{x}{sqrt 4 \pi D_L t} \exp\left(-\frac{\left(x - vt\right)^2}{4 D_L t}\right) \tag{6.9}$$

where v was approximately equal to the mean flow velocity. Zheng *et al.* (2009a) found that the analytical solution to the 1D Advection-Dispersion equation did not adequately model colloid transport (Figure 6.3 a) and was not used for RWPT model (Chapter 4) verification. The comparison of the RWPT simulation used in Chapter 4 was in very good agreement with the RWPT results demonstrated by Zheng *et al.* (2009a) and thus the model was assumed to be operating appropriately, hence verified.

6.3 RWPT Experimental Setup

In addition to the experimental schematic shown in Chapter 4, Figure 4.1, photographs of the experimental setup were taken to elucidate upon the experimental process. All experiments were performed in a dark box to eliminate extraneous light sources from influencing LED intensity collection.

Both fracture 1 and 2 were laser cut into poly(methyl methacrylate) (PMMA) and were 30 cm in length. The variation in both fractures was in the xy plane; however, along the z-axis (out of the page) the fracture aperture field was invariant (Figure 6.4).

Flow was induced at the inlet using a syringe pump with all effluent fluid being timed and captured for volumetric flow rate monitoring. The outlet end cap housed an LED and an optical fiber used to collect intensity information to monitor microsphere concentration in the effluent fluid (Figure 6.5).

The fractures were sealed near the fracture by dissolving the PMMA locally with dichloromethane and adhering a PMMA cover. Additional sealing around the perimeter of the two PMMA halves was added by sealing with epoxy. The housing for the LED and optical fiber was created out of a circular piece of plastic and all pieces were epoxied in place to prevent movement during experimentation (Figure 6.6).

In order to model these experiments, the 2D fracture geometry was imported into COMSOL multiphysics in order to numerically solve the Navier-Stokes equations of flow for the 2D fracture. Attempts to solve the Navier-Stokes equations for the three dimensional fracture geometry were unsuccessful. Boundary conditions used in the numerical solver were a no slip condition ($v = 0$) on the walls of the fracture and a pressure difference between the inlet and outlet to induce flow (these pressure differences are given with respect to flow in Chapter 4).

The flow field for the fracture was 2 dimensional, but for the purposes of attaining a more appropriate 3D flow field, a parabolic weighting function was utilized in the xz-plane. The parabolic weighting function was used scale the average 2D flow field depending on the z-value of the particle (Figure 6.8).

6.4 Concentration Curves used in the RWPT Experiments

Concentration curves were developed for each of the microsphere sizes (0.046 μm and 0.55 μm) and each fracture (Fracture 1 and 2). Each fracture required a unique concentration curve because the end caps and LEDs were unique to the fractures. Unused data appeared in each of the concentration curves (dented with X's) when absorbance was indistinguishable from 0 (namely, the intensity of light was indistinguishable from background values). Absorbance was calculated using the following formula:

$$A = -\ln\left(\frac{I}{I_0}\right) \tag{6.10}$$

where I is the intensity of light measured through a given concentration of microspheres and I_0 is the background light intensity (no microspheres in the water-Triton solution).

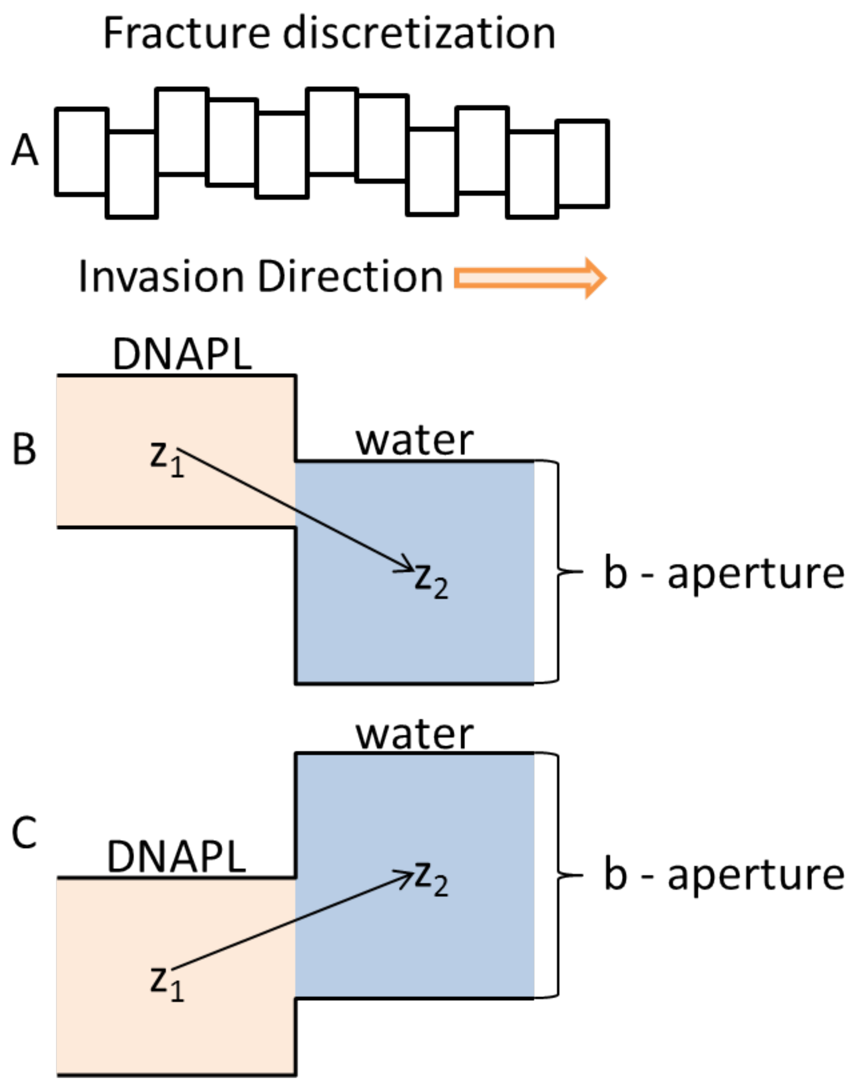

Figure 6.2: A) In a computer, the fracture is discretized as a set of apertures with heights associated with the median of the aperture being variable. When DNAPL is invading a water saturated fracture, from one DNAPL saturated element can potentially invade the adjacent water saturated element with two cases, either: B) the DNAPL is attempting to invade downwards into the water saturated element; or C) the DNAPL is attempting to invade upwards into the water saturated element.

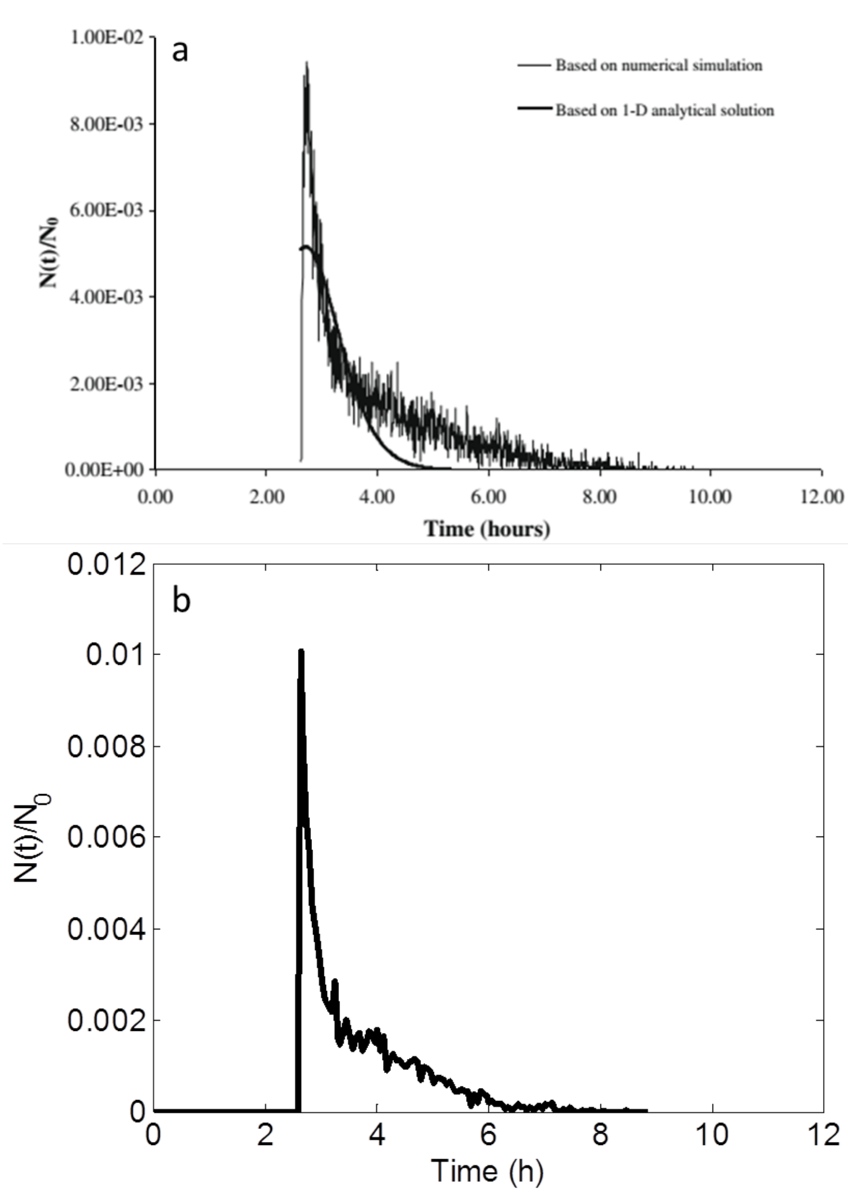

Figure 6.3: a) Breakthrough curve of RWPT and equation 6.9 demonstrated by Zheng *et al.* (2009a) (figure modified from (Zheng *et al.*, 2009a) b) Breakthrough curve of the Chapter 4 RWPT simulation for the same experiment as (Zheng *et al.*, 2009a)

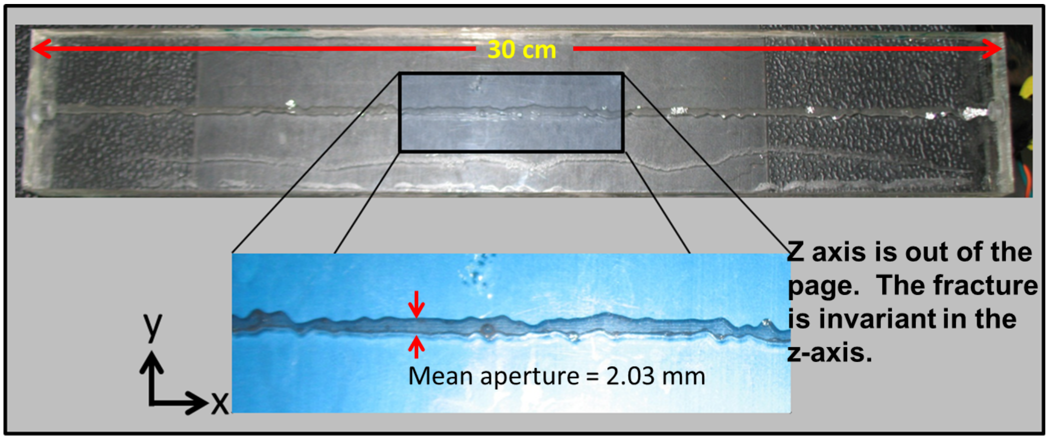

Figure 6.4: An example fracture with variation in the xy-plane is shown with no variation along the z-axis.

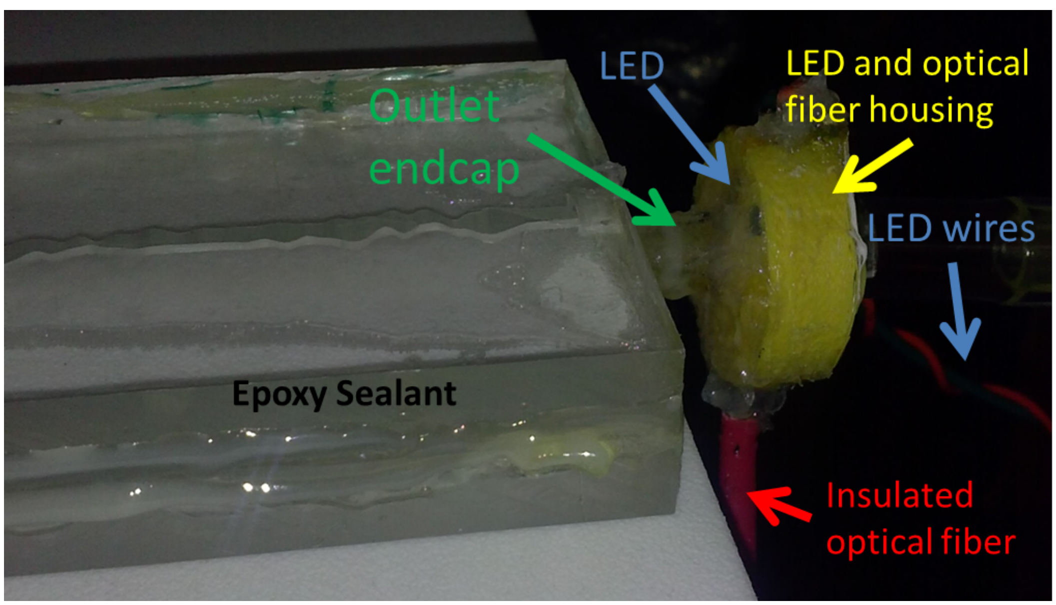

Figure 6.5: An experimental fracture with the inlet end cap and outlet end cap. The LED housing, LED wires, and optical fiber can be seen.

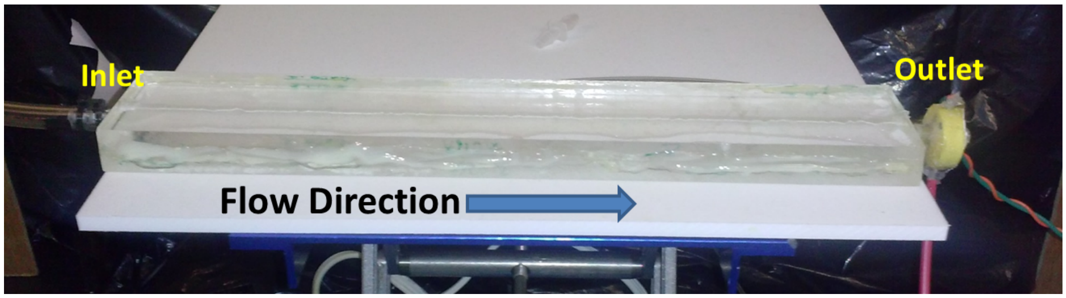

Figure 6.6: The LED and optical fiber housing on the effluent end cap of the fracture is shown.

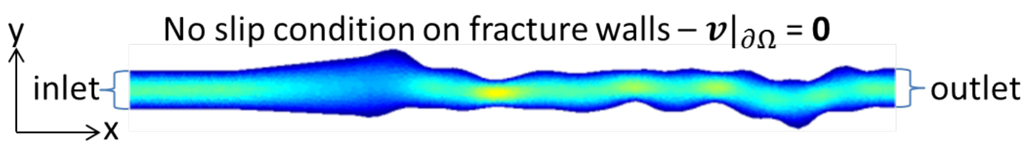

Figure 6.7: A section of Fracture 1 showing the solved flow field demonstrating the no slip condition along the fracture walls. A pressure difference between the inlet and outlet was used to induce flow in the model.

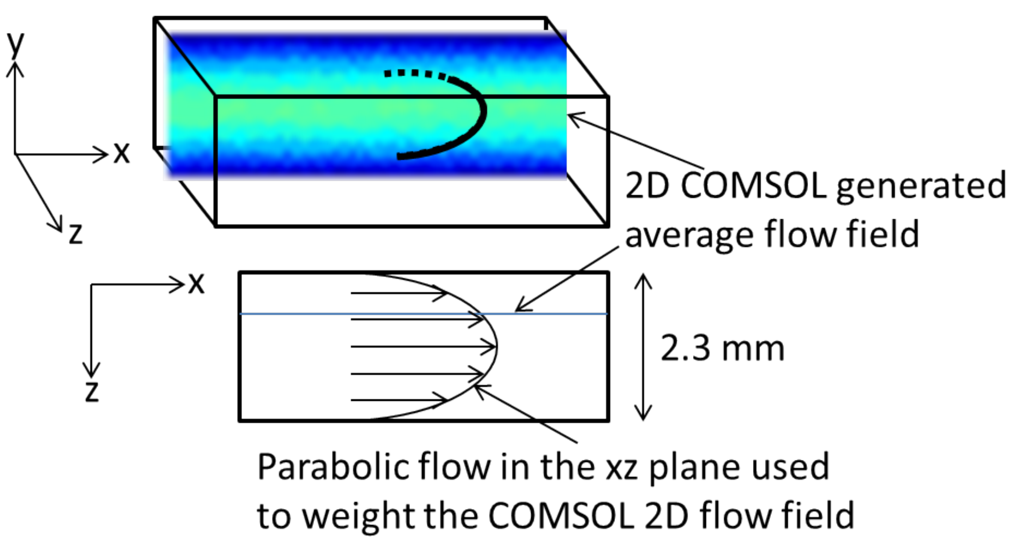

Figure 6.8: A schematic of how the 2D COMSOL generated flow field was scaled using a parabolic weighting function to generate a 3D flow field.

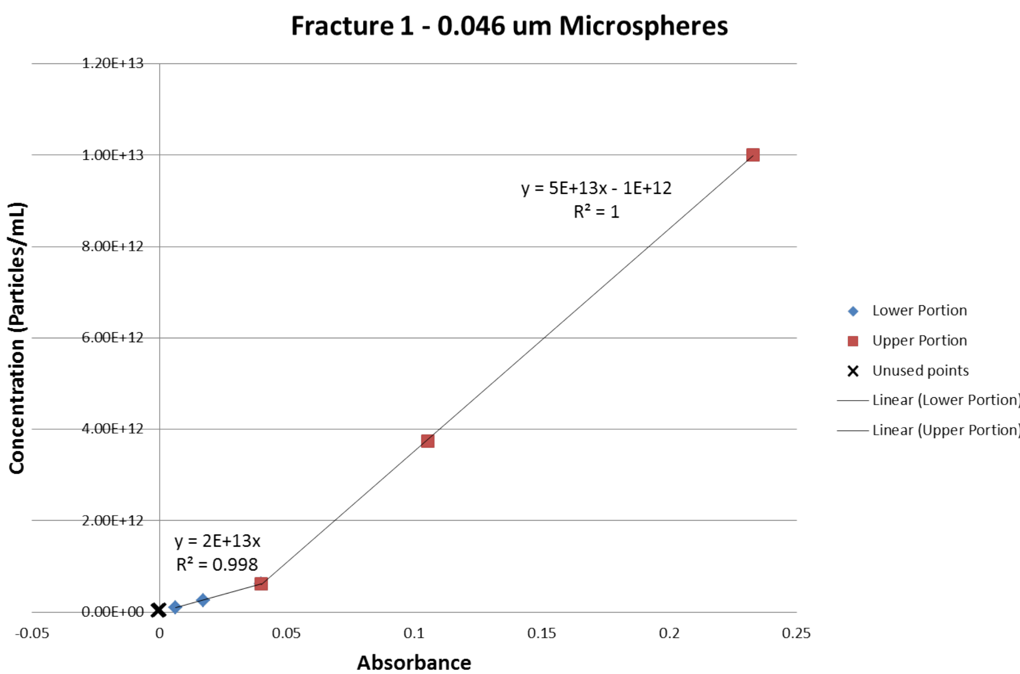

Figure 6.9: The concentration curve for Fracture 1 with 0.046 μm microspheres. X denotes data unused in the development of the concentration curve as the absorbance values were indistinguishable from 0.

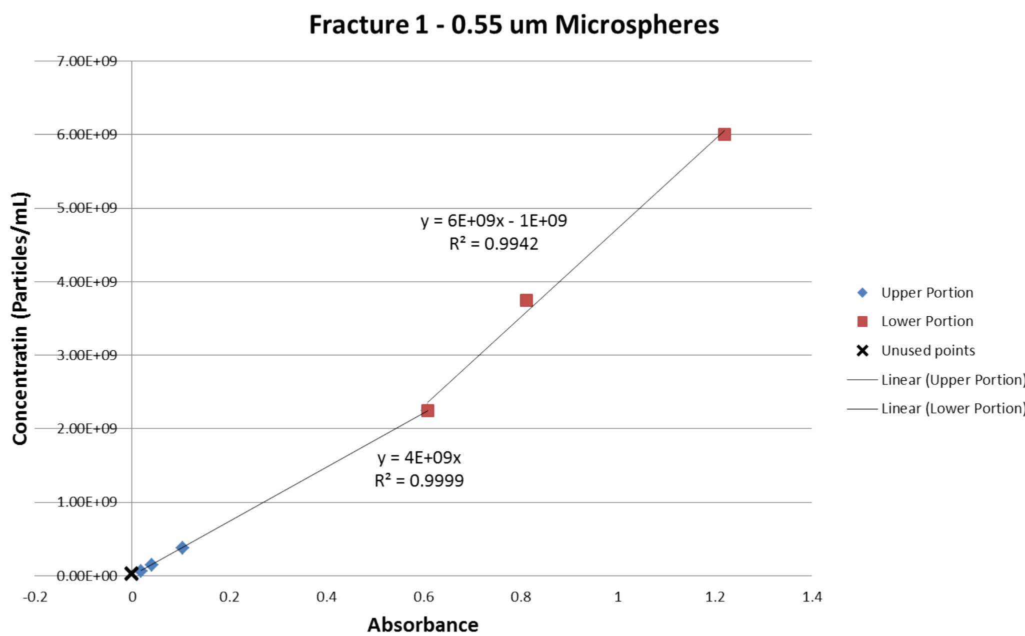

Figure 6.10: The concentration curve for Fracture 1 with 0.55 μm microspheres. X denotes data unused in the development of the concentration curve as the absorbance values were indistinguishable from 0.

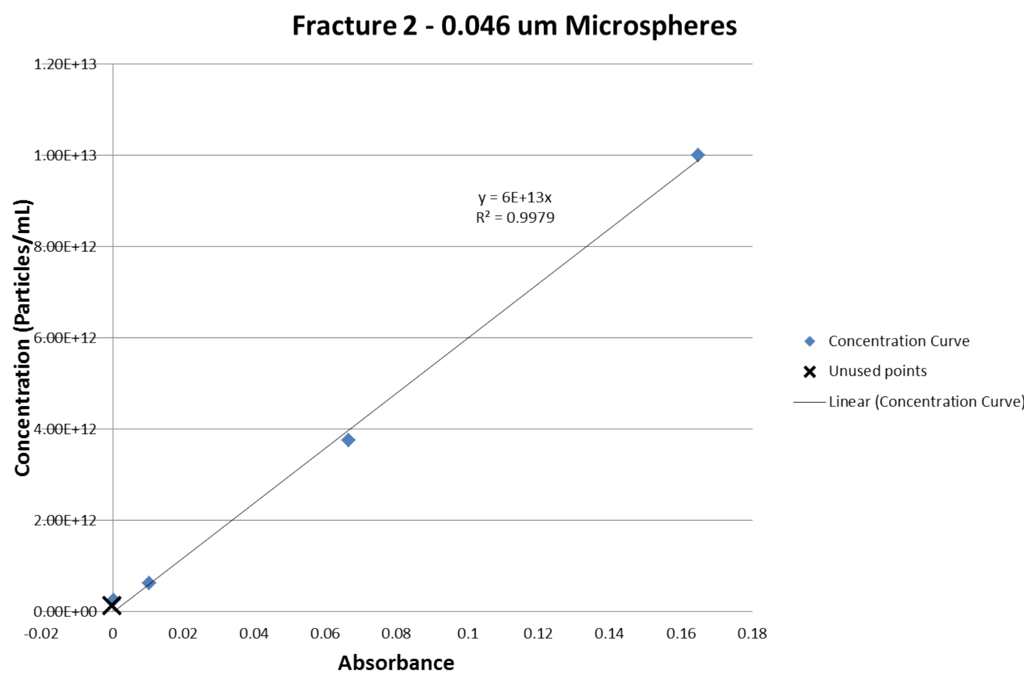

Figure 6.11: The concentration curve for Fracture 2 with 0.046 μm microspheres. X denotes data unused in the development of the concentration curve as the absorbance values were indistinguishable from 0.

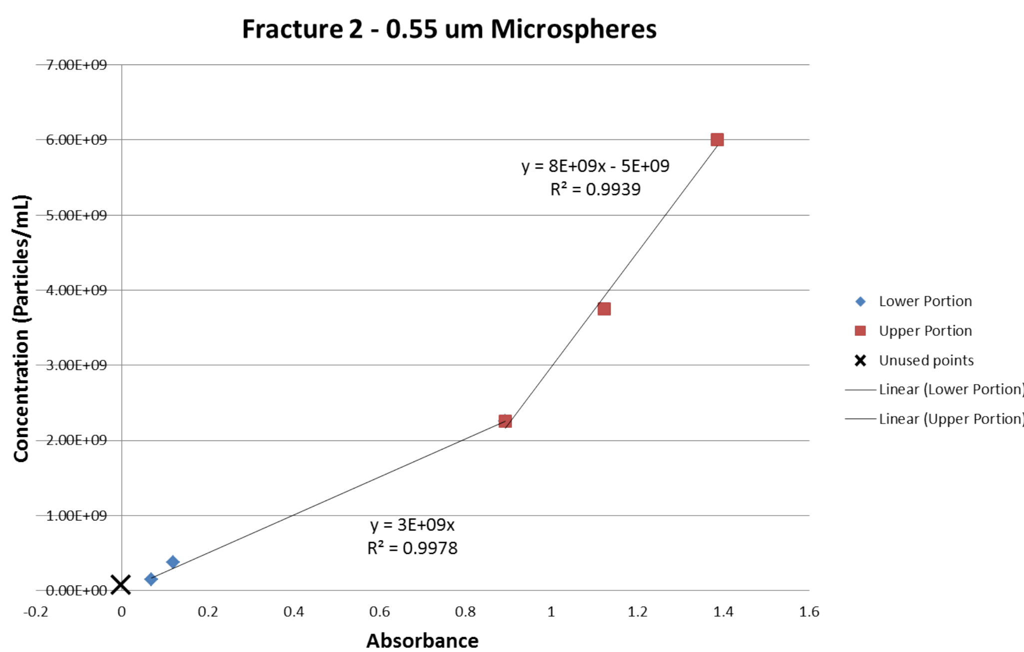

Figure 6.12: The concentration curve for Fracture 2 with 0.55 μm microspheres. X denotes data unused in the development of the concentration curve as the absorbance values were indistinguishable from 0.

Bibliography

Abdel-Salam, A. and Chrysikopoulos, C. V. (1995). Analysis of a model for contaminant transport in fractured media in the presence of colloids. *Journal of Hydrology*, **165**, 261–281.

Alexandra, R., Gerhard, J. I., and Kueper, B. H. (2012). Hydraulic displacement of dense nonaqueous phase liquids for source zone stabilization. *Ground Water*, **50**(5), 765–74.

Annable, M. D., Rao, P. S. C., Hatfield, K., Graham, W. D., Wood, A. L., and Enfield, C. G. (1998). Partitioning tracers for measuring residual napl: Field-scale test results. *Journal of Environmental Engineering*, **124**(6), 498–503.

Aris, R. (1956). On the dispersion of a solute in a fluid flowing through a tube. *Proceedings of the Royal Society A: Mathematical, Physical and Engineering Sciences*, **235**(1200), 67–77.

Bayoudh, S., Othmane, A., Mora, L., and Ben Ouada, H. (2009). Assessing bacterial adhesion using dlvo and xdlvo theories and the jet impingement technique. *Colloids Surf B Biointerfaces*, **73**(1), 1–9.

Bear, J. (1972). *Dynamics of Fluids in Porous Media*. Dover, New York, USA.

Berkowitz, B. (2002). Characterizing flow and transport in fractured geological media: A review. *Advances in Water Resources*, **25**(8-12), 861–884.

Berkowitz, B. and Scher, H. (1997). Anamalous transport in random fracture networks. *Physical Review Letters*, **79**(20), 4038–4041.

Bird, R. B., Stewart, W. E., and Lightfoot, E. N. (2002). *Transport Phenomena*. John Wiley and Sons, Inc., New York, New York, USA, 2 edition.

Boutt, D. F., Grasselli, G., Fredrich, J. T., Cook, B. K., and Williams, J. R. (2006). Trapping zones: The effect of fracture roughness on the directional anisotropy of fluid flow and colloid transport in a single fracture. *Geophysical Research Letters*, **33**(21).

Broadbent, S. R. and Hammersley, J. M. (1957). Percolation processes. *Mathematical Proceedings of the Cambridge Philosophical Society*, **53**(3), 629–641.

Brush, D. J. and Thomson, N. R. (2003). Fluid flow in synthetic rough-walled fractures: Navier-stokes, stokes and local cubic law simulations. *Water Resources Research*, **39**(4), 1085.

Cady, C., Silliman, S. E., and Shaffern, E. (1993). Variation in aperture estimate ratios from hydraulic and tracer tests in a single fracture. *Water Resources Research*, **29**(9), 2975–2982.

Cardenas, M. B., Slottke, D. T., Ketcham, R. A., and Sharp Jr., J. M. (2007). Navier-stokes flow and transport simulations using real fractures shows heavy tailing due to eddies. *Geophysical Research Letters*, **34**, L14404.

Chrysikopoulos, C. V. and James, S. C. (2003). Transport of neutrally buoyant and dense variably sized colloids in a two-dimensional fracture with anisotropic aperture. *Transport in Porous Media*, **51**(2), 191–210.

Cohen, R. M., Mercer, J. W., and Matthews, J. (1993). Dnapl site evaluation. Report, United States Environmental Protection Agency.

Corey, A. T. (1986). *Mechanics of immiscible fluids in porous media*. Water Resources Publications, Littleton, CO, USA.

Culligan, K. A., Wildenschild, D., Christensen, B. S. B., Gray, W. G., Rivers, M. L., and Tompson, A. F. B. (2004). Interfacial area measurements for unsaturated flow through a porous medium. *Water Resources Research*, **40**(12), n/a–n/a.

Culligan, K. A., Wildenschild, D., Christensen, B. S. B., Gray, W. G., and Rivers, M. L. (2006). Pore-scale characteristics of multiphase flow in porous media: A comparison of airwater and oilwater experiments. *Advances in Water Resources*, **29**(2), 227–238.

Darwish, M. I. M., McCray, J. E., Currie, P. K., and Zitha, P. L. J. (2003). Polymer-enhanced dnapl flushing from low-permeability media: An experimental study. *Ground Water and Remediation*, **23**(2), 92–101.

Detwiler, R. L., Rajaram, H., and Glass, R. (2001). Nonaqueous-phase-liquid dissolution in variable-aperture fractures: Development of a depth-averaged computational model with comparison to a physical experiment. *Water Resources Research*, **37**(12), 3115–3129.

Detwiler, R. L., Rajaram, H., and Glass, R. J. (2009). Interphase mass transfer in variable aperture fractures: Controlling parameters and proposed constitutive relationships. *Water Resources Research*, **45**(8), W08436.

Dewar, H. and Soulard, F. (2010). Freshwater supply and demand in canada. Report, Statistics Canada.

Di Carlo, D., Irimia, D., Tompkins, R. G., and Toner, M. (2007). Continuous inertial focusing, ordering, and separation of particles in microchannels. *Proceedings of the National Academy of Sciences*, **104**(48), 18892–18897.

Di Carlo, D., Edd, J. F., Humphry, K. J., Stone, H. A., and Toner, M. (2009). Particle segregation and dynamics in confined flows. *Physical Review Letters*, **102**(9).

Dickson, S. E. and Thomson, N. R. (2003). Dissolution of entrapped dnapls in variable aperture fractures: Experimental data and empirical model. *Environmental Science and Technology*, **37**(18), 4128–4137.

Dunstan, D. E. and Stokes, J. (2000). Diffusing probe measurements of polystyrene latex particles in polyelectrolyte solutions: Deviations from stokes-einstein behavior. *Macromolecules*, **33**(1), 193–198.

Ernst, D. and Kohler, J. (2013). Measuring a diffusion coefficient by single-particle tracking: statistical analysis of experimental mean squared displacement curves. *Physical Chemistry Chemical Physics*, **15**(3), 845–849.

Esposito, S. J. and Thomson, N. R. (1999). Two-phase flow and transport in a single fracture-porous medium system. *Journal of Contaminant Hydrology*, **37**(3-4), 319–341.

Ewing, R. P. and Berkowitz, B. (1998). A generalized growth model for simulation initial migration of dense non-aqueous phase liquids. *Water Resources Research*, **34**(4), 611–622.

Ewing, R. P. and Gupta, S. C. (1993). Modeling percolation properties of random media using a domain network. *Water Resources Research*, **29**(9).

Fetter, C. W. (2001). *Mass Transport of Solutes*, book section 10.6, pages 400–409. Prentice Hall, Upper Saddle River, New Jersey, 4 edition.

Gerhard, J. I., Kueper, B. H., and Hecox, G. R. (1998). The influence of waterflood design on the recovery of mobile dnapls. *Ground Water*, **36**(2), 283–292.

Glass, R. J. and Nicholl, M. J. (1996). Physics of gravity fingering of immiscible fluids within porous media: An overview of current understanding and selected complicating factors. *Geoderma*, **70**(2-4), 133–163.

Glass, R. J. and Yarrington, L. (1996). Simulation of gravity fingering in porous media using a modified percolation model. *Geoderma*, **70**(2-4), 231–252.

Glass, R. J. and Yarrington, L. (2003). Mechanistic modeling of fingering, non-monotonicity, fragmentation, and pulsation within gravity/buoyant destabilized two-phase/unsaturated flow. *Water Resources Research*, **39**(3), 1058.

Glass, R. J., Nicholl, M. J., and Yarrington, L. (1998). A modified invasion percolation model for low-capillary number immiscible displacements in horizontal rough-walled fractures: Influence of local in-plane curvature. *Water Resources Research*, **34**(12), 3215–3234.

Glass, R. J., Conrad, S. H., and Peplinski, W. (2000). Gravity-destabilized nonwetting phase invasion in macroheterogeneous porous media: Experimental observations of invasion dynamics and scale analysis. *Water Resources Research*, **36**(11), 3121–3137.

Glass, R. J., Conrad, S. H., and Yarrington, L. (2001). Gravity-destabilized nonwetting phase invasion in macroheterogeneous porous media: near-pore-scale macro modified invasion percolation simulation of experiments. *Water Resources Research*, **37**(5), 1197–1207.

Glass, R. J., Nicholl, M. J., Rajaram, H., and Andre, B. (2004). Development of slender transport pathways in unsaturated fractured rock: Simulation with modified invasion percolation. *Geophysical Research Letters*, **31**(6), L06502.

Gregory, J. (2006). *Particle in Water: Properties and Processes*. CRC Press Taylor and Francis Group, Boca Raton, FL, USA, 1 edition.

Gutjahr, A. L. (1989). Fast fourier transform for random field generation. Report, N. M. Inst. of Min. and Technol, Socorro.

Hakami, E. and Larsson, E. (1996). Aperture measurements and flow experiments on a single natural fracture. *International Journal of Rock Mechanics and Mining Sciences and Geomechanics Abstracts*, **33**(4), 395–404.

Hartog, N., Cho, J., Parker, B. L., and Annable, M. D. (2010). Characterization of a heterogeneous dnapl source zone in the borden aquifer using partitioning and interfacial tracers: residual morphologies and background sorption. *J Contam Hydrol*, **115**(1-4), 79–89.

Haupt, R. L. and Haupt, S. E. (1998). *Practical Genetic Algorithms*. Wiley-Interscience, New York, NY, USA.

Ioannidis, M. A., Chatzis, I., and Dullien, F. A. L. (1996). Macroscopic percolation model of immiscible displacement: Effects of buoyancy and spatial structure. *Water Resources Research*, **32**(11), 3297–3310.

James, S. C. and Chrysikopoulos, C. V. (2000). Transport of polydisperse colloids in a saturated fracture with spatially variable aperture. *Water Resources Research*, **36**(6), 1457–1465.

James, S. C. and Chrysikopoulos, C. V. (2003). Effective velocity and effective dispersion coefficient for finite-sized particles flowing in a uniform fracture. *Journal of Colloid and Interface Science*, **263**(1), 288–295.

James, S. C. and Chrysikopoulos, C. V. (2011). Monodisperse and polydisperse colloid transport in water-saturated fractures with various orientations: Gravity effects. *Advances in Water Resources*, **34**(10), 1249–1255.

James, S. C., Bilezikjian, T. K., and Chrysikopoulos, C. V. (2005). Contaminant transport in a fracture with spatially variable aperture in the presence of monodisperse and polydisperse colloids. *Stoch Environ Res Risk Assess*, **19**(4), 266–279.

Jawitz, J. W., Sillan, R. K., Annable, M. D., Rao, P. S. C., and Warner, K. (2000). In-situ alcohol flushing of a dnapl source zone at a dry cleaner site. *Environmental Science and Technology*, **34**(17), 37223729.

Ji, S.-H., Yeo, I. W., Lee, K.-K., and Glass, R. J. (2003). Influence of ambient groundwater flow on dnapl migration in a fracture network: Experiments and simulations. *Geophysical Research Letters*, **30**(10), 1504.

Jin, M., Delshad, M., Dwarakanath, V., McKinney, D. C., Pope, G. A., Sepehrnoori, K., Tilburg, C. E., and Jackson, R. E. (1995). Partitioning tracer test for detection, estimation, and remediation performance assessment of subsurface nonaqueous phase liquids. *Water Resources Research*, **31**(5), 1201–1211.

Kavanaugh, M. C. and Rao, P. S. C. (2003). The dnapl remediation challenge: Is there a case for source depletion? Report, United State Environmental Protection Agency.

Keller, A. A., Roberts, P. V., and Blunt, M. J. (1999). Effect of fracture aperture variations on the dispersion of contaminants. *Water Resources Research*, **35**(1), 55–63.

Kim, J. W., Lee, J. K., Baik, M. H., and Jeong, J. (2015). Modeling in-situ transport of uranine and colloids in the fracture network in kurt. *J Contam Hydrol*, **173**, 59–68.

Koyama, T., Tsukahara, T., Jing, L., Kawamura, H., and Ohnishi, Y. (2008a). Numerical simulation of laboratory coupled shear-flow tests for rock fractures. *International Journal of Geotechnical Engineering*, **2**(3), 215–227.

Koyama, T., Neretnieks, I., and Jing, L. (2008b). A numerical study on differences in using navierstokes and reynolds equations for modeling the fluid flow and particle transport in single rock fractures with shear. *International Journal of Rock Mechanics and Mining Sciences*, **45**(7), 1082–1101.

Kreft, A. and Zuber, A. (1978). On the physical meaning of the dispersion equation and its solutions for different initial and boundary conditions. *Chemical Engineering Science*, **33**(11), 1471–1480.

Kretzschmar, R., Barmettler, K., Grolimund, D., Yan, Y.-d., Borkovec, M., and Sticher, H. (1997). Experimental determination of colloid deposition rates and collision efficiencies in natural porous media. *Water Resources Research*, **33**(5), 1129–1137.

Kueper, B. H. and Frind, E. O. (1988). An overview of immiscible fingering in porous media. *Journal of Contaminant Hydrology*, **2**(2), 95–110.

Kueper, B. H. and McWhorter, D. B. (1991). The behavior of dense, nonaqueous phase liquids in fractured clay and rock. *Ground Water*, **29**(5), 716–728.

Kueper, B. H., Stroo, H. F., Vogel, C. M., and Ward, C. H. (2014). *Chlorinated Solvent Source Zone Remediation*. SERDP and ESTCP Remediation Technology Monograph Series. Springer Science and Business Media, New York, NY, USA.

Longino, B. L. and Kueper, B. H. (1999). Nonwetting phase retention and mobilization in rock fractures. *Water Resources Research*, **35**(7), 2085–2093.

Mackay, D. M. and Cherry, J. A. (1989). Groundwater contamination: Pump-and-treat remediation. *Environmental Science and Technology*, **23**(6), 630–636.

Marcos, Fu, H. C., Powers, T. R., and Stocker, R. (2012). Bacterial rheotaxis. *Proceedings of the National Academy of Sciences*, **109**(13), 4780–4785.

Masaeli, M., Sollier, E., Amini, H., Mao, W., Camacho, K., Doshi, N., Mitragotri, S., Alexeev, A., and Di Carlo, D. (2012). Continuous inertial focusing and separation of particles by shape. *Physical Review X*, **2**(3).

Masciopinto, C., La Mantia, R., and Chrysikopoulos, C. V. (2008). Fate and transport of pathogens in a fractured aquifer in the salento area, italy. *Water Resources Research*, **44**(1), W01404.

Maupin, M. A., Kenny, J. F., Hutson, S. S., Lovelace, J. K., Barber, N. L., and Linsey, K. S. (2010). Estimated use of water in the united states in 2010. Washington, DC.

Meakin, P., Wagner, G., Vedvik, A., Amundsen, H., Feder, J., and Jossang, T. (2000). Invasion percolation and secondary migration: experiments and simulations. *Marine and Petroleum Geology*, **17**(7), 777–795.

Microspheres, P. I. and Guide, P. H. (2012). Microspheres and particles handling guide.

Mondal, P. K. and Sleep, B. E. (2013). Virus and virus-sized microsphere transport in a dolomite rock fracture. *Water Resources Research*, **49**(2), 1–17.

Mumford, K. G., Smith, J. E., and Dickson, S. E. (2010). The effect of spontaneous gas expansion and mobilization on the aqueous-phase concentrations above a dense non-aqueous phase liquid pool. *Advances in Water Resources*, **33**(4), 504–513.

O'Connor, D. (2002a). Part one- report of the walkerton inquiry: The events of may 2000 and related issues. Report, Ontario Ministry of the Attorney General.

O'Connor, D. (2002b). Part two - report of the walkerton inquiry: A strategy for safe drinking water. Report, Ontario Ministry of the Attorney General.

Parker, B. L., Cherry, J. A., Chapman, S. W., and Guilbeault, M. A. (2003). Review and analysis of chlorinated solvent dense nonaqueous phase liquid distributions in five sandy aquifers. *Vadose Zone Journal*, **2**(2), 116–137.

Pennell, K. D., Pope, G. A., and Abriola, L. M. (1996). Influence of viscous and buoyancy forces on the mobilization of residual tetrachloroethylene during surfactant flushing. *Environmental Science and Technologyl*, **30**(4), 1328–1335.

Petchsingto, T. and Karpyn, Z. T. (2010). Simulation of fluid percolation in a rough-walled rock fracture. *Hydrogeology Journal*, **18**(7), 1583–1589.

Qian, J., Zhan, H., Chen, Z., and Ye, H. (2011a). Experimental study of solute transport under non-darcian flow in a single fracture. *Journal of Hydrology*, **399**(3-4), 246–254.

Qian, J. Z., Chen, Z., Zhan, H. B., and Luo, S. H. (2011b). Solute transport in a filled single fracture under non-darcian flow. *International Journal of Rock Mechanics and Mining Sciences*, **48**(1), 132–140.

Rao, P. S. C., Annable, M. D., and Kim, H. (2000). Napl source zone characterization and remediation technology performance assessment: recent developments and applications of tracer techniques. *Journal of Contaminant Hydrology*, **45**(1-2), 63–78.

Reitsma, S. and Kueper, B. H. (1994). Laboratory measurement of capillary pressure-saturation relationships in a rock fracture. *Water Resources Research*, **30**(4), 865–878.

Reynolds, D. A. and Kueper, B. H. (2002). Numerical examination of the factors controlling dnapl migration through a single fracture. *Groundwater*, **40**(4), 368–377.

Robinson, N. I., Sharp Jr., J. M., and Kreisel, I. (1998). Contaminant transport in sets of parallel finite fractures with fracture skins. *Journal of Contaminant Hydrology*, **31**(1-2), 83–109.

Rodrigues, S. and Dickson, S. (2014). A phenomenological model for particle retention in single, saturated fractures. *Ground Water*, **52**(2), 277–83.

Rusconi, R., Guasto, J. S., and Stocker, R. (2014). Bacterial transport suppressed by fluid shear. *Nat Phys*, **10**(3), 212–217.

Salamon, P., Fernndez-Garcia, D., and Gmez-Hernndez, J. J. (2006a). Modeling mass transfer processes using random walk particle tracking. *Water Resources Research*, **42**(11), W11417.

Salamon, P., Fernandez-Garcia, D., and Gomez-Hernandez, J. J. (2006b). A review and numerical assessment of the random walk particle tracking method. *J Contam Hydrol*, **87**(3-4), 277–305.

Schuster, C. J., Ellis, A. G., Robertson, W. J., Charron, D. F., Aramini, J. J., Marshall, B. J., and Medeiros, D. T. (2005). Infectious disease outbreaks related to drinking water in canada, 1974-2001. *Canadian Journal of Public Health*, **96**(4), 254–259.

Segre, G. and Silberberg, A. (1962). Behaviour of macroscopic rigid spheres in poiseuille flow part 2. experimental results and interpretation. *Journal of Fluid Mechanics*, **14**(1), 136–157.

Shapiro, A. A. and Bedrikovetsky, P. G. (2010). A stochastic theory for deep bed filtration accounting for dispersion and size distributions. *Physica A: Statistical Mechanics and its Applications*, **389**(13), 2473–2494.

Sheet, P. I. F. M. T. D. (2013). Fluoresbrite microspheres technical data sheet.

Singhal, B. B. S. and Gupta, R. P. (2011). *Groundwater Contamination*, book section 12, page 233. Springer, New York, NY, USA.

Snow, D. T. (1970). The frequency and apertures of fractures in rock. *International Journal of Rock Mechanics and Mining Sciences and Geomechanics Abstracts*, **7**(1), 23–30.

Song, L. and Elimelech, M. (1993). Dynamics of colloid deposition in porous media: modeling the role of retained particles. *Colloids and Surfaces A: Physicochemical and Engineering Aspects*, **73**, 49–63.

Song, L. and Elimelech, M. (1994). Transient deposition of colloidal particles in heterogeneous porous media. *Journal of Colloid and Interface Science*, **167**(2), 301–313.

Taylor, G. (1953). Dispersion of soluble matter in solvent flowing slowly through a tube. *Proceedings of the Royal Society A: Mathematical, Physical and Engineering Sciences*, **219**(1137), 186–203.

Tidwell, V. C. and Glass, R. J. (1994). X ray and visible light transmission for laboratory measurement of two-dimensional saturation fields in thin-slab systems. *Water Resources Research*, **30**(11), 2873–2882.

Tompson, A. T. B. and Gelhar, L. W. (1990). Numerical simulation of solute transport in three-dimensional, randomly heterogeneous porous media. *Water Resources Research*, **26**(10), 2541–2562.

Torkzaban, S., Bradford, S. A., and Walker, S. L. (2007). Resolving the coupled effects of hydrodynamics and dlvo forces on colloid attachment in porous media. *Langmuir*, **23**(19), 9652–9660.

Tsimpanogiannis, I. N. and Yortsos, Y. C. (2004). The critical gas saturation in a porous medium in the presence of gravity. *Journal of Colloid and Interface Science*, **270**(2), 388–395.

Vesper, D. J., Loop, C. M., and White, W. B. (2003). Contaminant transport in karst aquifers. *Speleogenesis and Evolution of Karst Aquifers*, **1**(2), 1–11.

Wagner, G., Biroljev, A., Meakin, P., Feder, J., and Jossang, T. (1997). Fragmentation and migration of invasion percolation clusters: Experiments and simulations. *Physical Review E*, **55**(6), 7015–7029.

Weerakone, W. M. S. B., Wong, R. C. K., and Mehrotra, A. K. (2011). Single-phase (brine) and two-phase (dnaplbrine) flows in induced fractures. *Transport in Porous Media*, **89**(1), 75–95.

Weerakone, W. M. S. B., Wong, R. C. K., and Mehrotra, A. K. (2012). Measurement of capillary pressure curve of dnapl in a water-saturated sandstone fracture. *Journal of Geotechnical and Geoenvironmental Engineering*, **138**(5), 614–624.

Wilkinson, D. and Willemsen, J. F. (1983). Invasion percolation: a new form of percolation theory. *Journal of Physics A: Mathematical and General*, **16**(14), 3365–3376.

Willmann, M., Lanyon, G. W., Marschall, P., and Kinzelbach, W. (2013). A new stochastic particle-tracking approach for fractured sedimentary formations. *Water Resources Research*, **49**(1), 352–359.

Wilson, V., Power, C., Giannopoulos, A., Gerhard, J., and Grant, G. (2009). Dnapl mapping by ground penetrating radar examined via numerical simulation. *Journal of Applied Geophysics*, **69**(3-4), 140–149.

Xu, B., Yortsos, Y. C., and Salin, D. (1998). Invasion percolation with viscous forces. *Physical Review E*, **57**(1), 739–751.

Yang, Z., Niemi, A., Fagerlund, F., and Illangasekare, T. (2012a). Effects of single-fracture aperture statistics on entrapment, dissolution and source depletion behavior of dense non-aqueous phase liquids. *Journal of Contaminant Hydrology*, **133**, 1–16.

Yang, Z., Niemi, A., Fagerlund, F., and Illangasekare, T. (2012b). A generalized approach for estimation of in-plane curvature in invasion percolation models for drainage in fractures. *Water Resources Research*, **48**(9), W09507.

Yang, Z., Niemi, A., Fagerlund, F., Illangasekare, T., and Detwiler, R. L. (2013a). Dissolution of dense non-aqueous phase liquids in vertical fractures: effect of finger residuals and dead-end pools. *Journal of Contaminant Hydrology*, **149**, 88–99.

Yang, Z., Niemi, A., Fagerlund, F., and Illangasekare, t. (2013b). Two-phase flow in rough-walled fractures: Comparison of continuum and invasion-percolation models. *Water Resources Research*, **49**(2), 993–1002.

Zhang, W., Tang, X.-Y., Weisbrod, N., Zhao, P., and Reid, B. J. (2015). A coupled field study of subsurface fracture flow and colloid transport. *Journal of Hydrology*, **524**, 476–488.

Zheng, Q., Dickson, S. E., and Guo, Y. (2009a). Differential transport and dispersion of colloids relative to solutes in single fractures. *Journal of Colloid and Interface Science*, **339**(1), 140–51.

Zheng, Q., Dickson, S., and Guo, Y. (2009b). Influence of aperture field heterogeneity and anisotropy on dispersion regimes and dispersivity in single fractures. *Journal of Geophysical Research*, **114**, B03205.